SULFUR-BRIDGED CHROMOPHORE DIMERS

by

Peter R. Christensen

B.Sc., The University *of* Wisconsin, Oshkosh, 2010

A Thesis Submitted *in* Partial Fulfillment *of*
the Requirements *for* the Degree *of*

DOCTOR *of* PHILOSOPHY

in

The Faculty *of* Graduate and Postdoctoral Studies

(Chemistry)

The University *of* British Columbia
(Vancouver)
September, 2016

ABSTRACT

Controlling both energy and electron transfer processes is necessary for the performance of both light harvesting, and light emitting devices. The efficiency of both energy and electron transfer depends on the degree, or magnitude of the electronic coupling between molecules. In photosynthetic organisms such as plants and bacteria, long range energy transfer occurs between electronically coupled assemblies of chlorophyll molecules. The remarkable energy transfer efficiencies of light harvesting complexes employed in photosynthesis is intimately related to the orientation and intermolecular spacing between neighboring, identical chlorophyll molecules.

In an attempt to develop inexpensive artificial light harvesting systems and devices researchers have synthesized an impressive catalogue of organic small molecules and polymers to generate free electrons and holes from absorbed light energy. The most commonly employed design principle for synthesizing both small molecule and polymer light absorbing systems is to link together an electron deficient (acceptor) molecule to an electron rich (donor) molecule through a conjugated linker. The conjugated bridge between donor and acceptor units enables charge transfer states that offer band-gap tuning and more easily separated electron/hole pairs. However, exciton migration in these synthetic donor-acceptor systems only partially mimics the assemblies of light harvesting molecules found in nature. As a result, exciton migration is limited to very short distances in synthetic light harvesting organic molecules.

The following thesis presents a new approach for controlling the electronic coupling between neighboring identical molecules. By bridging two identical molecules about a sulfur atom, the electronic coupling between the two molecules can be increased by increasing the oxidation state of the “sulfur-bridge”. The broader implication of this work is that we may not need to use strongly coupled, conjugated donor-acceptor systems to achieve efficient charge separation and excitation migration. Instead, by using a non-conjugated linker, such as sulfur or perhaps even a saturated carbon atom, between molecules with identical electronic structure we may be able to enhance exciton transport in synthetic light harvesting assemblies.

PREFACE

The contents of Chapter 2 have been published previously and I am the principal,[*] and co-first author[†] of this content, under the supervision of Prof. Michael O. Wolf. The work presented in Chapter 2 was performed in collaboration with Prof. Chris Bardeen and Chad Cruz of the University of California Riverside and also with Dr. David Casanova of the Euskal Herriko Unibertsitatea (UPV/EHU), Donostia Spain. The photoluminescence lifetimes and transient absorption data presented in Chapter 2 were collected and analyzed by Chad Cruz and Chris Bardeen (Sections 2.4.4 and 2.5). The computational work presented in Chapter 2 (Section 2.6) was performed by David Casanova.

The contents of Chapter 3 have also been published previously[‡] and I am the principal author of this content, under the supervision of Prof. Michael O. Wolf. The crystallographic data (excluding PXRD) in Chapter 3 were obtained and analyzed by Dr. Brian Patrick and Élise Caron of the University of British Columbia.

The contents of Chapter 4 are included in a manuscript in preparation. The concept, experimental work, equipment fabrication, code writing, and analysis were all performed by me, under the supervision of Prof. Michael O. Wolf.

All of the authors listed in the publications below were involved in the discussion and writing of the manuscripts.

All figures, unless otherwise specified, have been created by me or in collaboration with the previously specified authors and are used with permission.

---

[*] **Christensen, P. R.**; Nagle, J. K.; Bhatti, A.; Wolf, M. O. *J. Am. Chem. Soc.* **2013**, *135*, 8109.

[†] Cruz, C. D.*; **Christensen, P. R.***; Chronister, E. L.; Casanova, D.; Wolf, M. O.; Bardeen, C. J. *J. Am. Chem. Soc.* **2015**, *137*, 12552 (*equal contribution)

[‡] **Christensen, P. R.**; Patrick, B. O.; Caron, E.; Wolf, M. O. *Angew. Chem*. **2013**, *125*, 13184.

TABLE *of* CONTENTS

LIST *of* TABLES

LIST *of* FIGURES

LIST *of* SCHEMES

LIST *of* EQUATIONS

LIST *of* LISTINGS

LIST *of* SYMBOLS *and* ABBREVIATIONS

δ	NMR Shift parts per million
%	Percentage
Δf	Solvent Polarizability
$\Delta \nu$	Stokes Shift
$\Delta \mu$	Difference between Ground, and Excited-State Dipole
^{13}C	Carbon
^{1}H	Proton
A	Measured Absorbance Energy
a	Onsager Radius
Å	Angstrom (10^{-10} m)
ACN	Acetonitrile
arb. or a.u.	Arbitrary Units
ATR	Attenuated Total Reflection
Avg.	Average
BChl-a	Bactereochlorophyll a
BHJ	Bulk Heterojunction
CB	Conduction Band
CCD	Charge Coupled Device
CD_2Cl_2	Deuterated Dichloromethane
$CDCl_3$	Deuterated Chloroform
CH_2Cl_2	Dichloromethane
CHx	Cyclohexane
cm	Centimeter (10^{-2} m)
cm^{-1}	Wavenumber
CMYK	Cyan, Magenta, Yellow, Black
cos	Cosine
CPU	Central Processing Unit
CR	Charge Resonance
CT	Charge Transfer
d	Molecular density
dba	Dibenzylideneacetone

DFT	Density Functional Theory
dppf	Bis-dipheylphosphinoferrocene
DSSC	Dye Sensitized Solar Cell
e^-	Electron
EI MS	Electron Ionization Mass Spectrometry
Em.	Emission
eq.	Equivalent
ESI MS	Electrospray Ionization Mass Spectrometry
ETL	Electron Transport Layer
eV	Electronvolt
Ex	Excimer
F	Integrated Area under Fluorescence Spectrum
fs	Femtosecond (10^{-15} s)
FT-IR	Fourier Transform Infrared Spectroscopy
FTO	Fluorine Doped Tin-Oxide
g	Grams
GC-MS	Gas Chromatography Mass Spectrometry
h	Planck's Constant (6.62×10^{-34} m^2 kg s^{-1})
h^+	Hole
HMBC	Heteronuclear Multiple Bond Correlation NMR Experiment
HOMO	Highest Occupied Molecular Orbital
HPLC	High Performance Liquid Chromatography
HSQC	Heteronuclear Single Quantum Coherence NMR Experiment
HTL	Hole Transport Layer
IC	Internal Conversion
I_f	Measured Fluorescence Intensity
ISC	Intersystem Crossing
ITO	Indium doper Tin-Oxide
J	Coupling Constant (NMR)
J	Joule (kg m^2/s^2)
JPG or JPEG	Joint Photographic Experts Group, File Format

k	Boltzmann's Constant (1.38×10^{-23} m^2 kg s^{-2} K^{-1})
k	Reaction Rate Constant
kHz	Kilohertz
kV	Kilovolt
LE	Localized Excited State
LED	Light Emitting Diode
LHC	Light Harvesting Complex
LUMO	Lowest Unoccupied Molecular Orbital
M	Molarity (mol L^{-1})
M	Molecular Weight
***m*-CPBA**	meta-chloroperoxybenzoic acid
m/z	mass to charge ratio
mA	Milliamp
mg	Miligram
MHz	Megahertz (10^6 Hz)
min	Minute
mL	Milliliter
MLCT	Metal to Ligand Charge Transfer
mm	Millimeter (10^{-3} m)
mmol	Milimole
M_w	Molecular Weight
N	Avogadro's Number (6.02×10^{23} mol^{-1})
***n*-BuLi**	*n*-Butyllithium
Nap	Naphthalene
NBO	Natural Bond Order
nm	Nanometer (10^{-9} m)
NMR	Nuclear Magnetic Resonance
NTO	Natural Transition Orbital
O_2	Oxygen
ºC	Degrees Centigrade
OLED	Organic Light Emitting Diode

OPO	Optical Parametric Oscillator
OPV	Organic Photovoltaic
PBMA	poly(butylmethacrylate)
$PC_{60}BM$ or C_{60}	Phenyl-C_{61}-butyric acid methyl ester
$PC_{70}BM$ or C_{70}	Phenyl-C_{71}-butyric acid methyl ester
PCM	Polarizable Continuum Model
pH	Power of Hydrogen, -log[H^+]
PL	Photoluminescence
PMMA	poly(methylmethacrylate)
ps	Picosecond (10^{-12} s)
PVK	poly(*N*-vinylcarbazole)
p_x, p_y, p_z	p-Orbitals
PXRD	Powder X-Ray Diffraction
Pyr	Pyrene
QR	Quick Response
r_{AB}	Center-to-Center Distance between Neighboring Transition Dipoles
RGB	Red, Green, Blue
rpm	Revolutions per Minute
s	Second
S	Sulfide
S_1	Lowest Energy Electronic Excited Singlet-State
S1*	Excited Singlet State with charge transfer contribution
S_o	Electronic Ground-State
SO	Sulfide
SO_2	Sulfone
T	Temperature
T_1	Lowest Energy Electronic Excited Triplet-State
T2	Bithiophene
T3	Terthiophene
T6	α - Sexithiophene
TA	Transient Absorption
TADF	Thermally Activated Delayed Fluorescence
TDDFT	Time Dependent Density Functional Theory
T_g	Glass Transition Temperature

THF	Tetrahydrofuran
TICT	Twisted Intramolecular Charge Transfer
TiO_2	Titanium Dioxide
TTA	Triplet Triplet Annihilation
UBC	University of British Columbia
UV	Ultraviolet
UV-Vis	Ultraviolet-Visible Absorption
ν	Vibrational quantum number
V	Electronic Coupling
VB	Valence Band
V_{oc}	Open Circuit Voltage
wt%	Weight Percent
Δε	Exciton Energy Splitting
ϵ	Dielectric Constant
ε	Extinction Coefficient (10^4 M^{-1} cm^{-1})
ϵ_0	Permittivity of Vacuum
θ **and α**	Angles between Transition Dipole Moments
λ	Wavelength
μJ	Microjoule (10^{-6} J)
μm	Micrometer (10^{-6} m)
μ_T	Transition Dipole Moment
π	Ground-State molecular pi-orbital
π*	Excited-State molecular pi-orbital
τ_{PL}	Photoluminescence Lifetime
τ_{rad}	Radiative Lifetime
Φ_{PL}	Photoluminescence Quantum Yield
ψ	Wavefunction

ACKNOWLEDGEMENTS

I would first like to thank my supervisor Mike Wolf, for supporting and helping me grow as a scientist and as a person. For supporting me scientifically, and also for supporting my entrepreneurial side in the middle of a PhD. Over the course of my time in your lab I have always felt free to explore my creativity, and this has been one of the most valuable and formative experiences of my entire life. I have learned an incredible amount under your supervision. Thank you.

I would like to thank all of the members of the Wolf research group, past and present, you have all motivated me to succeed, and I hope I have done the same. I wish you all the best.

I must thank Dr. Saeid Kamal of LASIR labs at UBC for patiently putting up with my constant questions and curiosities about experimental photophysics. You helped me design several experiments, and the exercise of thinking things out with you has been extremely beneficial. Thank you.

Over the course of my PhD I have also spent a great deal of time tinkering with and fabricating equipment to perform experiments. In particular, the equipment used in Chapter 4 of this thesis would not have been possible without the guidance, patience, and the electrical engineering expertise of Milan Coschizza. Thank you.

To my buds Gunner and Tom. I've had a blast hanging out with you guys over the years. From slingin' coconuts on the beach to bike rides and forrest hikes, you guys have kept me sane during grad school. Thanks dudes.

To my siblings, Andrew, Sarah, Nathaniel and James, without your love and support this work would not have been possible. It's been so much fun growing up wth you guys and watching you all become amazing people!

For teaching me the value of hard work,
For always supporting my creativity,
For allowing me to be me,
I have, and will achieve.
I love you.

To My Parents.

CHAPTER 1

Introduction

1.1 Energy in the Human Context

In 1964, Soviet astronomer Nikolai Kardashev wrote an article entitled "Transmission of Information by Extraterrestrial Civilizations" where three types of advanced civilizations were proposed.[1] The metric that Kardashev used to characterize these advanced civilizations was by their hypothetical capabilities to harness energy. A type I civilization will have mastered the energy sources available on their own planet, including solar radiation and also the ability to control otherwise catastrophic global forces such as earthquakes and volcanoes yielding an estimated energy capability of $\sim 10^{12}$ - 10^{16} J/s. A type II civilization will be capable, through advances in astroengineering, of harnessing and transmitting the energy of a nearby star, yielding energy capabilities in the neighborhood of $\sim 10^{26}$ J/s. Further, a type III civilization will have exhaustively exploited its nearest star, including mastery over fusion by which the star operates, and will need to find new stars to continue advancing. Thus, the energy harnessing capabilities of a type III civilization is only limited by its ability to reach other stars, a concept currently outside of human understanding. Humans, as of 2016, barely show up on Kardashev's scale with global energy (production) of $\sim 10^{12}$ J/s.[2] As a civilization, our most abundant sources of energy come from the combustion of coal and natural gas, a process that, if continued, will destroy us and our planet before we can advance any further. Accordingly, as the population of our planet, and consequently the energy demand of our civilization, continues to grow, sources of clean and abundant energy are of immediate and long term concern.

1.2 Solar Energy

While humans are so far inefficient at harnessing energy from sustainable sources (< 20% of our total energy production),[2] planet Earth is filled with organisms that have evolved amazingly efficient mechanisms to make use of the huge amounts of solar energy that hits Earth's surface. According to the U.S. Dept. of Energy, our planet intercepts $\sim 10^{17}$ J/s of solar irradiation from our closest star, the Sun.[3]

The primary use of photo-generated electrons in light harvesting organisms is to store energy in chemical bonds.[4] While humans have made a habit of using energy stored in chemical bonds and individual atoms, e.g. coal, natural gas and nuclear fission, the majority of devices with which we interact on a daily basis use electrical energy. Accordingly, the heat energy obtained by the combustion of hydrocarbons or through the fission of uranium is, for the most part, turned into electrical energy (Figure 1.1). According to the U.S. Energy Information Administration (EIA), just over half (53%) of the total energy generated for human use was in the form of electrical energy.[5] However, due to inefficiencies in generation, transmission and distribution of electrical energy, only 30% of this electrical energy is actually used, bringing the percentage of total energy used in the form of electricity down to 35%.

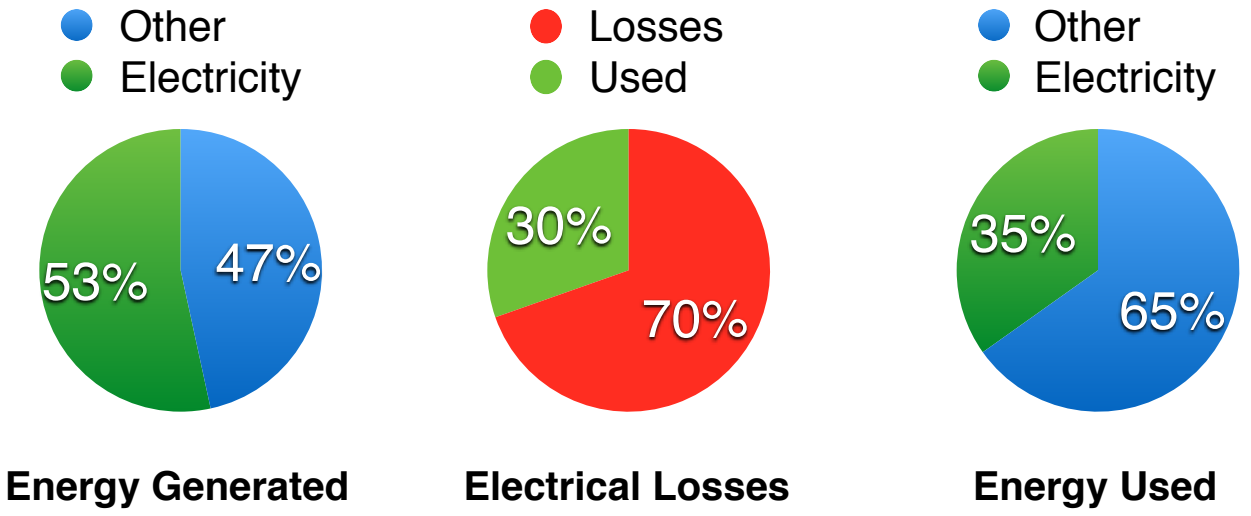

Figure 1.1. Charts showing the contribution of electrical energy to the total global energy generated in 2014 (left). After losses that occur during the generation, transmission and distribution of electrical energy (middle) only 35% of the total energy used is from electricity.

In terms of converting solar energy into usable forms of energy, photosynthetic, photovoltaic, and solar-thermal approaches have been the most successful so far.[6,7] The commonly applied term "solar cell" typically refers to a photovoltaic device, such as those found on the roofs of houses and powering our calculators and satellites. The biggest challenge associated with using photovoltaics to meet the global energy demand is the storage of electrons, namely in batteries.[8] Liquid/gaseous fuels on the other hand, whether mined or generated photosynthetically (e.g. Syngas),[7] are much easier to store and transport.

Electrical storage methods capable of being interfaced with the grid, such as redox flow cells and batteries for the home, are only now becoming a reality.[9,10] With over half of the global energy resources used to generate electrical energy it is essential, for the health of our planet and our civilization, that we succeed in developing sustainable sources of electricity.

1.2.1 First and Second Generation Solar Devices, The p-n Junction

To date, several different types of photovoltaic devices have been proposed. The earliest report that electrical current could be modified in the presence of light came from Becquerel, who showed that acidic solutions of silver salts could affect the measured voltage and current between two platinum electrodes when irradiated.[11] Becquerel's discovery later led to the complete description of the photoelectric effect in 1905 by Einstein.[12] The origin of the now ubiquitous photovoltaic solar cell comes from work performed in the 1940s when the semiconductor p-n junction was first demonstrated.[13] The semiconductor p-n junction was quickly leveraged by Bell Labs to create and patent the first "light sensitive device", or what is now colloquially known as the solar cell.[14]

The p-n junction is one of the most significant developments in the history of science and engineering. In addition to photovoltaic devices, the p-n junction is the basic component of transistors[13] and light emitting diodes[15] that make up the bits, bytes, and lights of the digital world we are now immersed in. Aptly named, the p-n junction is quite literally the junction, or rather the interface, between "n-type" and "p-type" semiconducting materials. The terms n-type and p-type refer to the nature of the dopant in the crystal lattice of a given semiconductor.[16] For instance, single crystalline group IV elements such as silicon and germanium, both intrinsic semiconductors, can be rendered p-type by doping the crystal with group III atoms (usually boron). These group III elements have one less valence electron than Si or Ge, thus, creating vacancies, or holes, in the material. Conversely, n-type semiconductors can be achieved by doping the group IV crystal with a group V atom, such as phosphorus, which have one extra valence electron compared to Si and Ge. Accordingly, p-type semiconductors act as hole conductors (electron vacancies), and n-type semiconductors more efficiently transport electrons.

When p- and n-type semiconductors are placed in contact with one another (p-n junction), electrons from the n-type material diffuse into the p-type material.[17] This diffusion of electrons results in

the localization of positive charges on the n-type material and the localization of negative charge on the p-type material at the interface (Figure 1.2a). This polarized interfacial region, also called the "depletion region", results in very low conductivity of both electrons and holes due to the presence of an electrostatic potential acting as a barrier. If an external bias is applied, e.g. by an electrical load, the barrier potential can be overcome and current can flow through the semiconductor junction, such is the function of a diode.

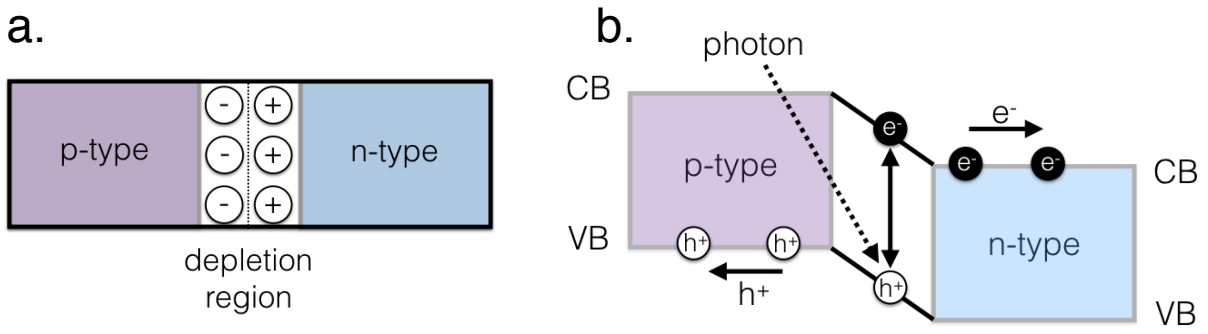

Figure 1.2. (a) Illustration of a typical inorganic p-n junction showing the "depletion region" that forms at the interface between p and n-type semiconductors. (b) Illustration showing function of the p-n junction in a photovoltaic device. Absorption of a photon results in an exciton (bound electron-hole pair). At the p-n junction the exciton is dissociates into a free electron and hole. Electrons are transported through the conduction band (CB) of the n-type material and holes are transported through the valence band (VB) of the p-type material, and a potential, or voltage, is generated.

The barrier potential can also be overcome by absorption of a photon with energy equal to the band gap of the semiconductor (VB to CB, Figure 1.2b). Initially, when a photon is absorbed by a semiconducting material, a bound (strongly coupled) electron/hole pair (exciton) is formed. The exciton then diffuses to the p-n interface where it is then separated into independent charge carriers (electron and hole). Accordingly, in the presence of an external (forward) bias from say, a battery or a light, the separated hole and electron can be transported through the p and n-type materials, respectively, to charge or power the external device.

Photovoltaic devices based on single junction (p-n) inorganic semiconductors are commonly referred to as first generation solar devices. Second generation solar devices are distinct from first generation devices by making use of polycrystalline, and amorphous inorganic materials. These second generation photovoltaic devices offer significantly lower manufacturing costs by obviating the use of

costly single crystalline inorganic materials. By eliminating the dependence on single crystalline materials second generation devices can also be manufactured into significantly larger devices, further reducing cost. The third generation of photovoltaics includes using tandem, multiple junction devices to improve the absorption cross-section. Over the past 60 years, solar devices have increased in efficiency from ~1% to 46% through advances in materials science, micro fabrication and electrical engineering.[18] However, the commercially viable inorganic solar devices such as those that one would find on top of a home have efficiencies of ~ 25 %. Currently, in order to achieve efficiencies in the 30%+ range additional micro fabrication is required, such as light concentrators and multiple (triple) junction devices that significantly increase the cost of the device.[19] Accordingly, several emerging third generation photovoltaic technologies seek to use materials that offer extremely low cost manufacturing methods such as ink-jet printing and roll-to-roll coating.

1.2.2 Third Generation Solar Devices, Organic Photovoltaics (OPVs)

Although the highest efficiency photovoltaic devices make use of inorganic semiconductors such as silicon and germanium, there are several disadvantages to these materials and the corresponding devices. The main reason inorganic semiconductors have achieved such success in solar technology, and in electrical engineering in general, is that the electronic properties (e.g. through n-doping or p-doping) can be very precisely and reproducibly controlled. Although silicon/germanium solar cells have become inexpensive enough to be widely adopted,[20] and are likely candidates for grid-scale energy harvesting in the near future, there are several applications where alternative materials and devices are of interest. For commercially available silicon photovoltaic devices, the cost of the hardware including the semiconductor panel, all wiring and structural components makes up less than 30% of the total cost associated with the switching to a photovoltaic system.[7] The remaining costs associated with realizing solar energy include installation, labor, permits, inspection, etc. Accordingly, if there was a way to make efficient photovoltaic devices that are both inexpensive and easy to install, the barrier to entry would be significantly reduced. Ideally, customers should be able to purchase a photovoltaic device from the local hardware store and install it themselves. In order for this do-it-yourself type of photovoltaic installation to become a reality,

the devices need to be smaller and lighter while also requiring minimal expertise and maintenance over the lifetime of the device.

One such technology that promises inexpensive, flexible, and even rollable solar devices are organic photovoltaics (OPVs). OPV technology grew out of the discovery that semiconducting, and even metallic properties can be achieved in organic small molecules and polymers.[21,22] The ability to synthesize, handle and process organic materials in solution provides an opportunity to fabricate devices using manufacturing processes such as roll-to-roll (flexographic, gravure) and ink-jet printing on inexpensive plastic substrates, significantly reducing costs.[23,24] Additionally, a wide variety of electronic and mechanical properties can be imparted in organic materials by using chemical synthesis. The prospect of flexible and mechanically robust solar devices will also enable photovoltaic functionality in objects with lightweight and portable form factors, significantly reducing labor costs associated with installation.[25]

The multidisciplinary field of organic electronics involves a close collaboration between organic synthesis, solid-state physics and electrical engineering with the goal of developing functional electronic devices using organic materials. One of the earliest demonstrations of an organic molecule with low resistivity was a bimolecular complex between the polycyclic aromatic molecule perylene, and bromine.[26] This chemical doping of an electron rich donor molecule was later expanded upon in the 1970s when it was shown that metallic conductivity could be achieved in polyacetylene through doping with halogens.[27] For their work on the synthesis and physical characterization of conductive polymers, Heeger, MacDiarmid, and Shirakawa were awarded the 2000 Nobel Prize in Chemistry.

Since the discovery of semiconducting and metallic properties in conjugated polymers and small molecules, numerous synthetic materials have been created for organic photovoltaic (OPV) applications. A great deal of work has been published regarding the synthesis of both n-[28] and p-type[29] semiconducting, organic small molecules and polymers. The typical synthetic route to p-type organic materials is to append electron-donating groups to a π-conjugated small molecule or polymer. The effect of additional electron density often raises the energy of the highest occupied molecular orbital (HOMO), which lowers the oxidation potential, making these systems more susceptible to oxidative doping. Conversely, electron-withdrawing substituents can be appended to conjugated molecules in order to lower the energy of the

lowest unoccupied molecular orbital (LUMO), lowering the reduction potential, making these materials more susceptible to reductive, or n-type doping.

In the context of OPVs, p-type materials are commonly referred to as "donors" and the n-type materials as "acceptors". Much like the inorganic p-n junction, the interface between organic donor and acceptor materials facilitates exciton dissociation into free holes and electrons.[30,31] The earliest report of a two-layer, donor acceptor organic photovoltaic device came from Calvin (Figure 1.3).[32]

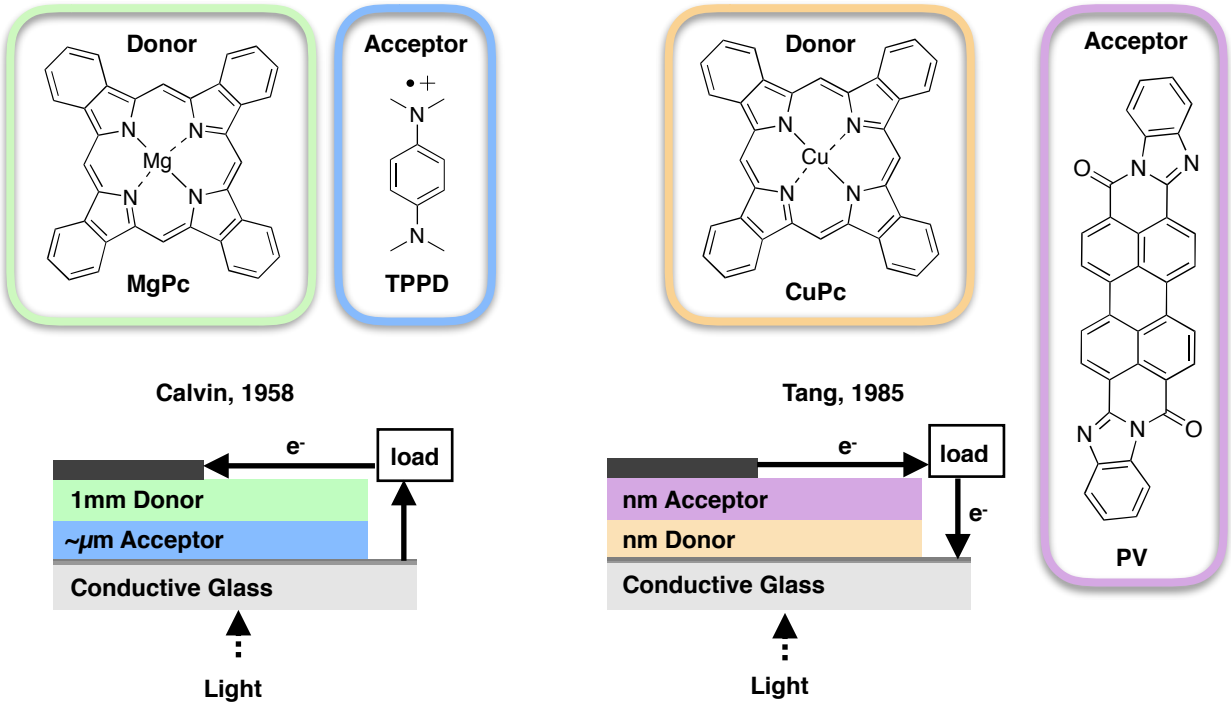

Figure 1.3. The earliest known multilayer, solid-state organic photovoltaic devices from Calvin (left) and Tang (right).

Calvin's original device used a thick (~1 mm) layer of magnesium phthalocyanine (**MgPc**) as a donor material and oxidized tetramethyl-p-phenylenediamine (**TPPD**, or Wurster's blue) as an acceptor. While Calvin's OPV device received little attention for about 30 years, perhaps due to the extremely low efficiency, it served as inspiration, or as a proof of principle for seminal work put forth by Tang (UBC Chemistry Class of 1970) in 1985.[33] Tang's OPV paper showed that thin (<100 nm) layers of donor (**CuPc**) and acceptor (**PV**) materials on top of one another enables photovoltaic efficiencies of ~1%

(Figure 1.3). The OPV put forth by Tang in the mid 1980s has served as a design principle for development in OPV technology that exists to this day.

Much like inorganic p-n junction solar devices, the interface between p- and n-type organic semiconductors also enables electron and hole separation. In a simple OPV device, light is absorbed by the donor (p-type) material and an exciton is formed (Figure 1.4). The bound electron (e^-) and hole (h^+) pair (exciton) then diffuses through the donor material to the interface between the donor and the acceptor (n-type) materials. At the donor-acceptor interface, the exciton is separated into free charge carriers, localizing the hole on the donor and the electron on the acceptor. The hole must then diffuse through the donor material, and the electron through the acceptor where they are collected by opposing electrodes.

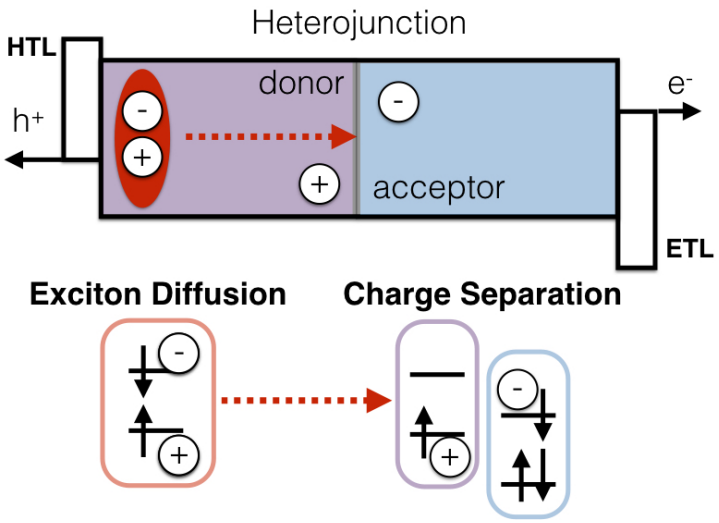

Figure 1.4. Illustration of a typical multilayered organic photovoltaic device (OPV). Absorption of a photon by the donor material results in the formation of a bound electron hole pair, or exciton (red) which then diffuses the the donor-acceptor interface where charge separation occurs.

Perhaps one of the biggest challenges associated with OPVs is the limited diffusion lengths of the exciton. In most organic materials the exciton is only able to travel ~10 nm before the electron and hole recombine.[34] Collapse of the exciton through electron and hole recombination results in either emission of a photon (radiative) or through molecular vibration (non-radiative) generating heat. After Tang's 1985 paper on the two-layer device structure, the next major breakthrough in OPV technology was the concept of the bulk heterojunction 10 years later by Heeger.[35] The bulk heterojunction (BHJ) is, in its most basic

form, a mixture of both p- and n-type materials, or a donor-acceptor blend, that results in an interpenetrating network of donor-acceptor interfacial regions. By controlling the sizes of the donor and acceptor domains to ~10 nm in the BHJ network, the probability of exciton diffusion to the donor-acceptor interface can be optimized. To date, the bulk heterojunction OPV remains the dominant design and the 20 years that have followed its invention have been witness to enhanced device efficiencies through the design of new donor and acceptor materials (Figure 1.5).

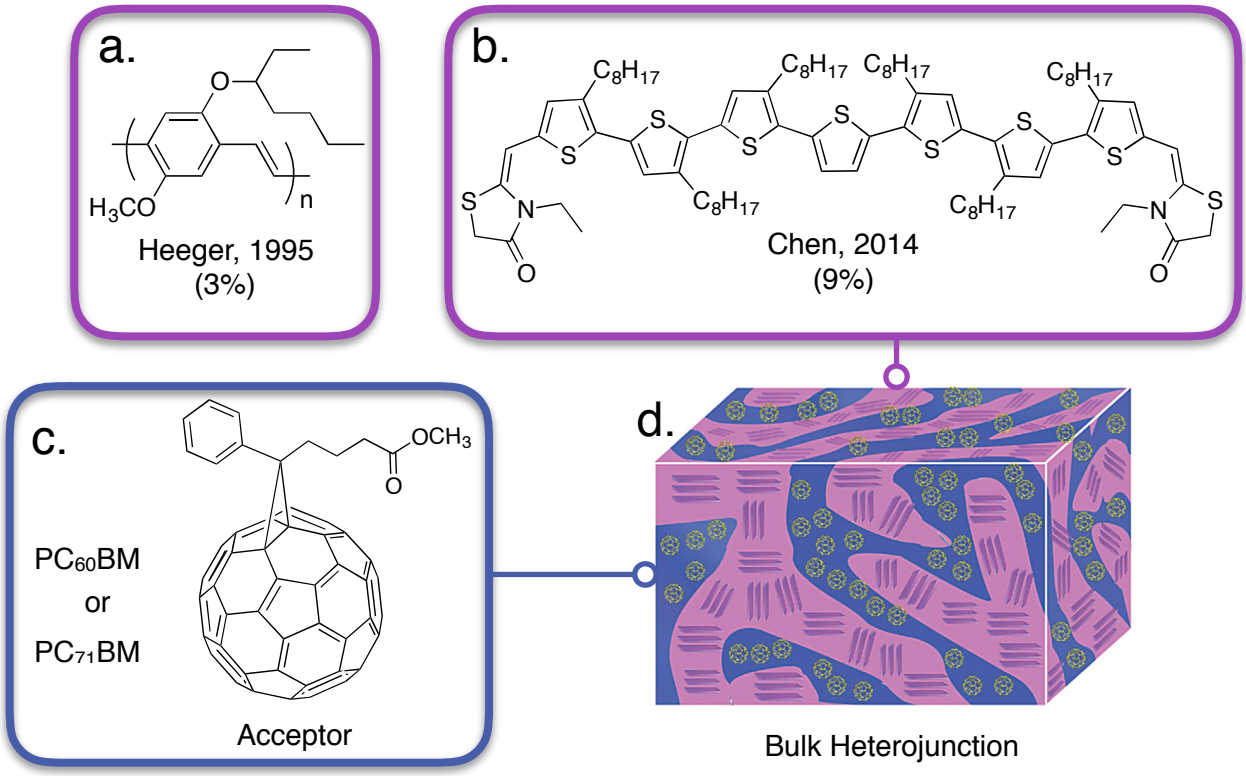

Figure 1.5. Structures of the original (a) and state of the art (b) donor materials blended together with soluble fullerene derivatives (c) C_{60} and C_{71} as an acceptor material (respectively) to yield a segregated, interpenetrating bulk heterojunction (d) * Image in (d) from Ref. 37. Reproduced with permission from Nature Publishing Group.

From a molecular design prospective, a huge variety of synthetic donor and acceptor materials have been explored and detailed analyses of these materials have been reviewed several times. Common donor materials are electron-rich derivatives of the conjugated oligomers and polymers of thiophene, phenylene-vinylene, aniline, and pyrrole (Figure 1.6). Common acceptor materials include oligomers and

polymers containing electron deficient heterocycles such as naphthalene/perylene diimide, benzothiadiazole, and cyano/fluorinated cyclic aromatics. To date, the most successful acceptor materials are soluble derivatives of the spherical, all carbon allotrope Buckminsterfullerene (or just fullerenes, commonly C_{60} or C_{71}).[36]

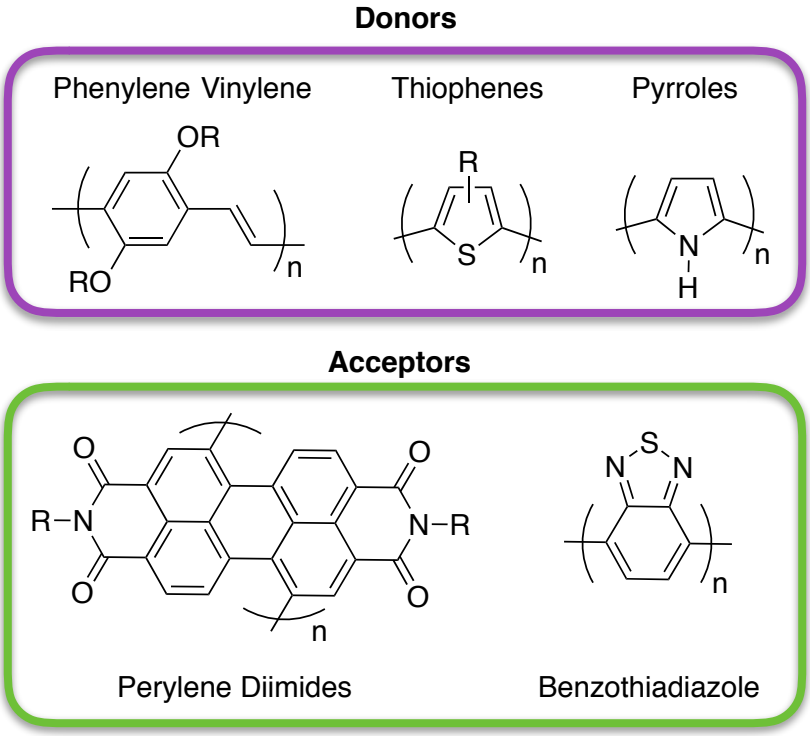

Figure 1.6. Common Donor and Acceptor Materials. Typically, longer oligomers and polymers of all of these materials (except poly(pyrroles)) are substituted with alkyl groups (R) in order to promote solubility.

Since the discovery of the donor/acceptor BHJ, synthetic chemists have used a variety of methods to tune the electronic and structural properties of donor and acceptor materials. The goal of all of this synthetic effort is to control a few key parameters of the resulting solar device. From a practical standpoint, the absorption energy of the donor material should closely match the solar spectrum in order to achieve efficient energy harvesting. Additionally, the organic molecules, both donor and acceptor, should be soluble, and once blended and deposited, segregate into regions of discrete $\leq$ 10 nm aggregates to maximize exciton transport to the donor/acceptor interfaces between these regions. Accordingly, most of the work in the area of organic photovoltaics is dedicated to synthesizing new donor materials and

optimizing the method of depositing these materials. The result of 20 years of chemical synthesis is an improvement of device efficiency from ~3% from the first BHJ solar device (1995) to ~12-13%.[37,38,39] It is worth noting that while fullerenes can be easily synthesized from abundant materials (carbon), the purification and functionalization required to render these materials soluble is still prohibitively expensive for wide spread commercialization. Promising research into non-fullerene acceptor materials is underway by a number of groups.[40]

1.2.3 Additional Third Generation Solar Devices: The Dye Sensitized Solar Cell.

In addition to inorganic semiconductor and organic photovoltaics, the dye-sensitized solar cell (DSSC) has received a great deal of attention over the past 20 years. The DSSC, introduced by Grätzel in 1991, made use of visible light absorbing ruthenium dye molecules adsorbed onto a semiconducting (usually TiO_2) surface (Figure 1.7a).[41] The dye molecules absorb lower energy photons than the semiconductor and due to the high energy excited-states of these molecules, enable injection of an electron into the conduction band of the semiconductor. After the first report, DSSCs quickly reached efficiencies >10%.[42] However, the efficiencies of DSSCs using organic/organometallic dyes, despite 20 years of considerable effort, have only increased marginally to ~13%.[43] Another drawback to the original

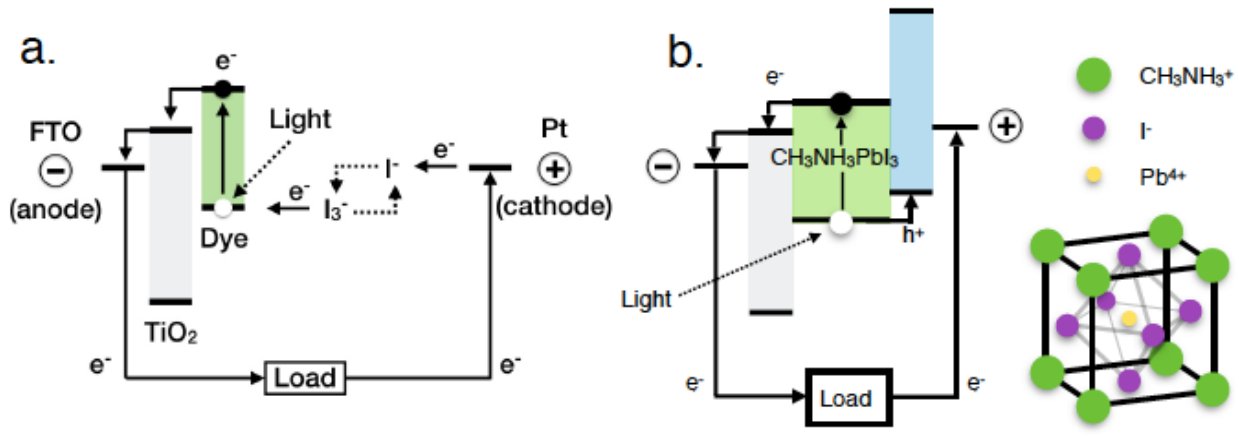

Figure 1.7. (a) Basic design and electrochemical operation of a DSSC. (b) Layered structure of a typical state of the art, solid-state perovskite photovoltaic cell. Inset shows the crystal structure of the methyl ammonium lead halide ($CH_3NH_3PbX_3$, X = I, Br, Cl) sensitizer.

DSSC design is that in order to achieve these high efficiencies, a liquid electrolyte is required to efficiently regenerate the oxidized dye molecules, limiting the stability and safety of these devices.

A major step forward in DSSC technology was the demonstration that efficient (~10%) photovoltaic devices could be achieved using organic metal-halide perovskite materials instead of the adsorbed small molecule dyes (Figure 1.7b).[44] Owing to long diffusion lengths of the exciton through the perovskite absorbing layer (~100 nm) the efficiencies of the perovskite solar cell have reached ~20% in a matter of 4 years.[45] Additionally, the use of a crystalline perovskite absorbing layer and solid-state charge extraction layers has enabled the fabrication of electrolyte-free devices.[46] Much like the DSSCs mentioned above, the methylammonium lead halide perovskite material absorbs visible light and injects an electron into the conduction band of TiO_2. Recent advances have also shown that the TiO_2 layer can be removed entirely, further simplifying the fabrication of these devices. The remarkable performance achieved so far in perovskite solar devices is largely due to the long exciton diffusion lengths that range from hundreds of nm to μm.[47] Despite the performance of the perovskite solar cells, there are a few drawbacks to these devices and the materials that enable their operation. Of primary concern is the use of water soluble lead, which poses potential health and environmental waste concerns.[48] Additionally, there is a rather large challenge associated with the instability of methylammonium lead halide perovskites.

1.3 Fourth Generation Solar Devices

The fourth generation of solar devices, currently in the early stages of concept and development, seek to harness new photophysical phenomena in order to achieve higher photon-to-electron conversion efficiencies. Both the first and second generation photovoltaic devices discussed in the previous sections focus primarily on the separation of the electron and the hole from the initially formed exciton. While hugely important for generating photocurrent, dissociation of the exciton in nature also involves antenna complexes that transport absorbed light energy large distances before charge separation occurs.

1.3.1 Photosynthesis and the Quantum Nature of Life

Instead of molecular assemblies with disparate electronic properties (i.e. donor and acceptor) the long range transport of excitation energy in photosynthesis is facilitated by controlled interactions between identical molecules (Figure 1.8). In these systems, coherent excitation is thought to play a role in the efficient (~100%) quantum efficiency of energy transport.[49] Instead of a cascade of energy transfer events occurring between neighboring molecules, all of the adjacent light absorbing molecules are excited simultaneously. This "coherence" between excited states results from the fact that the excited states of all of the neighboring (chlorophyll) molecules are identical. When such an assembly of identical molecules absorb a photon, the precise "position" of the excited state cannot be determined, and all of the molecules are said to be excited simultaneously, or coherently. In accordance with the Heisenberg uncertainty principle, it is only when the position of the excitation is measured (e.g. spectroscopically) that coherence between states collapses to a single observable state. If quantum coherence can be realized in synthetic light harvesting assemblies, in particular with OPV materials, then it is possible that long range exciton transport can be significantly improved

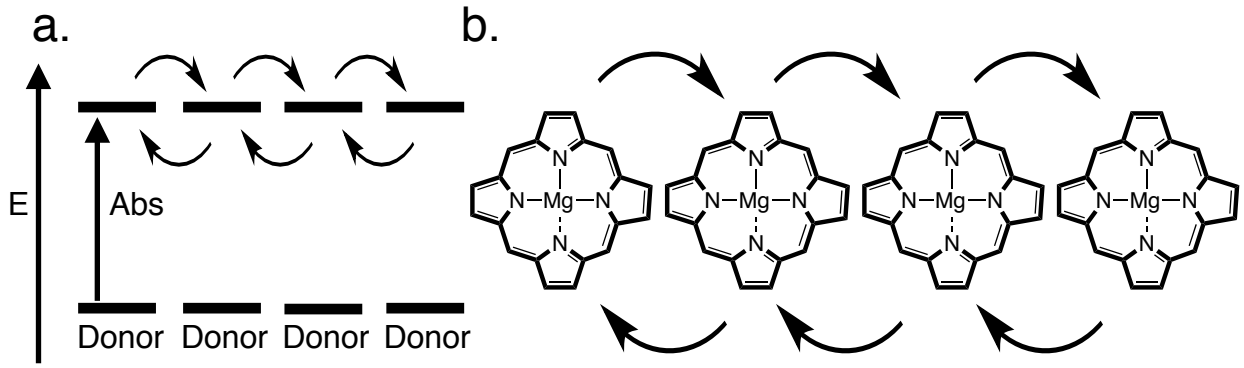

Figure 1.8. (a) Energy diagram illustrating how nature makes use of energy transfer between neighboring, identical chlorophyll molecules in the LHC I and II proteins.

While there are several types of light harvesting complexes (LHCs) employed by the diverse population of photosynthetic organisms, supramolecular assemblies of identical light absorbing small molecules always seems to be present. Figure 1.9 shows the crystal structure of LHCs I and II found in the purple bacteria *Rhodopseudomonas palustris*, a microorganism that is commonly found at the bottom

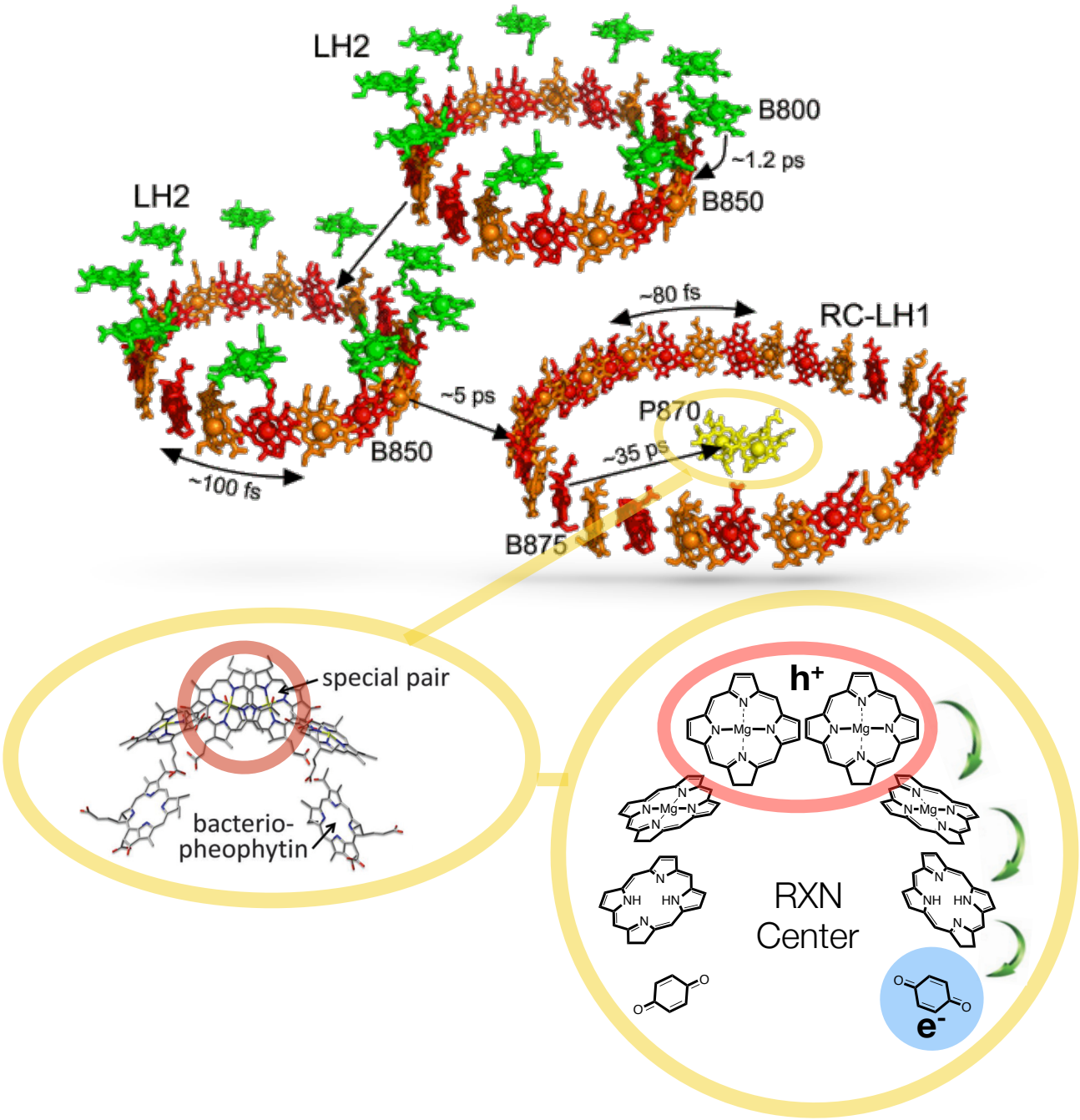

Figure 1.9. (a) Crystal structure of the light harvesting complexes (LHC) I and II with the protein scaffold omitted to highlight the identical sets of chlorophyl dimers (red and orange, chlorophyll a and b) where extremely efficient long-range energy transfer occurs and the reaction center (yellow) where separation of the electron and hole occurs through electron transfer from the chlorophyl special pair (red oval) to a quinone acceptor (blue). Figure of LHC I and II from Ref. 52, reproduced with permission.

of lakes, sometimes ~10 meters under water where light is scarce.[50,51,52] The two major components of LHC I are the antenna molecules, an array of 30 identical light harvesting bacteriochlorophyll (**BChl-a)** molecules (or 15 identical dimers), and the reaction center, where electron/hole separation occurs. While LHC I is capable of absorbing light directly, it is also surrounded by several light harvesting antenna assemblies (LHC II), which contain 9 monomeric **BChl-a** molecules (B800, Figure 1.9, green) and a ring of 18 identical **BChl-a** molecules (or 9 sets of dimers, B850, Figure 1.9, red). It is thought that absorption of a photon by the monomeric B800 assembly occurs first, followed by energy transfer to the ring of closely interacting B850 **BChl-a** molecules. The excited LHC-II assembly then transfers excitation energy to a neighboring LHC-II assembly, or directly to the ring of antenna chromophores of the LHC-I complex that surrounds the reaction center. From the outer ring of **BChl-a** molecules in LHC-I, excitation energy is transferred to a pair of identical **BChl-a** molecules in the middle of the protein (reaction center, Figure 1.9, yellow) known as the "special pair". From the special pair dimer, electron transfer to a quinone acceptor is facilitated by neighboring chlorophyll and pheophytin (chlorophyll without Mg^{2+} coordinated) molecules.

The unique feature of both LHC I and II is the ability to share excitation energy between the neighboring, identical **BChl-a** molecules through quantum coherence.[53] The result of this coherent excitation is a superposition of excitation, shared equally throughout the set of 18 (LHC II) or 30 (LHC I) neighboring molecules. In the context of photosynthesis, the coherent superposition of excited chlorophyll molecules is thought to be the reason why long range energy transfer in LHCs I and II is close to 100% efficient, even at biological temperatures.[54]

1.3.2 Singlet Fission, 200% Efficiency

Another emerging photophysical mechanism that has been proposed for raising the efficiency of photovoltaic devices is singlet fission. Singlet fission involves the conversion of one high energy singlet exciton into two lower energy triplet excitons (Figure 1.10). By creating two excitons per photon, singlet fission has the potential to raise the internal quantum efficiency (photon to electron) of solar devices to 200%. Amazingly, 200% yield of triplet excitons has been realized experimentally in several polycyclic aromatic molecules such as tetracene and pentacene. The ideal molecule for singlet fission is one that has

a triplet energy (ET_1) approximately one half the energy of the lowest energy excited singlet state ($ES_1 \sim 2\ ET_1$). Like the coherent light harvesting assemblies in photosynthesis, singlet fission requires specific control of the geometry between neighboring, identical molecules in order to work efficiently. As such, the most successful systems to date have been single crystals[55,56] and dimers[57,58,59] of tetracene and pentacene. Recently, significant advances have shown that certain amorphous polymers and molecular dimers can also show extremely efficient singlet fission by controlling the coupling between donor and acceptor molecules.[60]

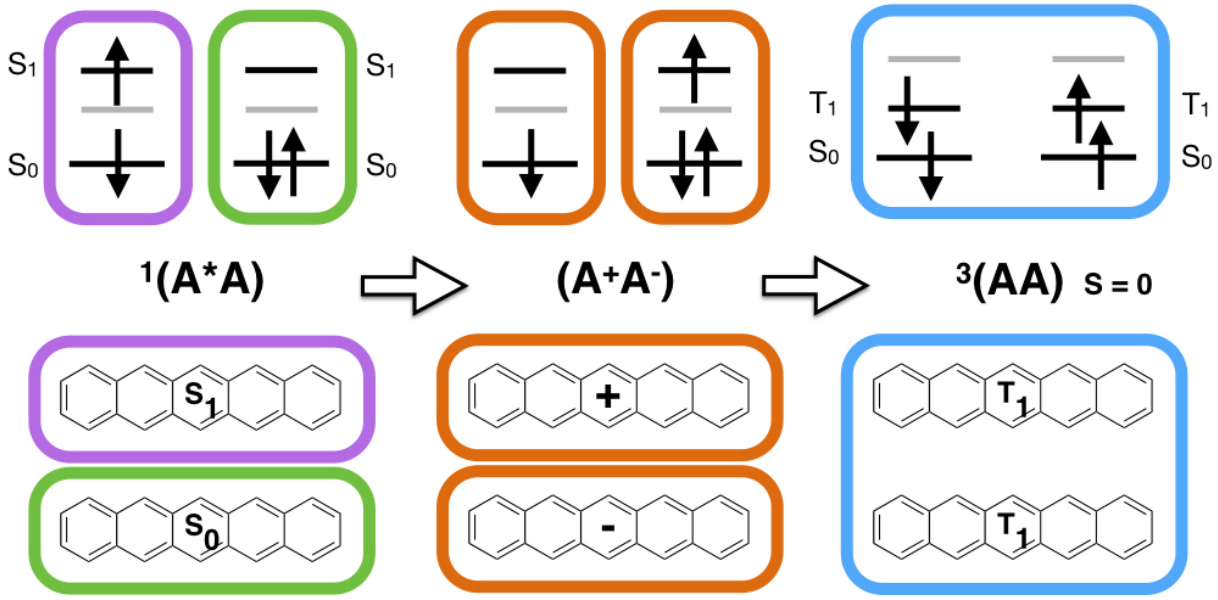

Figure 1.10. Energy diagrams showing the electronic excited (singlet) state of pentacene **^{1}(A*A)** interacting with a neighboring pentacene molecule through a charge transfer intermediate **(A^+A^-)**, through which, singlet fission to two neighboring triplet states **^{3}(AA)** occurs. The total spin of the **^{3}(AA)** state is S = 0, making this process spin allowed.

1.4 Electronic Coupling

Both singlet fission[61] and quantum coherence[62] (in the context of photosynthesis) are strongly dependent on the electronic coupling between neighboring identical molecules. In a general sense, the electronic structure and transitions of one atom or molecule can affect the electronic structure and transitions of another atom or molecule. The degree, or magnitude of this electronic interaction is termed the "coupling". The magnitude of the electronic coupling between neighboring atoms (intramolecular)

and molecules (intermolecular) has a significant impact on how individual molecules and assemblies behave in the presence of a perturbing electric field (e.g. light). The electronic coupling (V, equation 1.1) between two identical molecules (A) is given by the magnitude of the overlap between localized excited states (A*A to AA*). The total electronic coupling (V_{total}) has contributions from both dipole-dipole (V_{coulomb}) up to intermolecular spacing of ~100 Å, as well as electron exchange interactions (V_{short}) when the molecules are in close proximity (< 10 Å).[63]

(1.1)
$$V = \langle A^*A|\hat{H}|AA^*\rangle$$
$$V_{total} = V_{coulomb} + V_{short}$$

The electronic coupling between molecules can be experimentally observed through steady-state and time-resolved electronic absorption (UV-Vis) and photoluminescence spectroscopies. The degree of Coulombic (dipole-dipole) coupling between neighboring molecules is often observable by careful analysis of the electronic absorption spectroscopy. The short-range coupling, or electron exchange component, can be observed by looking for charge transfer character in the photoluminescence. Charge transfer intermediates are involved in the electron exchange between neighboring molecules and result in polar excited states that can be observed by measuring the photoluminescence spectrum in polar media. The following sections provide a background and describe the nature of these observables in the context of electronic coupling.

1.4.1 The Structure of Electronic Absorption Spectra

The absorption of a photon occurs significantly faster than the time constant associated with nuclear motion (vibration).[64] This "decoupling" of the nuclear and electronic components of the molecular Hamiltonian is the basis of the Born-Oppenheimer approximation. In the context of electronic absorption (and also photoluminescence) spectroscopy, the Born-Oppenheimer approximation implies that since the nuclei of a molecule have significantly greater mass than the electrons their "motion" is much slower than that of the electrons. Accordingly, the absorption (and emission) of a photon occurs with highest probability (faster) between two states with identical nuclear geometry. Electronic transitions

between identical nuclear configurations is also known as the Franck-Condon principle, which has served as a basis for rationalizing electronic absorption and emission spectra for over 80 years.[65,66] Although electronic transitions are quantized, a broad distribution of electronic transitions are often observed when the absorption spectrum of a molecule is measured.

At room temperature, the thermal energy (kT ~200 cm^{-1})[67] of an ensemble of molecules is insufficient to populate higher vibrational levels (vibrational transitions for most molecules range from ~1000 - 3000 cm^{-1}). As such, it is assumed that transitions occurring from the electronic ground state to electronic excited states also occurs from the vibrational ground state, $v = 0$. This is not to say that molecules are not vibrating or rotating at room temperature, but rather, the lowest vibrational state has the highest population.

A photon with sufficient and appropriate energy can be absorbed by a molecule, resulting in a transition from the lowest energy electronic and vibrational state to a higher energy "excited" state. According to the Franck-Condon principle, this electronic transition will have the highest probability between states with identical nuclear geometry. When the absorption spectrum of a molecule is measured (in solution), a broad distribution of electronic transitions is often observed due to the distribution of ground-state nuclear coordinates within the molecular ensemble. Depending on the nature of the ground-state molecular vibrations, this distribution of electronic transitions can be diffuse, resulting in a broad absorption spectrum, or well defined, resulting in an absorption spectrum with multiple, sharp features. For example, structurally rigid molecules, (e.g. polycyclic aromatics) often show sharp, well-defined structure in their absorption (π-π*) spectra due to restricted rotation and well-defined vibrations of the carbon-carbon bonds that make up the electronic π-system.[68]

1.4.2 The Transition Dipole

In addition to the Franck-Condon principle, allowed electronic transitions of a molecule must also have non-zero transition dipole moments (electric-dipole selection rules).[69] A non-zero transition dipole (μ_T, equation 1.2) associated with the transition between two electronic states (e.g. ψ_i and ψ_f) determines whether this particular transition is allowed. Accordingly, the strength (or interaction energy) of an

electronic transition is directly related to the the transition dipole between two electronic states (μ_T) which is non-zero if an electronic transition between state is possible.

(1.2)
$$\mu_T = \langle \psi_f | \hat{\mu} | \psi_i \rangle$$

Not to be confused with an electrostatic, molecular dipole, the transition dipole is associated with the magnitude and change in the distribution of electrons in a molecule in the presence of an interacting field (light). However, like an electrostatic dipole, the transition dipole can be represented as a vector with both magnitude and direction. The direction (polarization) of the transition dipole is associated with the change in electronic distribution between initial and final electronic states (ψ_i and ψ_f). Both the magnitude and axis of polarization are significant when two or more light absorbing molecules are put in close proximity, for instance, in molecular aggregates. In these molecular aggregates the light absorbing properties are altered due to an interaction between neighboring electronic transition dipoles.

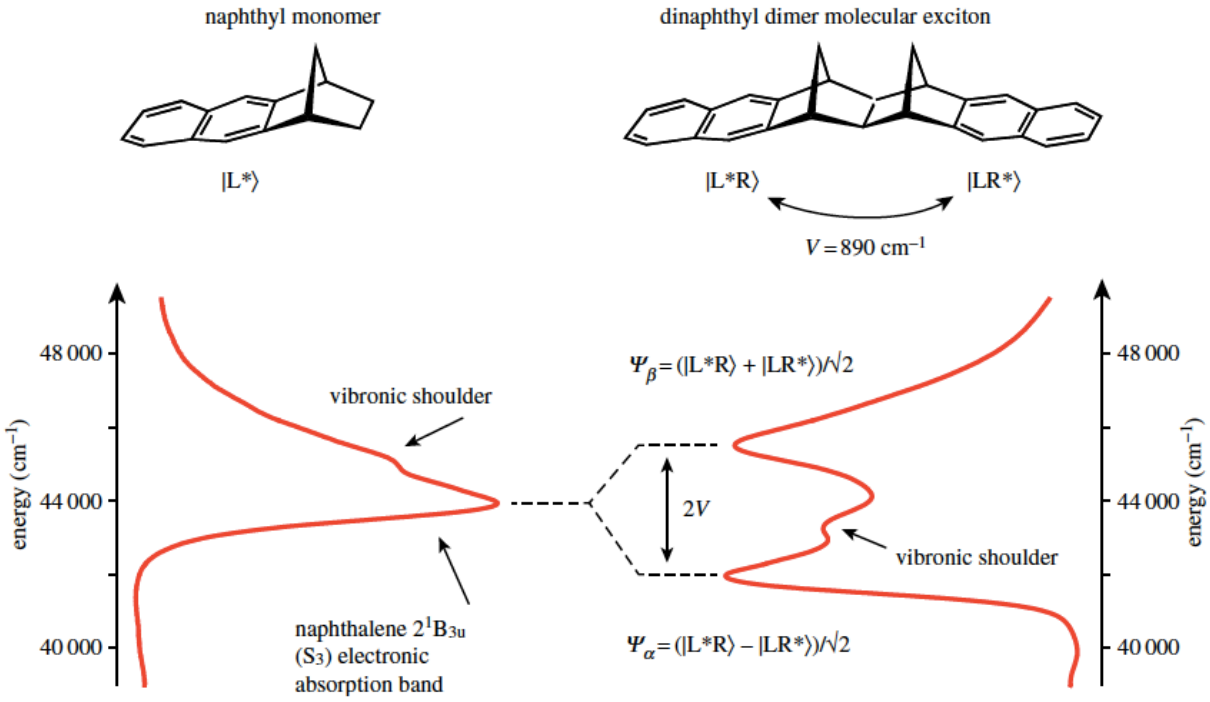

Figure 1.11. Structures and electronic absorption spectra for monomeric (left) and dimeric (right) naphthalene molecules. Figure (Ref. 71) reproduced with permission from Nature Publishing Group.

For instance, the polycyclic aromatic molecule naphthalene shows a dominant π - π* electronic transition ~230 nm (44,000 cm^{-1}) with a transition dipole polarized along the long molecular axis of the molecule (Figure 1.11).[70,71] The electronic absorption spectrum of the naphthalene monomer shows a single broad transition with a secondary "shoulder" that results from vibrational coupling. However, when two naphthalene molecules are linked together through a rigid, non-conjugated bridge, the absorption spectrum shows a splitting pattern that results from an interaction between the transition dipoles of the bridged molecules. The magnitude of the energy difference between the two transitions in the naphthalene dimer is directly proportional to the interaction, or coupling (V), between neighboring transition dipoles.

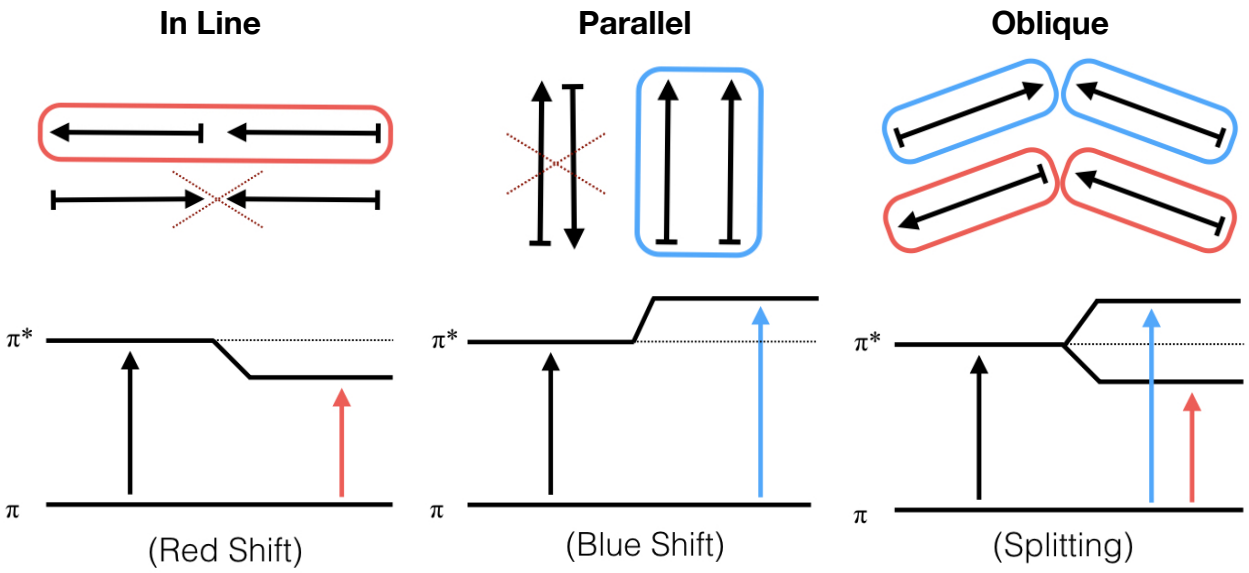

Figure 1.12. Illustration showing the effects of two neighboring transition dipoles on the observed electronic transitions. The relative orientation of the dipoles can interact attractively, to yield a lower energy transition (red), repulsively, to yield a higher energy transition (blue) or interfere deconstructively to reduce the oscillator strength to zero.

An explanation for the observation of such splittings in electronic absorption spectra was put forth by Kasha (Figure 1.12).[72] Kasha's model takes into consideration the magnitude and relative orientation (geometry) of two neighboring transition dipoles in order to explain excitonic splitting patterns. For instance, the naphthalene dimer discussed above (Figure 1.11) has two identical chromophores held apart from each other about some angle and intermolecular separation by the norbornene bridge. Since the transition dipole is polarized along the long molecular axis of naphthalene,

the transition dipole of each naphthalene chromophore in the dimer is pointing toward, or away from the other. This oblique orientation of the neighboring transition dipoles results in both an in-phase (attractive) and out-of-phase (repulsive) Coulombic interaction. The attractive (head-to-tail) dipole-dipole interaction results in a lowering of the energy associated with this transition. Conversely, the repulsive (head-to-head) dipole-dipole interaction results in a higher energy transition, compared to the monomeric naphthalene species. Accordingly, the splitting of the electronic absorption spectrum in the bridged naphthalene dimer is a result of two, strongly coupled electronic transition dipoles.

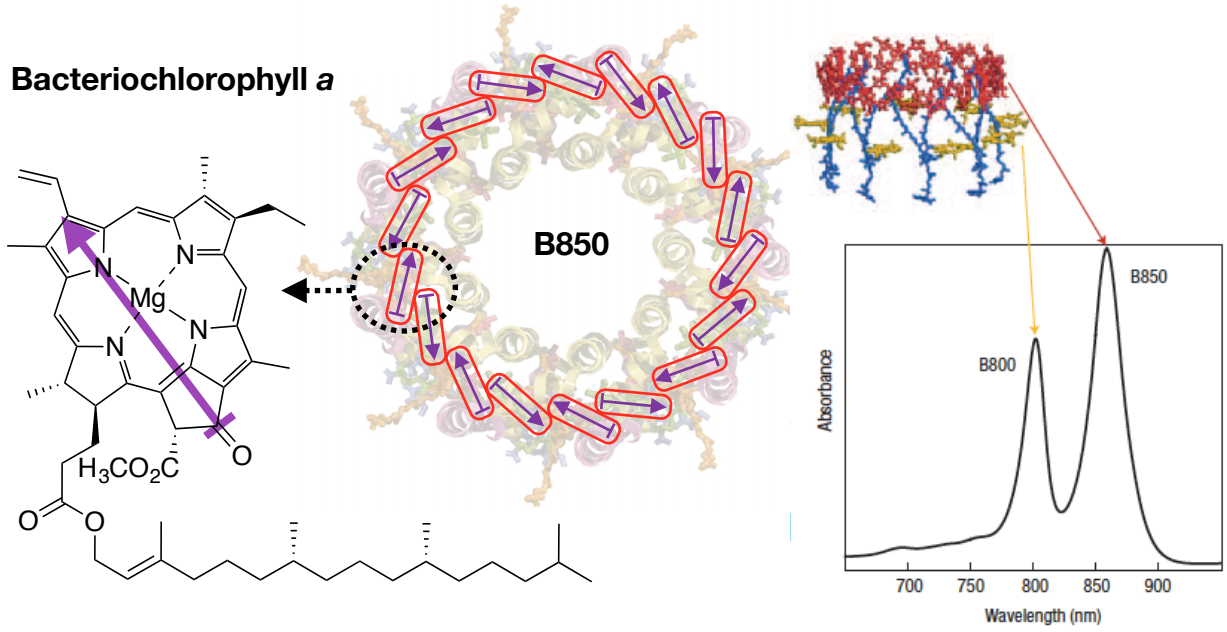

Figure 1.13. Structure and transition dipole (purple) of bacteriochlorophyll *a* (**BChl-*a***). In the B850 complex of LHC-II the transition dipoles of individual **BChl-*a*** dipoles are arranged in alternating orientations. Structure and absorption spectrum of the LHC II complex (Ref. 63) showing the distinct electronic transitions for monomeric bacteriochlorophyll (yellow, B800) and the 18 co-facial bacteriochlorophyll multimer (red, B850). Figure (Ref. 74) reproduced with permission from Nature Publishing Group.

Much like the naphthalene dimer, the light harvesting LHC I and II proteins contain 30 and 18 bacteriochlorophyll molecules (respectively) in close proximity (< 10Å) from one another.[73] The effect of this co-facial arrangement of (**BChl-*a***) molecules results in a shift in the absorbance spectrum compared to the respective monomeric **BChl-*a*** (Figure 1.13).[74] In the LCH II complex, both monomeric and multimeric **BChl-*a*** are present. The initial photon absorption event is thought to occur at one of these

monomeric **BChl-*a*** molecules (B800, yellow, Figure 1.13), which are situated orthogonal to the multimeric **BChl-*a*** ring (B850, red, Figure 1.13). The difference between the monomeric B800 and the multimeric B850 system can clearly be seen in the electronic absorption spectrum of LHC II where the B850 transition is shifted to ~850 nm from ~800 nm. This ~50 nm red-shift in absorption energy can be attributed to constructive, attractive coupling between neighboring **BChl-*a*** transition dipoles in the B850 ring.

1.4.3 Dipole-Dipole and Exchange Coupling

The mechanism of energy transfer between neighboring molecules with separations of ~10 - 100 Å is dominated by resonance energy, or Förster type transfer.[75] In addition to intermolecular distance and relative geometry, Förster resonance energy transfer (FRET) between donor and acceptor molecules depends strongly on the spectral overlap between the luminescence of the donor and the absorption of the acceptor. The energy and strength of an absorption or radiative transition is directly related to the dipole associated with this transition. Accordingly, the degree of dipole-dipole coupling (V_{dd}), which determines the efficiency of FRET, is directly proportional to the interaction of donor (μ_D) and acceptor (μ_A) transition dipoles which is scaled by the donor acceptor (center-to-center dipole) distance (R) and the relative orientation (k) (equation 1.3). The orientation factor (k) in equation 1.3 accounts for the relative angle and polarization for donor and acceptor transition dipoles.

$$V_{dd} = \frac{1}{4\pi\epsilon_o}\frac{k\mu_D\mu_A}{R^3} \tag{1.3}$$

For molecules at sufficiently large separations (~10 - 100 Å), resonance energy transfer and the dipole-dipole coupling dominate. However, at close intermolecular separations (< 10Å), electron exchange between donor and acceptor must also be considered (Figure 1.14, orange) in the expression for intermolecular electronic coupling (V_{short}). The exchange of electrons between an excited donor molecule and a neighboring ground state acceptor molecule was first proposed by Dexter in 1953.[76] It has been proposed that electron exchange does not contribute strongly to the electronic coupling between

neighboring chlorophyll molecules in LHC I and II.[77] However, in synthetic systems, especially those with close intermolecular spacing, the exchange component of the total electronic coupling must be considered.

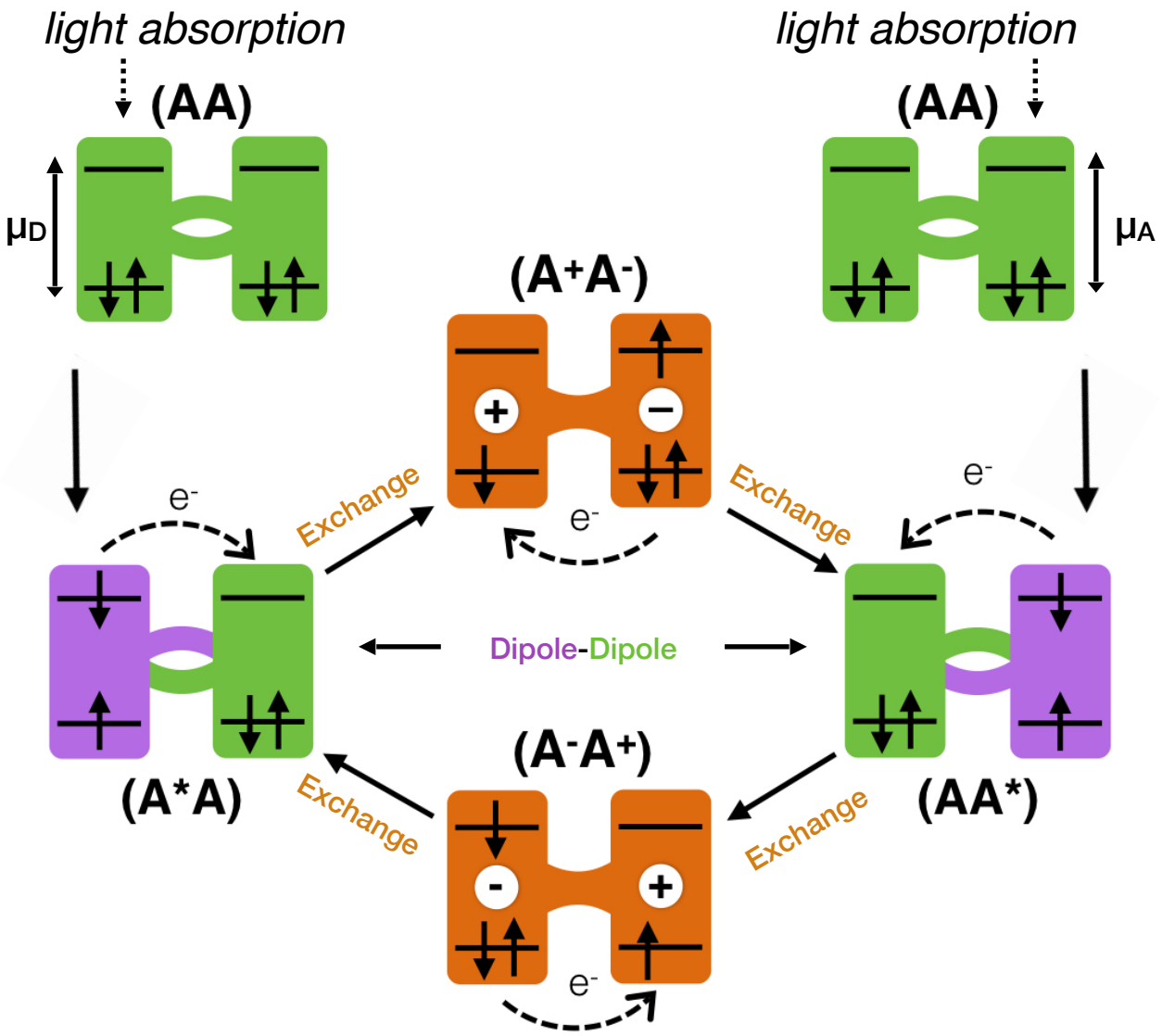

Figure 1.14. **Energy/Electron Transfer Between neighboring Identical Molecules**. Illustration showing the simplified four electron, four orbital treatment of two neighboring, identical molecules (A). Each "monomer" within the dimer has a ground state and an excited state (4 orbitals). Initially, (**AA**) the ground state configuration (green) is doubly occupied (top left, right). After light absorption excitation of the "left" or "right" half of the molecule is excited (**A*A** or **AA***, purple). This ground-state to excited state transition has associated with it a transition dipole (μ_A or μ_D) These two (degenerate) localized excited states can be interconverted through either dipole-dipole (Förster) energy transfer, or through a two-electron exchange (Dexter) mechanism involving charge transfer intermediates ($\mathbf{A^+A^-}$ and $\mathbf{A^-A^+}$, orange).

1.5 Goals of Thesis

In order to increase the exciton transport distance in organic donor materials we should take inspiration from the exciton transport observed in photosynthetic proteins. The ability of light harvesting assemblies to transport excitation energy large distances is intimately related to the controlled electronic coupling between neighboring chromophores. In nature, and in particular with LHCI and II discussed above, the transparent protein scaffold surrounding the light absorbing chlorophyll molecules is essential for obtaining the appropriate electronic coupling between molecules. The precise orientation of chlorophyll transition dipoles (Figure 1.13), intermolecular distances, and also the vibrational dynamics of the protein all play a role in achieving long-range, coherent excitation transfer. Accordingly, the next generation of man-made solar devices should focus, perhaps, not on the synthesis of new light absorbing materials, but on self-assembly and controlled intermolecular coupling between known chromophores.

In addition to supramolecular chemistry and self-assembled chromophore arrays, new methods for controlling intermolecular electronic coupling are of significant interest for the next generation of solar devices. The simplest system, with which to study intermolecular electronic coupling, is a dimer. By studying and controlling the electronic coupling between adjacent, identical molecules in a dimeric system we should be able to gain insight into new methods for larger multi-chromophore systems. Taking inspiration from the naphthalene dimer presented in the previous section, it is likely that the electronic interaction between neighboring molecules can be controlled by bridging two identical molecules together through some sort of linker. This linker could be an electrostatic (e.g. hydrogen bonding), ionic, or a covalent bond between neighboring molecules, so long as the neighboring molecules are not allowed to be fully conjugated with one another. An attractive feature of this covalent linker would be one that is electronically tunable in order to modulate the coupling between neighboring molecules. An electronically tunable system is attractive because, depending on the chromophore and the desired application, more or less electronic coupling may be preferred.

The addition of a double bond to oxygen, through chemical oxidation, provides a convenient and simple approach to controlling the electronic properties of an organic molecule. There are several widely available, inexpensive, and easy to handle chemical reagents that can oxidize organic molecules. In

particular, atoms that have stable electronic configurations with lone electron pairs, such as nitrogen, phosphorus and sulfur, can be readily oxidized. Among these examples, organo-sulfur and -phosphorus (phosphine) molecules, due to the 3p valence electrons, are able to form several neutral oxidation-states. Organo-phosphines can be three coordinate (R_3P) or four coordinate (R_3PO) where R is an alkyl or aryl single bond and O is an oxygen double bond. The oxidation of three coordinate phosphorus(III) to five coordinate phosphorus(V) can typically be performed in the presence of a mild oxidizing reagent, in many examples the oxygen in air is sufficient. Organo-sulfur molecules can be two coordinate (R_2S), three coordinate (R_2SO) and four coordinate (R_2SO_2).

In the context of controlling intermolecular electronic interactions, phosphorus and sulfur are attractive linkers between molecules due to their ease of preparation and tunable electronic properties through chemical oxidation. If light absorbing molecules (chromophores) are linked together about a sulfur, or phosphorus atom, then it might be possible to control the electronic interaction between the chromophores by oxidation or reduction of the phosphorus, or sulfur bridge. Sulfur is perhaps more suitable than phosphorus for molecular assemblies due to the access of three oxidation states (versus two), all of which are typically both air and water stable.

The chapters that follow explore the electronic nature of molecular dimers assembled by covalently bonding two identical chromophores about a sulfur atom. By chemically tuning the oxidation state of the bridging-sulfur atom it is shown that the electronic properties of the dimers can be controlled. Chapter 2 demonstrates the synthesis and detailed photo-physical characterization of a series of sulfur-bridged chromophores, whereby, the sulfur oxidation state controls the degree of electronic coupling between the bridged molecules. In addition to controlled electronic coupling, it is found that the fluorescence quantum yield can also be enhanced (compared to the unsubstituted chromophore) by increasing the oxidation state of the bridging sulfur.

Chapter 3 highlights a series of sulfur-bridged anthracene dimers that have different photo reactivity as a function of the bridging sulfur oxidation state. Notably, the sulfoxide (SO) bridged anthracene dimer shows rapid and quantitative conversion to the intensely fluorescent molecule 9,9'-bianthryl through loss of the SO bridge and formation of a new intramolecular carbon-carbon bond.

Chapter 4 focuses on the SO-bridged anthracene (**AnSO**), wherein the formation of 9,9'-bianthryl (**BA**) is leveraged to photochemically pattern fluorescent images with controllable luminescence intensity. The photochemical transformation of **AnSO** to **BA** offers access to patterned fluorescent images capable of storing large amounts of complex, encoded information. This final chapter explores the use of these multidimensional fluorescent images for easily covert security feature for anti-counterfeit applications.

CHAPTER 2*

Controlled Inter-Chromophore Electronic Coupling

2.1 Introduction

Taking inspiration from nature, symmetric dimers have the potential to optimize energy transfer and charge separation in optoelectronic devices. In this Chapter, a combination of optical spectroscopy (steady-state and time-resolved) and electronic structure theory is used to analyze the photophysics of sulfur-bridged dimers. This class of dimers has the unique feature that the interchromophore (intra-dimer) electronic coupling can be modified by varying the oxidation state of the bridging sulfur from sulfide (S), to sulfoxide (SO), to sulfone (SO_2).

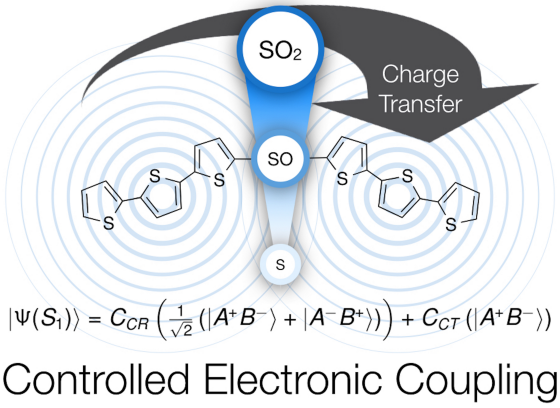

Figure 2.1. Structure of S-bridged terthiophene dimers (**T3SO$_n$**) illustrating the oxidation-state controlled electronic coupling between bridged molecules.

First, it is demonstrated that by bridging two identical chromophores about a sulfur atom, the photoluminescence quantum yield can be systematically enhanced by successively oxidizing the bridging sulfur (S < SO < SO_2). Secondly, the photophysical basis of this enhanced photoluminescence is studied using a combination of steady-state, and time-resolved optical spectroscopy and a mechanism is proposed. In general, control of the sulfur bridge oxidation state provides the ability to tune interchromophore (intra-dimer) electronic coupling without altering the molecular geometry or solvent polarity (Figure 2.1). This capability provides a new strategy for the design of functional supermolecules with applications in organic electronics.

* The experimental data presented in sections 2.4.10, 2.5, were collected and analyzed by Chad Cruz and Chris Bardeen, UC Riverside. The computational data in section 2.6 were collected and analyzed by David Casanova, UPV/EHU. The content of this chapter has been published previously:

Cruz, C. D.; **Christensen, P. R.**; Chronister, E. L.; Casanova, D.; Wolf, M. O.; Bardeen, C. J. *J. Am. Chem. Soc.* **2015**, *137*, 12552

Christensen, P. R.; Nagle, J. K.; Bhatti, A.; Wolf, M. O. *J. Am. Chem. Soc.* **2013**, *135*, 8109.

As discussed in Chapter 1, in nature, light harvesting organisms make extensive use of photo induced energy and electron transfer between adjacent molecules. A great deal of work has been focused on synthesizing electron donor/acceptor pairs to mimic these efficient natural systems. The most common approach is to unite an electron-rich donor with an electron-deficient acceptor using a π -conjugated linkage or "bridge". Separation of the donor and acceptor by such a π-conjugated bridge can enable charge transfer (CT) over large distances, limiting charge recombination.[78] While remarkable photovoltaic performance has been achieved using this approach,[79] these asymmetric systems only partially mimic the naturally occurring photosynthetic reaction centers where energy transfer between identical chromophores plays a central role in controlling excited-state dynamics.[80,81] Accordingly, the rational design of symmetrically bridged chromophore dimers, also called bichromophores, has attracted considerable theoretical[82,83] and practical[84,85] interest. For example, 9,9′-bianthryl, where two anthracene units are covalently bonded and adopt a nearly orthogonal orientation, has served as a model system for the study of excited-state electron transfer involving a symmetric chromophore pair.[86]

Recently, Thompson et al. have synthesized a series of symmetric dipyrrin molecules that show symmetry breaking CT using visible light.[87,88,89] These symmetric CT systems are of practical interest because the CT and neutral (delocalized) states are close in energy, which lowers the amount of energy lost in the charge separation event and has the potential to raise the open-circuit voltage (V_{OC}) of photovoltaic devices. Bichromophoric systems have also found applications in organic light emitting diodes (OLEDs).[90,91] Recently, Adachi et al. synthesized several types of organic molecules that harness both singlet and triplet excitons through a process known as thermally activated delayed fluorescence (TADF).[92,93] The singlet−triplet energy gap is most efficiently reduced when the HOMO and LUMO are spatially separated, which can be facilitated by intramolecular CT.[94] High-efficiency blue OLEDs were fabricated using SO_2-bridged symmetric bichromophores.[95,96] While it was demonstrated that these SO_2-bridged chromophores have reduced singlet−triplet gaps facilitated by CT, the role of the symmetric nature of these chromophores was not investigated.

It is anticipated that applications of dimeric molecules in photovoltaic and light emitting devices will require precise control of intra-dimer electronic interactions. One control strategy is to change the polarity of the environment and shift the relative energy levels of neutral and CT states; however, in solid-

state devices, this is impractical. An alternate strategy is to control the electronic coupling between light absorbing units. Ideally, such a control element would be built into the dimer molecule itself, without inducing large conformational changes. Decreasing the distance and angle between chromophores can enhance electron transfer, but if molecules are too close together, aggregation-induced excited-state quenching often results.[97] The goal is then to control the inter-chromophore coupling while maintaining ideal geometry.

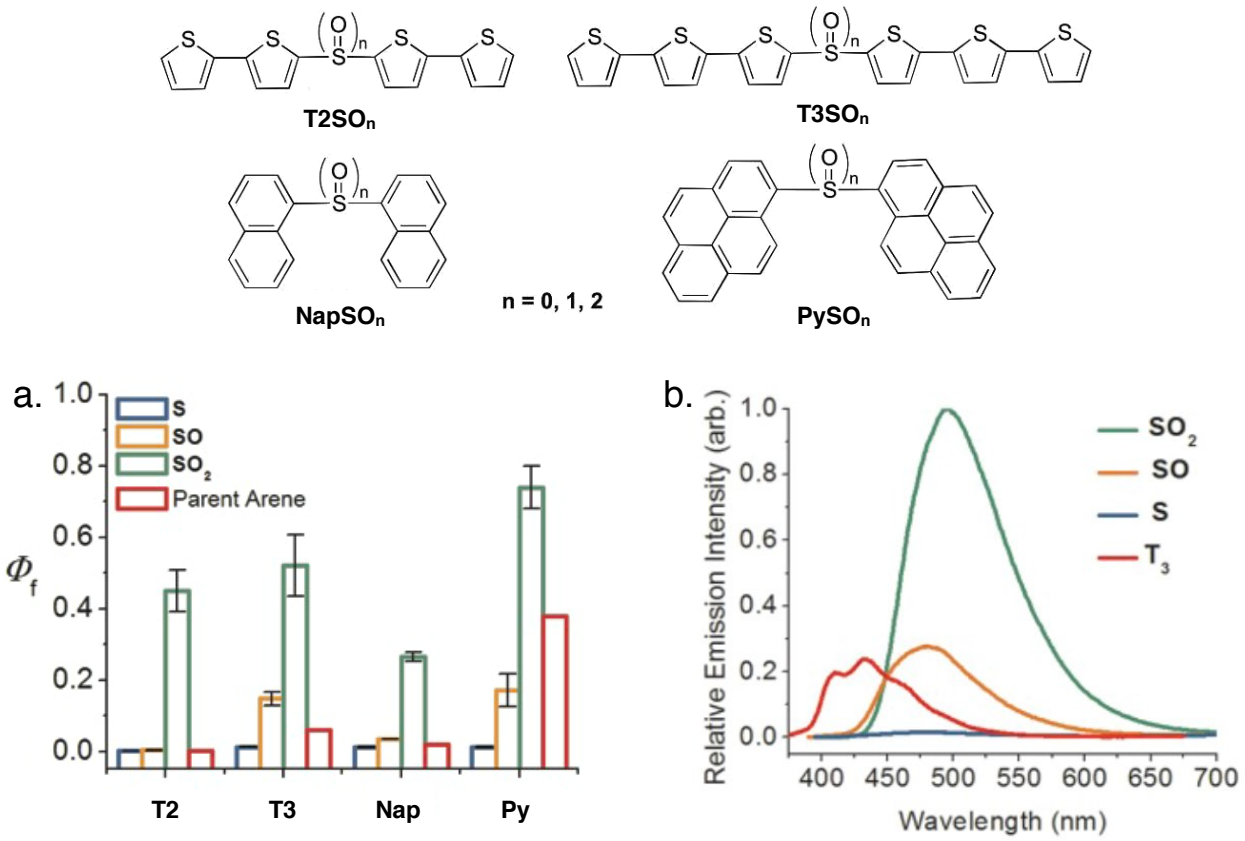

Figure 2.2. Structures of sulfur-bridged dimers which show increased photoluminescence quantum yields (Φ_f) as the oxidation state of the bridging sulfur is increased (a). (b) Photoluminescence spectra for **T3SO$_n$** compared to unsubstituted terthiophene (the "Parent Arene", **T3**).

By bridging two identical chromophores about a sulfur atom, a systematic enhancement of the photoluminescence quantum yield (Φ_{PL}) by oxidizing the bridging sulfur (S < SO < SO_2, Figure 2.2).[98] Increasing the oxidation state of the sulfur bridge also resulted in pronounced red-shifts of the PL spectra in polar solvents, an indication of increasing CT character. The observation that simply linking two light

absorbing molecules together could lead to new CT excited states and increase the PL yield by an order of magnitude raised several questions regarding the origin of the changes in spectroscopic behavior. The first question concerns the role of the sulfur linker: Does it actively participate in the electronic states, and why does its oxidation state have such a large effect? Related to this question, one may ask whether the second chromophore plays an important role. If the CT state involves only one of the chromophores and the bridging sulfur, then perhaps the second chromophore is not even necessary. The question of electronic structure is intimately related to the excited-state dynamics: How is the CT state formed and why is its relaxation different from that of a single chromophore? This class of sulfur bridged dimers, with potential applications in organic electronics, provides an ideal model system in which to study fundamental questions about the excited-state behavior in symmetric bichromophore systems. In this Chapter, optical spectroscopy (steady-state and time-resolved) and electronic structure theory are used to develop a complete picture of the photophysics, studying in detail the terthiophene dimers (**T3SO$_n$**). The following shows that the sulfur bridge itself does not significantly affect the excited-state structure, but the oxidation state of the sulfur bridge mediates the amount of electronic coupling between the two terthiophene chromophores. Using femtosecond transient absorption (TA) experiments, it is demonstrated that the initially excited state is a symmetric, delocalized excitonic state with an overall neutral character that relaxes within 10 ps to a second state, where the (asymmetric) CT character depends on the bridge oxidation state. This CT state has different radiative and intersystem crossing (ISC) rates when compared to monomeric terthiophene. Based on computational results, a mechanism is proposed in which electrostatic screening by lone pairs on the sulfur linker controls the CT character of the excited-state wave function. These results suggest that it is possible to use electron density on the bridge to mediate intermolecular (intra-dimer) interactions and tune the electronic coupling between identical chromophores without altering the dimer geometry or solvent polarity. The results presented in this Chapter not only reveal the origins of the novel properties of a specific class of bichromophores but also provide new directions for the design of symmetric chromophore systems that may find applications in fields ranging from artificial photosynthesis to organic electronics.

2.2 Synthesis of S-Bridged Dimers

Figure 2.2 shows the structures of four sulfur-bridged chromophore dimers. The organic chromophores bithiophene (**T2SO$_n$**), terthiophene (**T3SO$_n$**), naphthalene (**NapSO$_n$**) and pyrene (**PySO$_n$**) were chosen because the photophysics of the unsubstituted "parent arenes" are well known. The synthesis of these symmetric, sulfur-bridged dimers was achieved through a condensation reaction involving two equivalents of nucleophilic "monomer" (R-Li) and one equivalent of electrophilic sulfur (Scheme 2.1). For both bithiophene and terthiophene formation of the R-Li species was achieved through deprotonation of the terminal (alpha) C-H using *n*-butyllithium (*n*-BuLi) in tetrahydrofuran (THF). For **PyS** and **NapS** dimers 1-bromopyrene and 1-iodonaphthalene were reacted with *n*-BuLi to generate the corresponding R-Li nucleophiles. Bis-(phenylsulfonyl)sulfide was chosen as a convenient and clean (easy to work up) source of electrophilic sulfur. The sulfides (S) were isolated, purified, and portions of each sample were subjected to oxidation. Oxidation of the symmetrically bridged sulfides to their respective sulfoxides (SO) and sulfones (SO_2) was achieved using one or two equivalents, respectively, of the organic soluble oxidant meta-chloroperoxybenzoic acid (*m*-CPBA) in dichloromethane solution.

Scheme 2.1.General synthetic procedure for symmetric S-bridged dimers

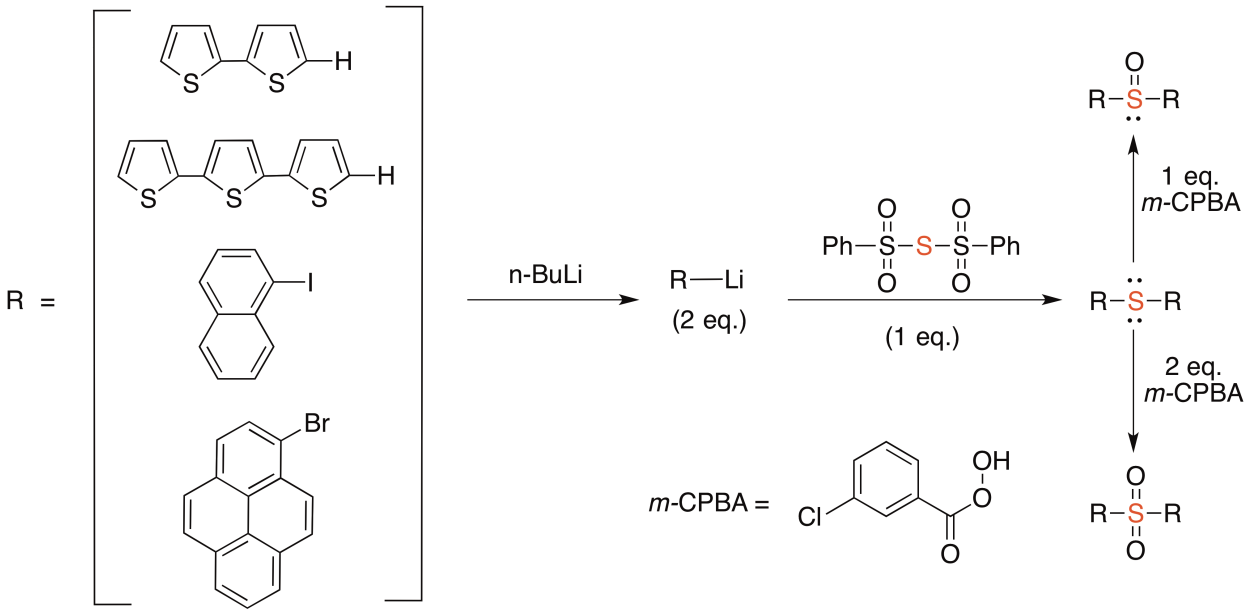

2.3 Photophysical Properties

2.3.1 UV-Vis Spectroscopy

The steady-state absorbance (UV-Vis) and photoluminescence (PL) data for all **RSO$_n$** are presented in Table 2.1 below. In general, by bridging two identical chromophores about a sulfur atom, the absorbance spectra, in particular the lower energy (π - π^*) transitions, are red-shifted relative to the parent arene (Figure 2.3). For instance, the S-bridged thiophenes (**T2SO$_n$** and **T3SO$_n$**) have absorbance maxima in between the unsubstituted parent arene and the fully conjugated dimers (**T2** = 305nm ,**T2SO$_n$** ~325-350nm, **T4**, λ_{max}= 377nm) and (**T3** = 349nm, **T3SO$_n$** ~370-400nm, **T6** λ_{max}= 432 nm). These absorption data are consistent with a weak interaction between bridged "monomers" about the sulfur atom in the ground state.

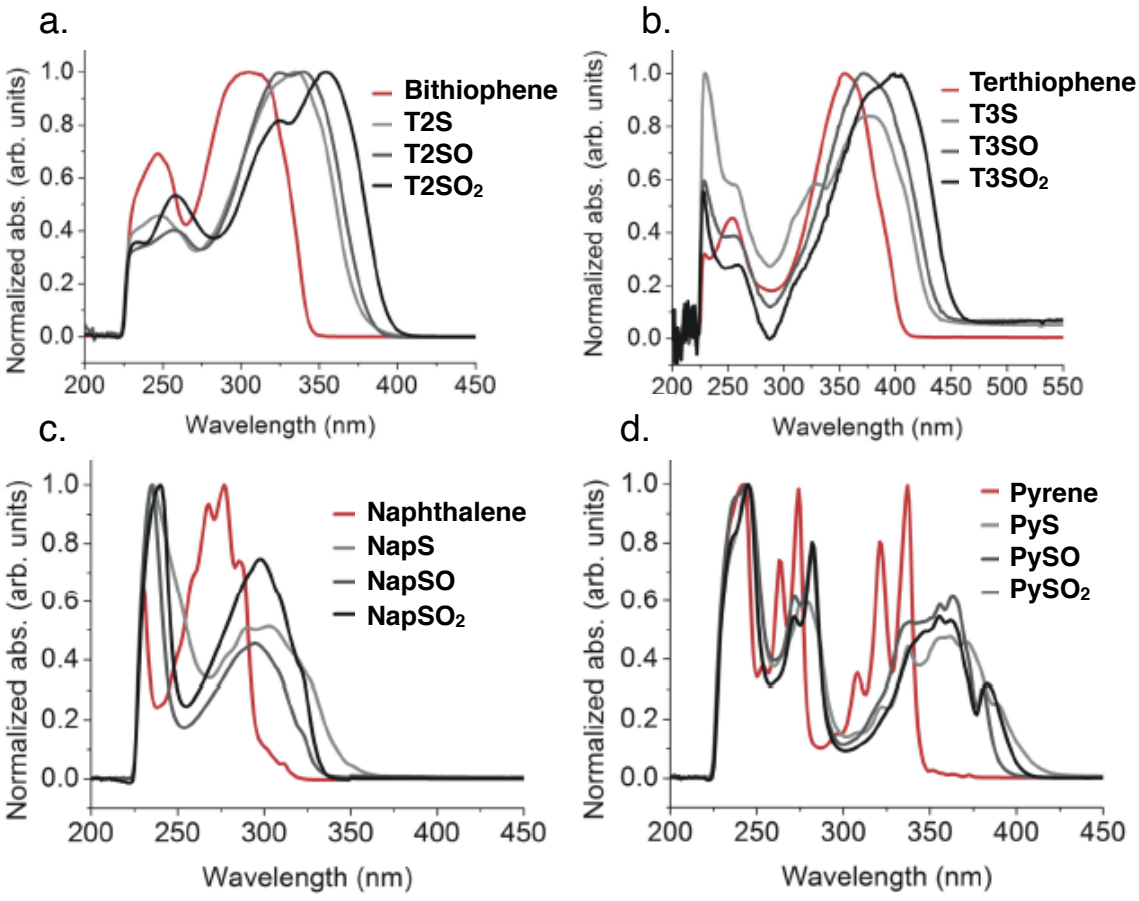

Figure 2.3.Absorbance spectra for all S-bridged dimers (**S**, **SO**, **SO$_2$**) in dilute (10^{-6} M) CH_2Cl_2 solutions showing the red-shifted profiles relative to the unsubstituted parent arenes.

2.3.2 Photoluminescence Spectroscopy

Likewise, the photoluminescence data show broad and red-shifted (lower energy) profiles compared to the unsubstituted parent arenes (Figure 2.4). Notably, as the oxidation-state of the bridging sulfur is increased from S, to SO, to SO_2 the PL intensity (quantum yield, Φ_f) increases by more than an order of magnitude (in dilute CH_2Cl_2 solutions). Additionally, for all **RSO_n** presented here, the PL quantum yields for the SO_2-bridged dimers are significantly higher than that of the unsubstituted parent arene. The photoluminescence for all S-bridged molecules presented here show short lifetimes (picoseconds to nanoseconds) and show no dependence on the presence of oxygen. The short lifetimes and the lack of oxygen dependence suggest that the observed photoluminescence is occurring from a singlet state (fluorescence) as opposed to a triplet state (phosphorescence).

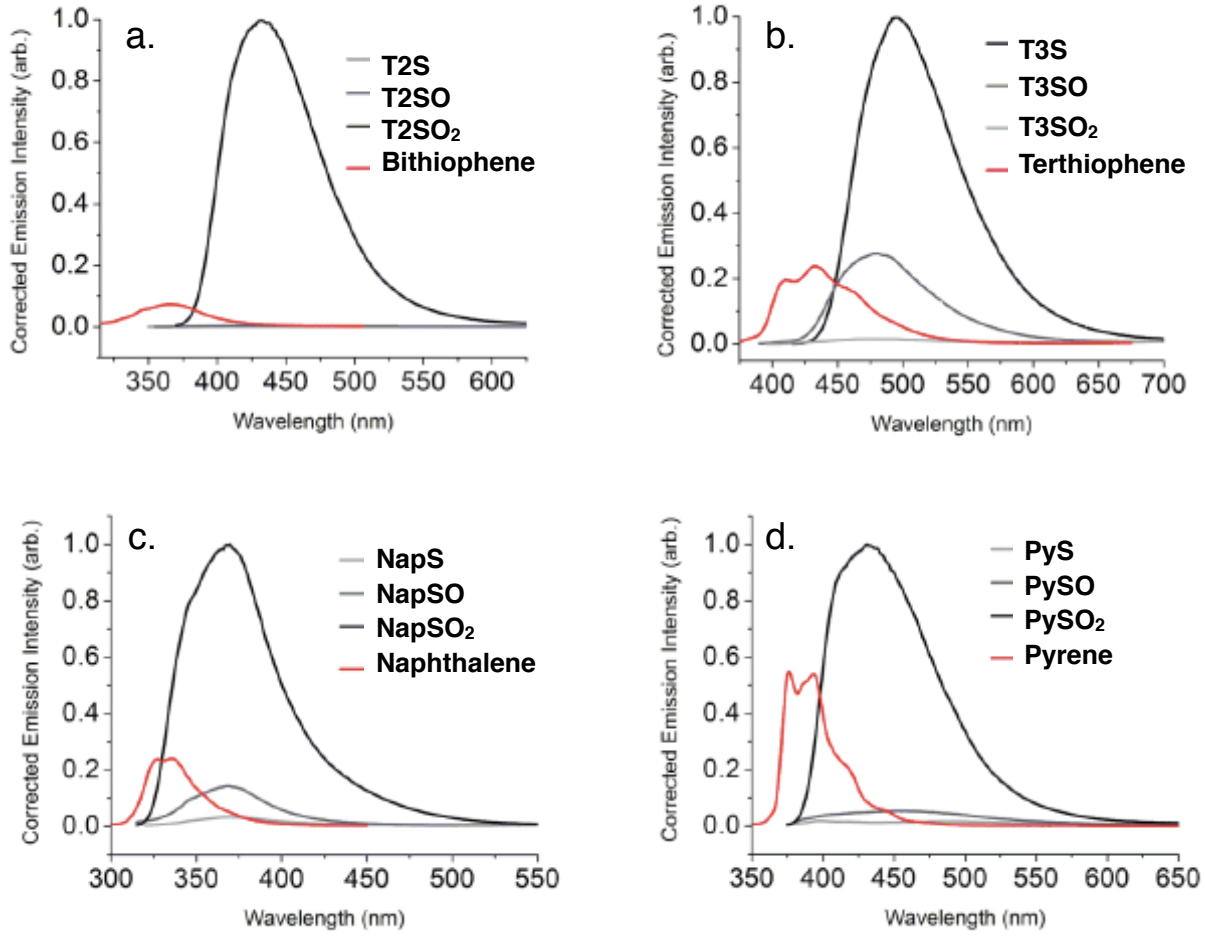

Figure 2.4. Photoluminescence spectra for all S-bridged dimers compared to unsubstituted parent arenes in dilute (10^{-6} M) CH_2Cl_2 solution showing the step-wise increase in PL intensity as the oxidation state of the bridging sulfur is increased (S < SO < SO_2).

Table 2.1. Summary of absorbance and photoluminescence data for all dimers compared to the unsubstituted parent arenes.

	Absorption		Photoluminescence	
Molecule	λ_{max} (nm)	ε (10^4 M^{-1} cm^{-1})	λ_{max} (nm)	Φ_{PL}
Bithiophene	305	1.3	365	0.001
T2S	334	3.4	383	0.002 ± 0.001
T2SO	325	2.9	447	0.003± 0.001
$T2SO_2$	349	3.2	430	0.45 ± 0.06
Terthiophene	349	2.5	432	0.06
T3S	374	5.8	473	0.012 ± 0.001
T3SO	371	5.3	479	0.15 ± 0.02
$T3SO_2$	398	4.3	495	0.52 ± 0.09
Naphthalene	277	0.8	355	0.02
NapS	302	1.3	368	0.012 ± 0.003
NapSO	296	1.3	368	0.035 ± 0.001
$NapSO_2$	298	1.0	368	0.27 ± 0.01
Pyrene	337	0.9	372	0.38
PyS	362	4.9	401	0.011 ± 0.002
PySO	351	4.6	449	0.17 ± 0.05
$PySO_2$	353	4.3	432	0.74 ± 0.06

2.3.3 Theory, Weakly Coupled Dimers

As a thought experiment, and to better understand the excited-state dynamics of the S-bridged dimers, each dimer is treated as a pair of weakly interacting molecules with a simplified four electron, four orbital analysis (**AA**, Figure 2.5). While this is indeed a simplified treatment of the excited-state dynamics, the UV-Vis absorption spectroscopy of all S-bridged dimers suggests only weak ground-state interaction between each half of the molecule. Accordingly, excitation of a weakly interacting dimer can result in promotion of an electron from the ground state to the excited state on one "half" of the molecule, or excitation of a single chromophore (**A*A** or **AA***).

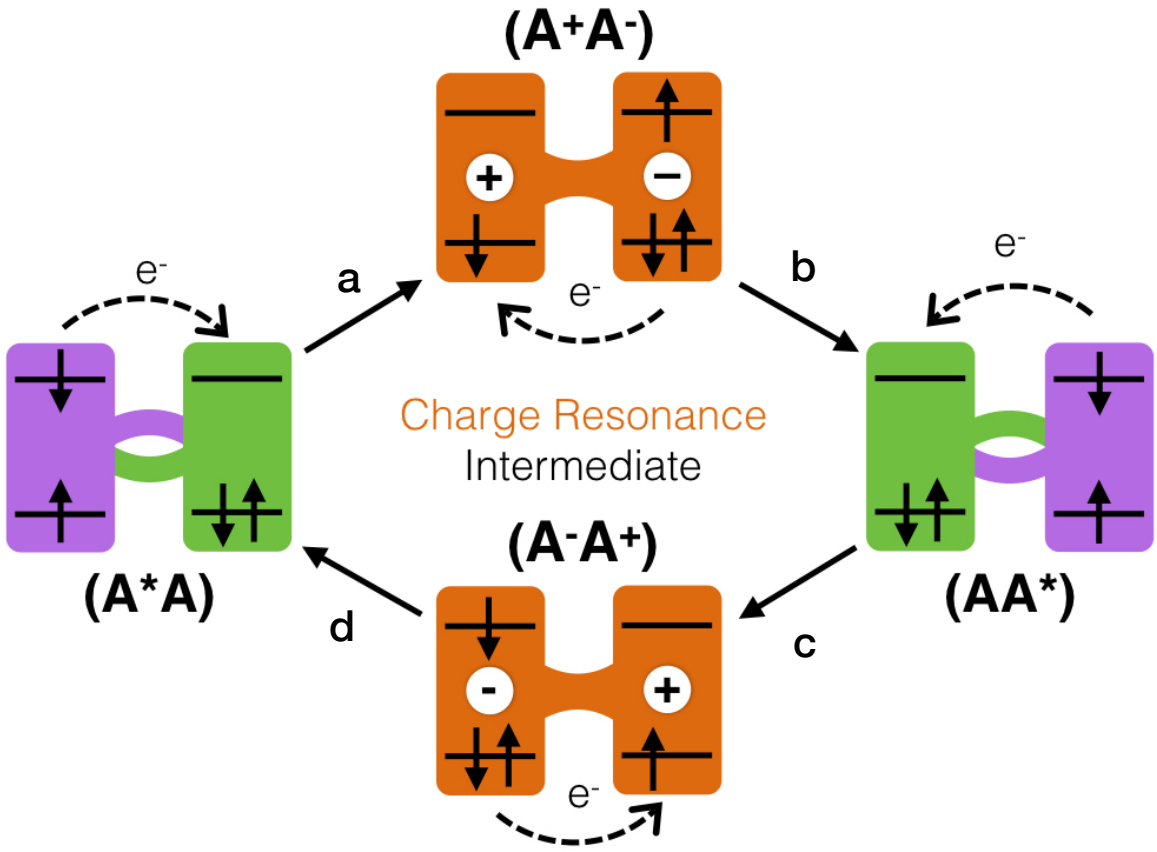

Figure 2.5. Illustration showing the simplified four electron, four orbital treatment of the S-bridged dimers. Each "monomer" within the dimer has a ground state and an excited state (4 orbitals). Initially (**AA**) the ground state configuration (green) is doubly occupied (top left, right). After light absorption excitation of the "left" or "right" half of the molecule is excited (**A*A** or **AA***, purple). These two (degenerate) localized excited states can be interconverted through a two-electron exchange (Dexter) mechanism (a-b and c-d) involving a charge transfer intermediate ($\mathbf{A^+A^-}$ and $\mathbf{A^-A^+}$, orange).

In the case of a symmetric dimer, the two possible (initially formed) excited states **A*A** and **AA*** are degenerate with one another and are therefore equally probable and indistinguishable. Additionally, **A*A** and **AA*** can interconvert with one another through a two-electron (Dexter) exchange mechanism (Figure 2.5 a-b and c-d), each pathway, involving a charge transfer (CT) intermediate ($\mathbf{A^+A^-}$ and $\mathbf{A^-A^+}$ respectively). Like the initially formed excited states (**A*A** and **AA***) the charge transfer intermediates ($\mathbf{A^+A^-}$ and $\mathbf{A^-A^+}$) are degenerate and indistinguishable from one another. As such, unless the excited state undergoes a desymmetrization event, by which one CT state becomes favored over another ($\mathbf{A^+A^-}$ and $\mathbf{A^-A^+}$ no longer degenerate), the overall excited-state character will remain neutral (non-polar, "charge

resonance" state). The prospect of a desymmetrized CT state is relevant here because it is known that CT states can have different rates of intersystem crossing than localized (neutral) states due to weaker orbital overlap (Fermi's Golden Rule). For most organic molecules, formation of a triplet state through ISC results in non-radiative decay, ultimately lowering the PL quantum yield. It is therefore possible that the observed increase in PL quantum yields for the S-bridged dimers ($S < SO < SO_2$) could be resulting from an increasing the amount of CT character in the excited state.

2.3.4 Photoluminescence as a Function of Solvent Polarity

The polarity of the excited state, in particular the state from which radiative decay (luminescence) occurs, can be probed by modifying the polarity of the surrounding medium (i.e. solvent polarity). To probe the nature of the excited state, specifically the presence of a charge transfer state, the photoluminescence of the S-bridged terthiophene dimers (**T3SO$_n$**) was measured in solvents of increasing polarity (Figure 2.6). The polar character of a CT state can be stabilized by polar solvents, which results in a decrease in energy. Accordingly, photoluminescence that involves contribution from a CT state will often show red shifted and broadened spectra. Figure 2.6 shows the PL spectra for all **T3SO$_n$** dimers, including unsubstituted **T3**, in solvents of increasing polarity. To achieve a range of solvent polarities, the solvents cyclohexane (non-polar), dichloromethane (moderately polar) and acetonitrile (polar) were chosen. As the oxidation state of the bridging sulfur is increased from S, to SO, to SO_2, the PL spectrum is increasingly red-shifted as the polarity is increased from cyclohexane to acetonitrile. These data suggest that as the oxidation state of the bridging sulfur is increased, the CT character of the emitting state also increases.

The degree of solvatochromism (red-shift induced by increasing solvent polarity) observed in the **T3SO$_n$** PL spectra can be quantified by calculating the Stokes shift, which is defined as the change in energy between the excitation energy (ν absorption) and the energy of the PL maximum (ν emission) (Figure 2.7). Furthermore, by plotting the Stokes shift ($\Delta\nu$) versus the solvent "polarizability" (Δf) the change in dipole from ground state to excited state ($\Delta\mu$) can be estimated using the Lippert-Mataga analysis (equation 2.1), which treats the solvated molecule as a polarizable sphere with radius a.[99,100] The

solvent polarizability (Δf) is a unit-less constant calculated as a function of the refractive index (η) and the dielectric constant (ϵ) of the medium (equation 2.2). From equation 2.1, the change in dipole moment is related to the slope of the linear fit of $\Delta\nu$ versus Δf by the solvent cavity (a), Planck's constant (h), the speed of light (c), and the dielectric permittivity of vacuum (ϵ_o).

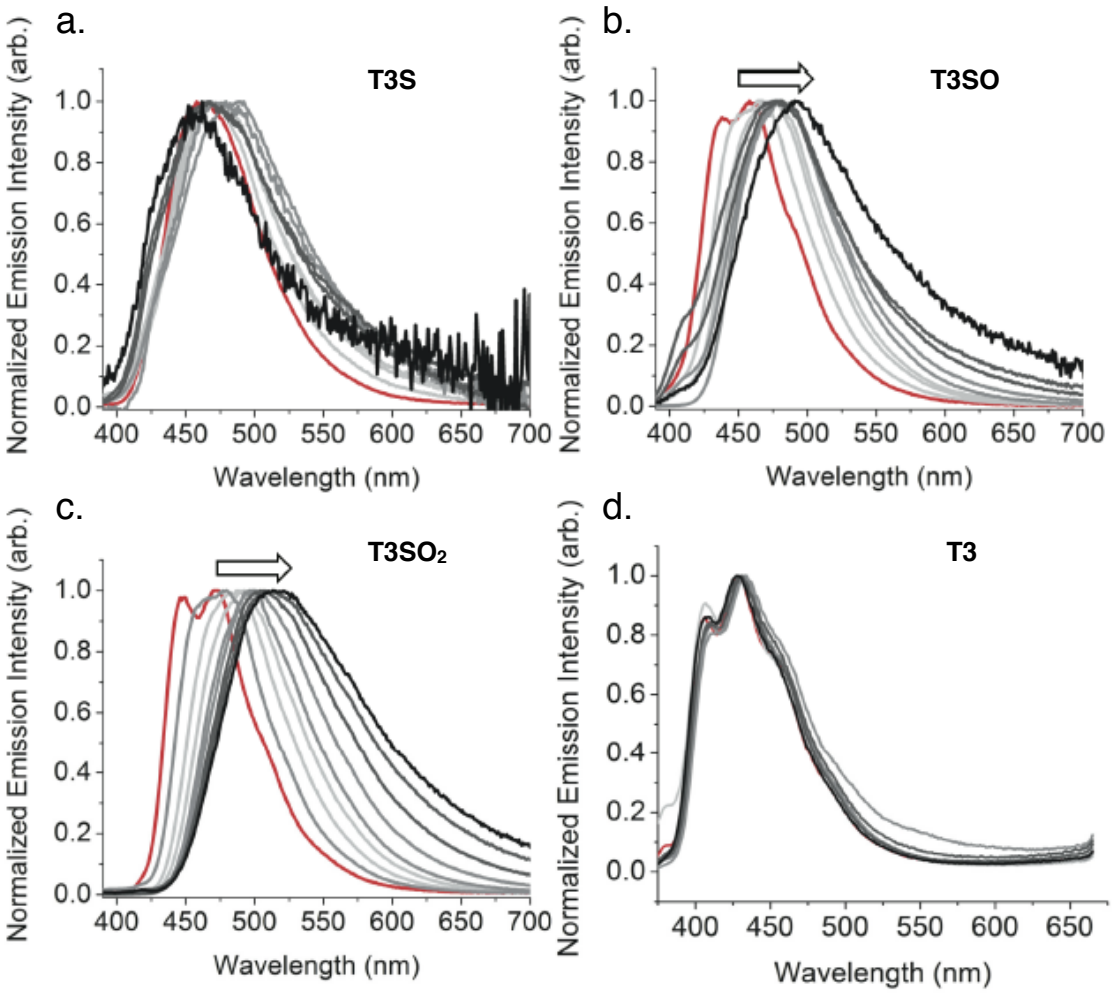

Figure 2.6. Photoluminescence spectra for **T3S** (a), **T3SO** (b), and **T3SO$_2$** (c) and unsubstituted **T3** (d) in solvent of increasing polarity (⟹)from non-polar cyclohexane (——) to polar acetonitrile (——).

The spherical solvent cavity (Onsager radius, a)[101] is estimated using the molecular weight (M) of the solute as well as Avogadro's number (N) and an assumed molecular density (d) of 1 g/cm^3 (equation 2.3). According to equation 2.1 the calculated change in dipole from ground-state to excited state ($\Delta\mu$) is 2.2 Debye for **T3SO** and 2.7 Debye for **T3SO$_2$**.

(2.1) $$\Delta\nu = \frac{2(\Delta\mu)^2}{\epsilon_o hca^3}\Delta f + \Delta\nu^o$$

(2.2) $$\Delta f = \frac{\epsilon-1}{2\epsilon+1} - \frac{\eta^2-1}{2\eta^2+1}$$

(2.3) $$a = \left(\frac{3M}{4N\pi d}\right)^{\frac{1}{3}}$$

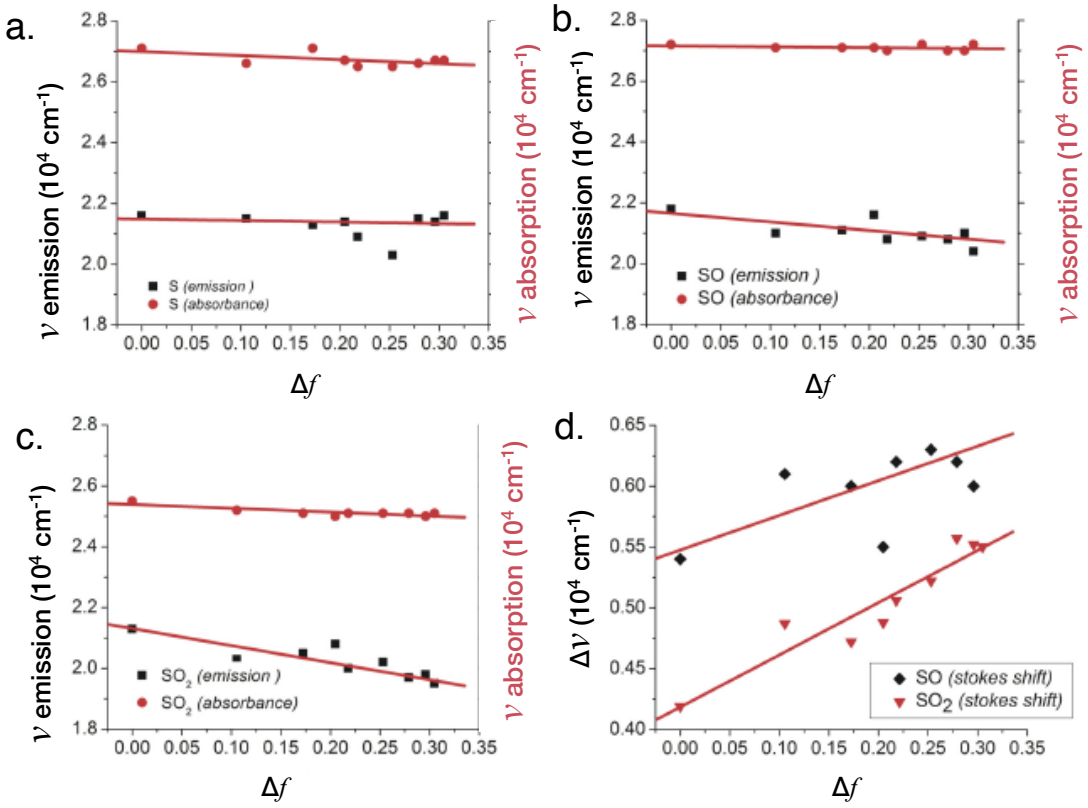

Figure 2.7. Plots showing the change in absorbance energy (ν absorbance) and the energy of the PL maximum (ν emission) versus the solvent polarizability (Δf) for **T3S** (a), **T3SO** (b), and **T3SO$_2$** (c). (d) Plot showing the linear relationship between Stokes shift ($\Delta\nu$) against the solvent polarizability (Δf).

2.4 Model Monomers

If charge transfer plays a role in the increased photoluminescence, there are a few pressing questions that result. Does sulfur actively participate in the electronic states, and why does its oxidation state have such a large effect? Next, is the dimeric structure necessary for achieving CT or is it simply the

presence of the sulfur functional group? To address these questions, a series of synthetic analogues to the **T3SO$_n$** dimers was synthesized such that the sulfur functionality was maintained but the second terthiophene was replaced with a methyl group (**T3SO$_n$Me**, Figure 2.8).

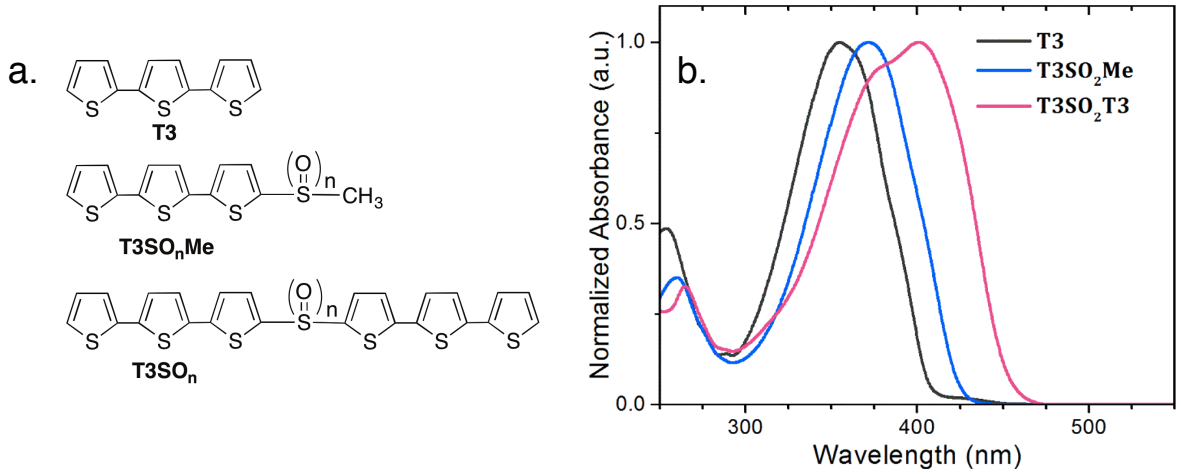

Figure 2.8. (a) Structures of unsubstituted **T3**, the "monomers" **T3SO$_n$Me** and the dimers **T3SO$_n$** and (b) the UV-Vis spectra of the SO_2 containing monomers and dimers versus unsubstituted **T3**.

2.4.1 Monomer vs. Dimer Absorption

The UV-Vis absorption spectra of **T3**, **T3SO$_2$Me** , and **T3SO$_2$** in dichloromethane are shown in Figure 2.8. When a methyl-terminated SO_2 linker is added to **T3** (**T3SO$_2$Me**), the absorption peak shifts from 350 nm to 370 nm, but the overall peak shape remains the same, and there is no discernible broadening. The same is true for the S and SO linkers. When the methyl group is replaced by a second **T3** (**T3SO$_2$**), the absorption not only redshifts farther but also broadens considerably, with two distinguishable peaks at 400 and 375 nm. This change in the absorption line shape is the first clue that the **T3-T3** electronic interaction plays an important role. Similar changes in absorption line-shapes are observed for all **T2SO$_n$** and **T3SO$_n$** dimers (Figures 2.3 and 2.8). Since the lowest-energy transition for all **T3SO$_n$** species (~ 400 nm) is higher in energy than that of sexithiophene (**T6**, ~ 435 nm),[102,103] the electronic interactions in these dimers are not as strong as in a fully conjugated system. Although the absorption spectra of the **T3SO$_n$** dimers are sensitive to the presence of the second **T3**, they are not very

sensitive to solvent polarity. The splitting of the dimer absorption spectra likely originates from through-space Coulombic interactions between the two **T3** chromophores (Figure 2.9).

2.4.2 Sulfur Oxidation State Controls Coulombic Coupling

The two bands observed in the absorbance spectra of **T3SO$_n$** are attributed to interacting transition dipoles of the two monomers resulting in exciton splitting (E1 and E2, Figure 2.9).[104,105] The low-energy bands in the absorption spectra of the **T3SO$_n$** dimers can be fit using a pair of Gaussians, allowing us to estimate values for the excitonic splitting energy Δε. The estimated splitting (Δε) increases with sulfur oxidation state (Δε = 1870 cm^{-1} for **T3S**, Δε = 2050 cm^{-1} for **T3SO**, and Δε = 2150 cm^{-1} for **T3SO$_2$**). This interaction between **T3** units is slightly smaller than the H-type aggregate coupling typically seen in oligothiophene crystals, in which the chromophores have an approximately parallel orientation.[106] The exciton splitting energy Δε can be estimated in each of the absorption spectra by using equation 2.4 to describe the interaction of two point dipoles A and B.

In equation 2.4, μ is the transition dipole moment, r_{AB} is the center-to-center vector between dipoles, α is the angle between the dipoles, and θ is the angle between the transition dipole moment and r_{AB}. Using equation 2.1, with values of r_{AB}, α , and θ (from computational results and X-ray crystallographic data)[107] and μ for unsubstituted terthiophene,[108] the calculated values for the exciton splitting energies are: Δε = 2000 cm^{-1} for **T3S** , Δε = 2100 cm^{-1} for **T3SO**, and Δε = 1900 cm^{-1} for **T3SO$_2$**. All the values are close to 2000 cm^{-1} , consistent with the experimental results. This is somewhat surprising, considering that the point dipole approximation of equation 2.4 tends to overestimate Δε for chromophores in close proximity.[109,110,111,112] The calculations predict no systematic increase in Δε from **T3S** to **T3SO$_2$** because the molecular geometries are quite similar. However, equation 2.4 only considers through-space dipole− dipole interactions, and it is known that electron-transfer terms can also contribute to excitonic splittings.[113,114,115,116] Comparing the calculated exciton splitting energy with those determined experimentally, it appears that such electron-transfer contributions to Δε may play a larger role as the sulfur oxidation state is increased.

(2.4) $$\Delta\varepsilon = \frac{2\,|\mu|^2}{|\vec{r}_{AB}|^3}(\cos\propto + 3\cos^2\theta)$$

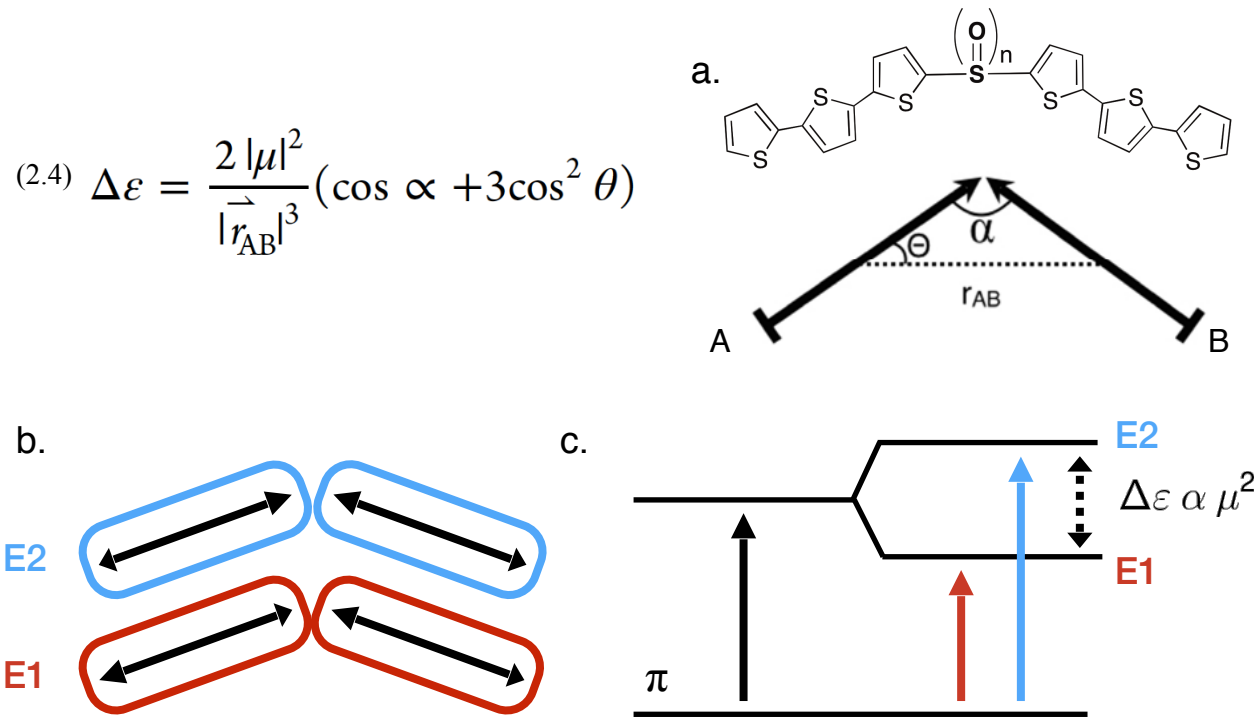

Figure 2.9. Theory behind exciton splitting for "obliquely" oriented transition dipoles (**A** and **B**). Equation 2.4 describes the relationship between the magnitude (μ) and orientation of two transition dipoles (**A** and **B**) and the exciton splitting energy (Δε). (a) Shows the relative orientation of transition dipoles **A** and **B**, for S-bridged dimers (**T3SO$_n$**). (b) Shows the "head to tail" (E1) and "head to head" (E2) interactions that can result from two obliquely oriented dipoles, resulting in a splitting in the π - π* transition (c).

2.4.3 Monomer vs Dimer Photoluminescence.

The steady-state PL spectra of **T3SO$_2$Me** and **T3SO$_2$** are compared in non-polar cyclohexane, moderately polar dichloromethane, and highly polar acetonitrile (Figure 2.10). Increasing the solvent polarity for the monomer (**T3SO$_2$Me**) solutions results in only a small red-shift, with no change observed between moderately polar dichloromethane and polar acetonitrile. Similar behavior is observed for the S and SO linkers. When the dimer (**T3SO$_2$**) is examined, however, a ~100 nm red shift in the PL maximum is observed when the solvent polarity is increased from non-polar cyclohexane to highly polar acetonitrile (Figure 2.10b). In the same solvents, the dimers (**T3SO$_n$**) display relatively broad and red-shifted profiles. These results reinforce the conclusion that, while the absorption spectra of **T3SO$_n$** are relatively insensitive to solvent, the fluorescence spectra of the dimers show strong solvatochromism. The results

with the **T3SO$_n$Me** monomers demonstrate that the CT character of the emitting state arises from the presence of the second **T3** chromophore and not from the linker itself. Finally, the degree of dimer solvatochromism depends on the linker oxidation state, with the SO_2 linker showing the largest shift and the S linker showing much smaller shifts.

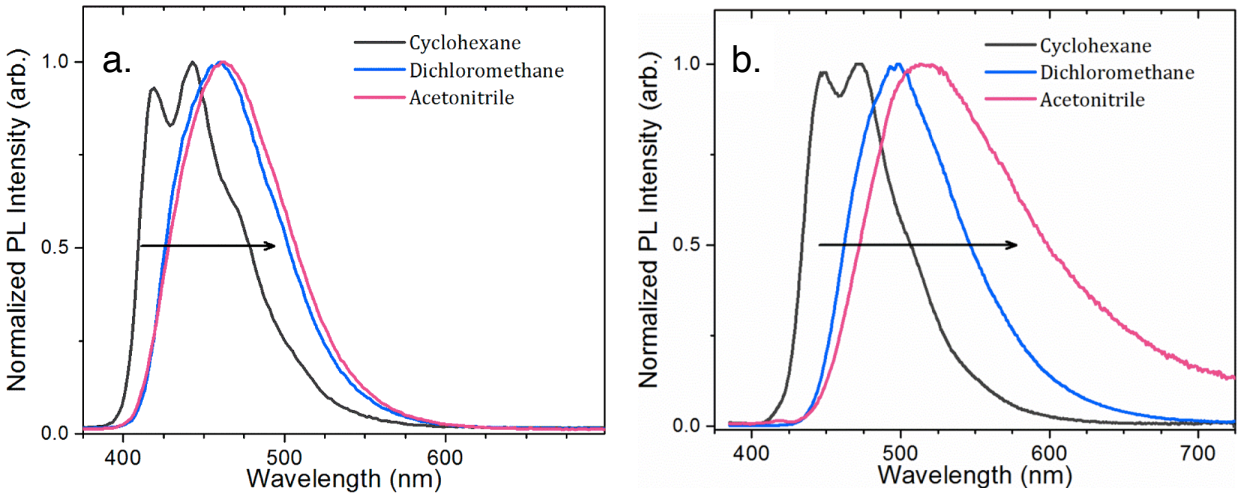

Figure 2.10. Photoluminescence spectra for the monomer (a) **T3SO$_2$Me** compared to the dimer (b) **T3SO$_2$** in solvents of increasing polarity.

2.4.4 Monomer vs. Dimer Photoluminescence Lifetimes

Additional information regarding the role of the second terthiophene and the oxidation state of the sulfur bridge were obtained by measuring the photoluminescence lifetimes (Figure 2.11, τ_{PL}). Unsubstituted **T3** has a relatively short PL lifetime (τ_{PL} = 190 ps), due to rapid intersystem crossing (ISC) to its triplet state.[117,118] When the SO$_n$Me group is added, the PL lifetimes change very little. Accordingly, the monomers in dichloromethane solutions have a τ_{PL} which varies only slightly depending upon the oxidation state of the sulfur, with a slight increase observed with increasing oxidation state (171 ps for **T3SMe**, 195 ps for **T3SOMe**, and 219 ps for **T3SO$_2$Me**). The lifetimes of all of the monomers are not appreciably different from that of unsubstituted **T3** and do not show a strong solvent dependence.

When the terminal methyl substituent is changed to **T3**, however, there is a significant increase in the fluorescence lifetime, as shown in Figure 2.11a. The different bridge oxidation states also give rise to

different lifetimes in the dimers, as shown in Figure 2.11b. In all solvents, the lifetimes of the unoxidized sulfur-bridged dimer **T3S** are consistently shorter than those of the sulfoxide **T3SO**, which in turn are shorter than those of the sulfone **T3SO$_2$**.

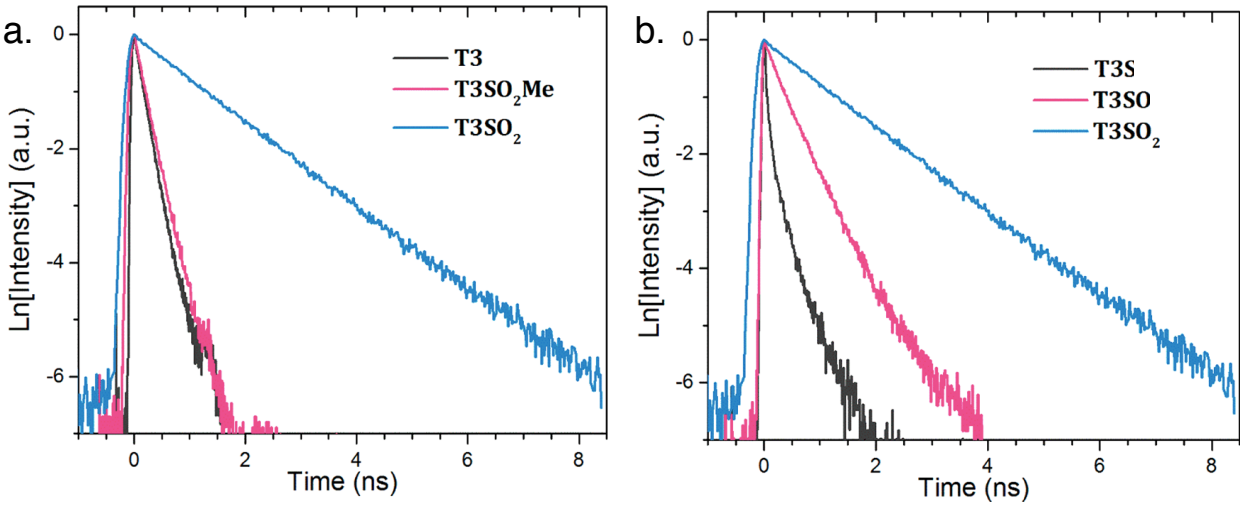

Figure 2.11. Photoluminescence lifetimes of **T3**, **T3SO$_2$Me** and **T3SO$_2$** (a), and **T3SO$_n$** (b) in dichloromethane.

A summary of the photoluminescence quantum yields (Φ_{PL}), photoluminescence lifetimes (τ_{PL}) and calculated radiative lifetimes (τ_{rad}) are presented in Table 2.2. Of the compounds studied, only **T3S** deviated from mono-exponential decay behavior, requiring a minor (~15%) second component when fit to a bi-exponential function (Table 2.2 footnote). A stretched exponential function could also be used, but since there is some evidence that two different conformers may be present (see Theory section), a bi-exponential is more justified physically. Despite this complication, the average fluorescence lifetime of **T3S** fits well with the trend observed in Figure 2.11. The radiative lifetime τ_{rad} of **T3SO$_2$** (Table 2.2) increases with solvent polarity, consistent with a loss of oscillator strength in more polar solvents. This decrease in oscillator strength is concordant with an increasing degree of charge separation and is another hallmark of a CT state.[119,120] The effect of the oxidation state of the bridging sulfur group on the emission lifetime is similar for both the monomers and dimers, in that increasing the oxidation state from S to SO_2 results in an increase in the observed τ_{PL}. However, the trend is much more pronounced in the bridged

dimers. In general, a higher oxidation state for the bridge leads to a more pronounced solvatochromic character of the emitting state as well as longer lifetimes and higher quantum yields.

Table 2.2. Photoluminescence quantum yields (Φ_{PL}), photoluminescence lifetimes (τ_{PL}), and radiative lifetimes (τ_{rad}) for **T3SO$_n$** as a function of solvent polarity.

		Molecule		
Solvent	Parameter	**T3S**	**T3SO**	**T3SO$_2$**
Acetonitrile	Φ_{PL}	0.007 ± (0.001)	0.026 ± (0.005)	0.14 ± (0.03)
	τ_{PL} (ps)	120	270	650
	τ_{rad}[a] (ps)	17,000 ± (3000)	11,000 ± (2000)	5,000 ± (1000)
Dichloromethane	Φ_{PL}	0.012 ± (0.001)	0.15 ± (0.02)	0.52 ± (0.09)
	τ_{PL} (ps)	90	400	1400
	τ_{rad}	7500 ± (600)	2700 ± (400)	2700 ± (500)
Cyclohexane	Φ_{PL}	—	—	0.14 ± (0.03)
	τ_{PL} (ps)	—	—	250
	τ_{rad} (ps)	—	—	2000 ± (500)

[a] τ_{rad} calculated by τ_{PL} / Φ_{PL}.
*Weighted average of two components (58.7 ps (86%) and 475.3 ps (14%)).
**Weighted average of two components (49.2 ps (85%) and 297.8 ps (15%)).

2.5 Femtosecond Transient Absorption Spectroscopy

The results presented in the preceding sections indicate that the excited state character of the dimers changes between the absorption and emission events. The absorbing state has an overall neutral character, as inferred from its lack of solvatochromism. The emitting state, on the other hand, has pronounced CT character that is strongly influenced by both solvent polarity and the oxidation state of the bridge. In order to understand how these two excited states are connected, femtosecond transient absorption (TA) measurements were performed. The femtosecond TA of unsubstituted **T3** in solution has been measured previously.[121]

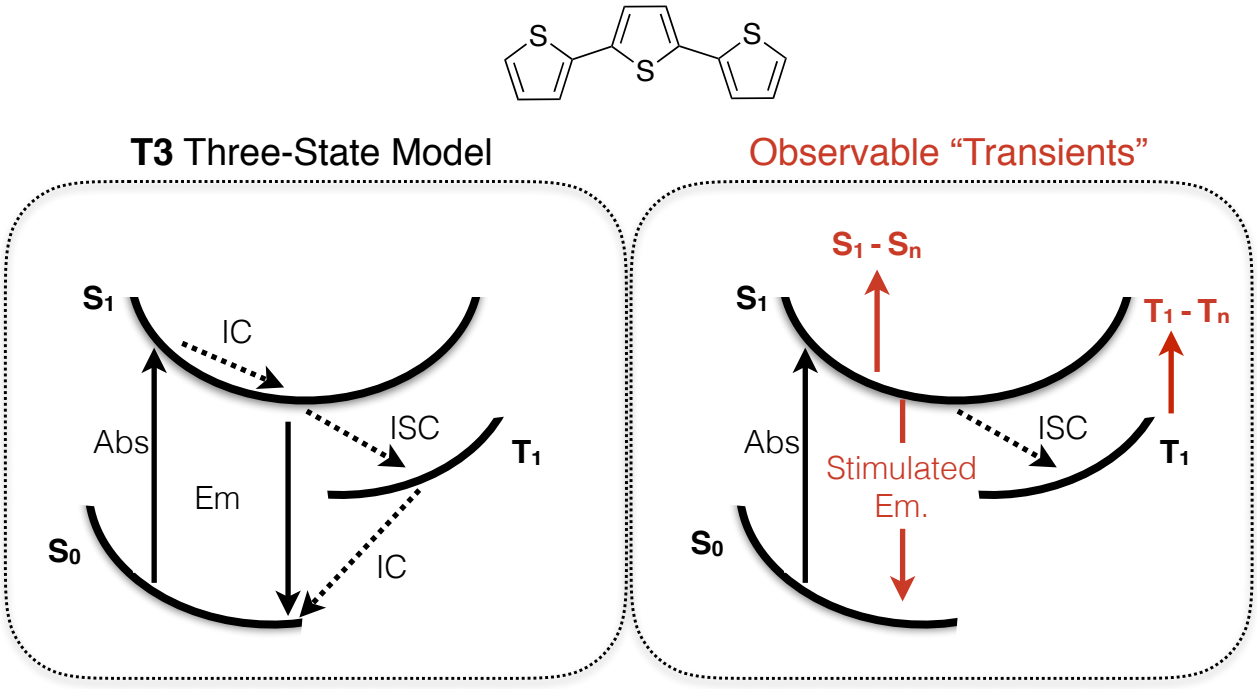

Figure 2.12. (a) Potential energy surfaces illustrating the typical three-state model for unsubstituted terthiophene (**T3**), absorption (Abs.) from ground state to excited state (S_0 - S_1) followed by internal conversion (IC) to the lowest energy S_1 state (Kasha's rule) to yield either radiative decay back to S_0 (emission, Em.) or intersystem crossing from singlet to triplet (T_1) from which non-radiative, internal conversion back to S_0 occurs. (b) Observables ("transients") of the three-state model in a typical time resolved absorption (TA) experiment.

2.5.1 Excited State Dynamics of T3SO$_n$Me Monomers

For unsubstituted **T3**, an initial singlet $S_1 \rightarrow S_n$ excited-state absorption in the visible spectrum decays to a signature $T_1 \rightarrow T_n$ triplet absorption on the same time scale as the PL decay. The photophysical behavior is consistent with that of a simple three-state system: absorption from S_0 to S_1, followed by ISC from S_1 to T_1 on a 190 ps time scale (Figure 2.12). The T_1 state then survives for nanoseconds before decaying back to S_0. The TA spectra of the **T3SO$_n$Me** monomers show similar behavior to unsubstituted **T3**. At early times (t < 100 ps), the **T3SO$_2$Me** monomer shows a negative feature at 490 nm (Figure 2.13a), corresponding to stimulated emission, as well as a positive feature at ~595 nm assigned to the singlet induced absorption ($S_1 \rightarrow S_n$). At longer times (t > 100 ps), the triplet induced absorption ($T_1 \rightarrow T_n$) grows in at ~500 nm, while the $S_1 \rightarrow S_n$ feature and the stimulated

emission both decay. The positive feature at 500 nm is assigned to the triplet since in **T3** the $T_1 \rightarrow T_n$ absorption is located at ~470 nm.[41,122] The redshift of the $T_1 \rightarrow T_n$ feature is expected because the T_n states tend to be less localized than T_1 and undergo a greater bathochromic shift upon substitution with electron-donating and -withdrawing groups.[123] The spectra in Figure 2.13a show an approximate isosbestic point at 545 nm, that suggests the dominant relaxation process occurs between two well-defined electronic states.

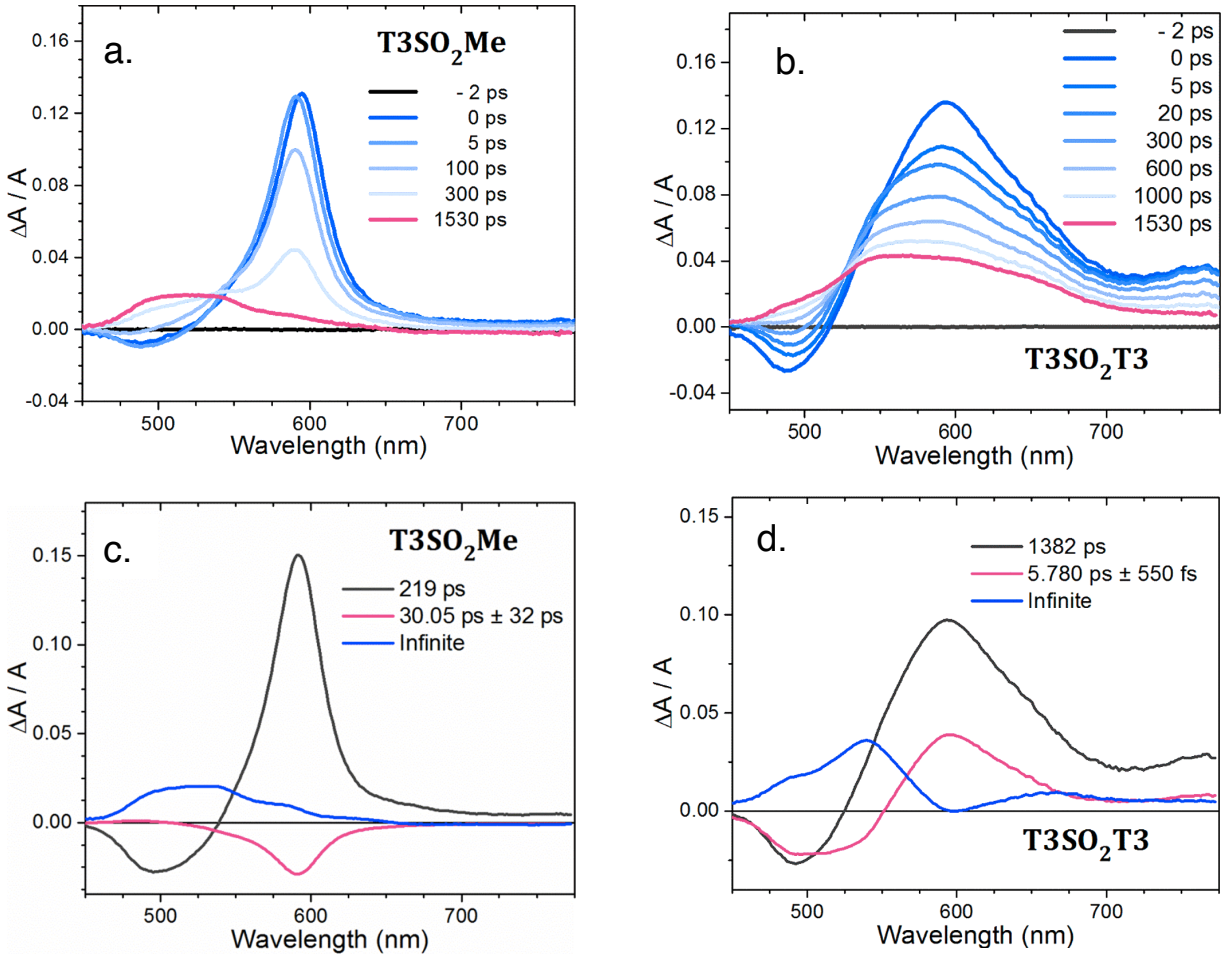

Figure 2.13. Transient absorption data for monomer **T3SO₂Me** (a) and dimer **T3SO₂** (b) in dichoromethane. Pre-exponential amplitudes obtained from Global fit analysis for monomer **T3SO₂Me** (c) and dimer **T3SO₂** (d).

Using a principal component analysis, combined with a global fitting algorithm, the data in Figure 2.14a can be described using three components linked by two relaxation times τ_1 = 30 ps and τ_2 = 219 ps (Figure 2.13c). The latter time is just the measured fluorescence decay time and reflects the ISC time in this molecule. The 30 ps time describes a small shift in the $S_1 \rightarrow S_n$ absorption peak and probably reflects conformational relaxation or solvent reorganization. The amplitude of the pre-exponential factor that corresponds to this time is < 20% of the initial component.

2.5.2 Excited State Dynamics of T3SO$_n$ Dimers

In the **T3SO$_n$** dimers the behavior is more complicated (Figure 2.13b). All three compounds in dichloromethane show a much broader $S_1 \rightarrow S_n$ absorption that extends from the visible through the near-infrared, with a peak at ~600 nm and a second feature near 750 nm. As in the methyl-terminated compounds, the $S_1 \rightarrow S_0$ stimulated emission around 490 nm is eventually replaced by an induced absorption that is assigned to the triplet $T_1 \rightarrow T_n$ transition. For all three compounds, however, there is no clear isosbestic point because the induced absorption at 600 nm undergoes a rapid blueshift which is much more pronounced than in the monomer. For all three **T3SO$_n$** dimers, global analysis required a minimum of three components with two time constants (Figure 2.13d). There is a fast (5−10 ps) component, followed by a slower component where the relaxation time mirrors the fluorescence decay time. The third component is strongly peaked around 500 nm, suggesting that it is associated with the triplet state (T_1). In all three **T3SO$_n$** dimers, the fast component is comparable in magnitude to the other components, unlike in the monomer, where it leads only to a small spectral shift. The TA kinetic parameters for the **T3SO$_n$** dimers and the sulfone-bridged monomer **T3SO$_2$Me** in dichloromethane are summarized in Table 2.3.

The important conclusion (Table 2.3) is that excited-state relaxation in the dimers appears to occur in two steps: fast relaxation from the absorbing state (S_1) to an intermediate state (S_1*), followed by slower relaxation from S_1* to the triplet (T_1) and S_0 (ground) states. The fluorescence behavior of the **T3SO$_n$** dimers is dominated by the relatively long-lived S_1* state (as reflected by τ_2 Table 2.3).

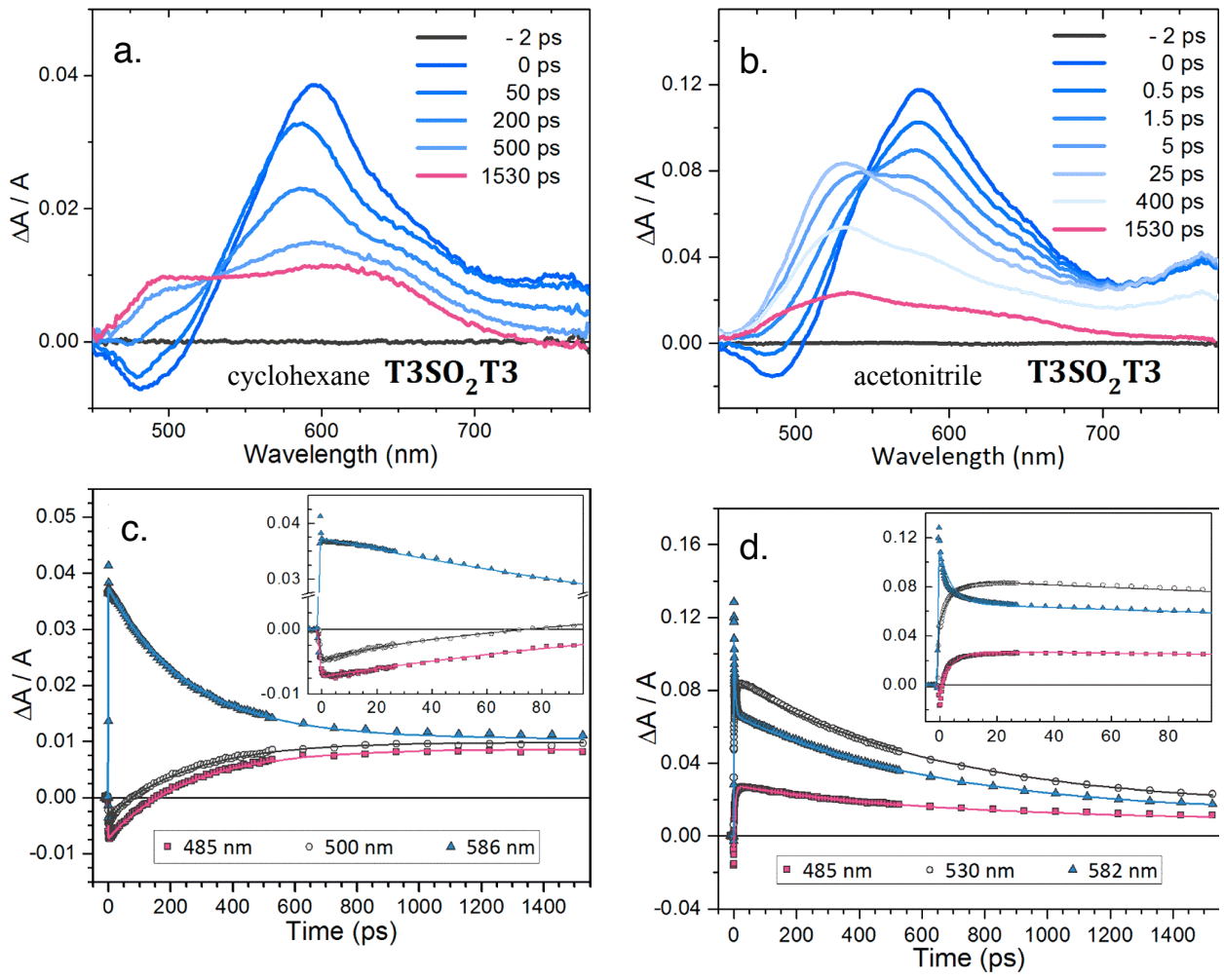

Figure 2.14. Transient absorption data for **T3SO₂** in cyclohexane (a), and acetonitrile (b) and the corresponding single wavelength kinetic traces (c,d respectively). Insets show the early time (100 ps) evolution of the kinetic traces.

Table 2.3. Transient absorption lifetimes (τ) for all **T3SOₙ** dimers compared to the monomer **T3SO₂Me**.

	Molecule			
	T3S	**T3SO**	**T3SO₂**	**T3SO₂Me**
τ_1 (ps)	5	9	6	30
τ_2 (ps)	50	400	1400	200

2.5.3 Excited State Dynamics as a Function of Solvent Polarity

The solvent polarity was varied in order to probe the CT character of the S_1* intermediate state. There is little dependence upon solvent polarity observed in the TA spectra of the **T3SO$_n$Me** monomers. The spectral evolution of **T3SO$_2$** in non-polar cyclohexane (Figure 2.14) is strongly reminiscent of that seen in **T3SO$_2$Me**, albeit with a broader $S_1 \rightarrow S_n$ absorption feature (~600nm) that extends into the near-infrared region. There is a recognizable isosbestic point located at 530nm as the $T_1 \rightarrow T_n$ absorption grows in (~490 nm). A global fitting analysis yields only two components linked by a relaxation time of 265 ps, the experimentally measured fluorescence lifetime. The single wavelength traces in Figure 2.14c show only a decay and concomitant rise in the $T_1 \rightarrow T_n$ absorption. Thus, in non-polar cyclohexane, **T3SO$_2$** behaves like monomeric **T3** and the methyl-terminated bridge compounds with a one-step population transfer between S_1 and the triplet manifold. The dynamics are qualitatively different for **T3SO$_2$** in acetonitrile (Figure 2.14b). In this solvent, a clear isosbestic point is also observed, shifted to 570 nm. A global analysis of the two principal spectral components yields three fit parameters. The amplitude of the pre-exponential coefficient that corresponds to the isosbestic point at 570 nm is peaked at 525 nm and forms within 2.8 ± 1.1 ps. This feature then decays with the measured fluorescence lifetime of 646 ps. The rapid growth of the intermediate state can also be seen in the single wavelength traces in Figure 2.13d, where a clear increase in the signal is resolved at 530 nm, which then decays on a much slower time scale, close to the fluorescence decay time. Comparing the cyclohexane and acetonitrile data, it appears that the energetic separation of S_1* from S_1 depends on solvent polarity, and, in the most polar solvent (acetonitrile), relaxation to the S_1* state leads to the appearance of a distinct electronic absorption feature (530 nm). Accordingly, S_1* must correspond to a state with a high degree of charge separation that is stabilized by the surrounding medium. This S_1* state is also most pronounced for **T3SO$_2$**. Similar relaxation dynamics are observed for **T3S** and **T3SO** in acetonitrile: the intermediate S_1* states are formed on comparable time scales (3.4 and 4.7 ps, respectively) but are not as pronounced spectrally.

2.6 Calculations

2.6.1 Conformational Flexibility

In order to gain insight into the nature of the dimer excited states TDDFT calculations were performed. One concern is that the molecules used in this study are relatively large and incorporate flexible linkers, which could lead to conformational disorder and distributed kinetic behavior. To address this concern, the ground-state potential energy surfaces for bending and torsion of the dimers were computed (Figure 2.15). In all cases the barriers are substantially higher than *kT*, the thermal energy. Note that even though the barriers to rotation are high, the energy difference between rotational conformers (*cis* and *trans*) can be small, which is why both conformers are considered when calculating excitonic energy splittings.

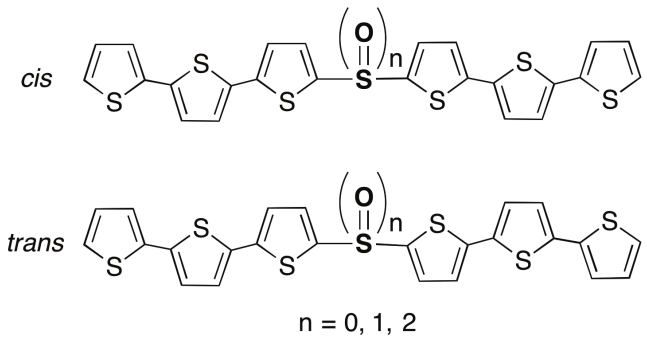

Figure 2.15. Structures of the computed *cis* and *trans* conformers.

The fact that almost all the fluorescence decays and TA data in the preceding sections could be fit with single exponentials provides experimental evidence that the spectroscopic behavior of these conformers must be quite similar. The only exception is the **T3S** dimer, which had a minor (~ 15%) long-lived component in its fluorescence decays, suggesting that *cis* and *trans* isomers may have different relaxation dynamics in this molecule. Overall, both experiment and theory suggest that conformational disorder does not play a decisive role in the observed dynamics.

2.6.2 Calculated Electronic Structure of Monomers and Dimers

Of particular interest is the electronic structure of both the S_1 and S_1* states. Electronic structure calculations indicate that in all cases, the optical excitations correspond to a $\pi \rightarrow \pi^*$, HOMO-to-LUMO transition. Starting with the optimized ground-state geometries, the computed vertical transition energies of **T3** and **T3SO$_n$** are in reasonable agreement with the experimental absorption maxima in dichloromethane and properly reflect the relative shift observed when increasing the oxidation state of the linker. The absorption redshift of **T3SO$_n$Me** with respect to **T3** can be rationalized, to a first approximation, as a result of LUMO stabilization due to the bonding interaction of the **T3** fragment with the SO_n bridge. This effect increases with the oxidation state of the sulfur atom in the linker group. Oxidation of the sulfur atom also results in stabilization of the HOMO, but this effect is smaller than the energy lowering of the LUMO. The excited states for all monomer molecules are qualitatively the same, involving a neutral state similar to that of **T3**. When the excited states are calculated for the optimized ground-state geometries of the **T3SOn** series, the lowest excited singlet state (S_1) can be described, to a first approximation, as the coupling of local excitons on each of the **T3** fragments. In symmetric dimers, the strength of this electronic interaction can be quantified by the orbital energy gap between the HOMO and HOMO− 1 (Δ HOMO), the LUMO and LUMO+1 (Δ LUMO) and the exciton splitting energy Δε. Table 2.4 reports orbital energy differences and computed exciton splitting energies for the *cis* and *trans* conformers of the **T3SO$_n$** dimers. For the *cis* conformers, the calculated values for Δε follow similar trends as the measured Δε values (Figure 2.9, section 2.4.2). In all three **T3SO$_n$** dimers, the electron - hole pair of the S_1 state fully delocalizes over the two **T3** fragments with minor contributions from the SO_n bridge, as characterized by means of a natural transition orbital (NTO) analysis (Figure 2.16, top).[124] Although the S_1 state is delocalized in all three dimers, exciton decomposition in terms of two localized (LE) and two CT diabatic states highlights the distinctive nature of the S_1 state in **T3SO$_2$** with respect to **T3S** and **T3SO**. The lowest excited state for the S and SO bridged dimers shows strong neutral character with ≤ 5% of CT participation, but in **T3SO$_2$** CT contributions account for 35% of the wave function (Table 2.5). The energy gap between the lowest neutral and CT states in **T3S** and **T3SO** is ~ 1.0 eV, while it reduces to ~ 0.5 eV for **T3SO$_2$**. This leads to neutral-CT couplings that are much larger for **T3SO$_2$**. It is

S_1	T3(a) hole / electron	linker hole / electron	T3(b) hole / electron
T3ST3	49 / 49	2 / 2	49 / 49
T3SOT3	64 / 62	2 / 3	34 / 35
$T3SO_2T3$	52 / 52	1 / 1	47 / 47
	all values in %		

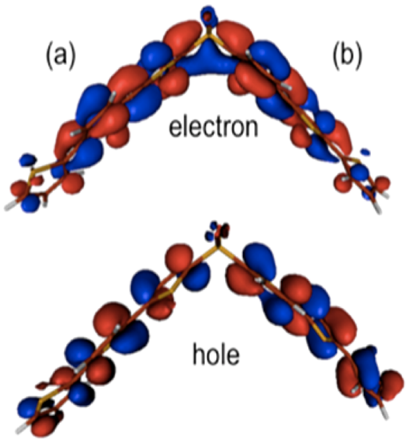

S_1*	T3(a) hole / electron	linker hole / electron	T3(b) hole / electron
T3ST3	93 / 95	5 / 3	2 / 1
T3SOT3	97 / 95	2 / 3	2 / 2
$T3SO_2T3$	93 / 89	1 / 4	6 / 7
	all values in %		

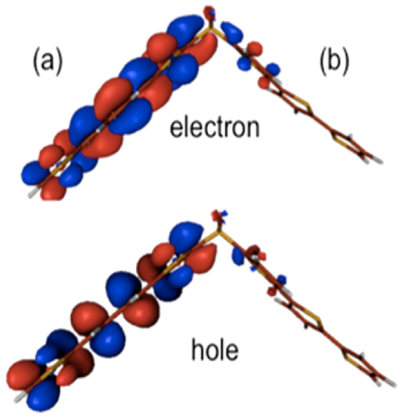

Figure 2.16. Fragment localization of the lowest singlet exciton of the **T3SO$_n$** dimers in dichloromethane and electron and hole NTOs accounting for 70% of the electronic transition in **T3SO$_2$** (top). Fragment localization of the lowest singlet exciton of the **T3SO$_n$** dimers for the S_1* optimized geometries in dichloromethane and electron and hole NTOs (bottom).The percentage of hole and electron exciton on each fragment (exciton localization) is obtained through NTO analysis.[47]

Table 2.4. Computed orbital energy gaps ΔHOMO and ΔLUMO and exciton splitting Δε (in cm^{-1}) for the **T3SO$_n$** series in dichloromethane.

		Molecule		
	Parameter	**T3S**	**T3SO**	**T3SO$_2$**
trans	ΔHOMO (cm^{-1})	1114	929	1400
	ΔLUMO (cm^{-1})	909	1374	3053
	Δε	1057	951	1430
cis	ΔHOMO (cm^{-1})	615	835	1784
	ΔLUMO (cm^{-1})	1148	1722	3518
	Δε	238	1098	1731

important that due to the symmetry of the dimers, opposite CT contributions in these species are degenerate (charge resonance, CR), resulting in no net electron transfer between **T3** moieties (Figure 2.5). This could explain the weak dependence of the absorbance peak with solvent polarity. Experimentally, absorption to S_1 does not involve a large change in the net dipole moment, but geometrical relaxation to S_1* clearly does, as evidenced by the strong solvatochromism of this state. In order to gain insight into the formation of the S_1* state, the electronic structure of each dimer was calculated after allowing them to fully relax in their first excited state. Molecular relaxation on the S_1 potential energy surface localizes the exciton onto one of the **T3** fragments for all **T3SO$_n$** molecules. Comparing the S_1 state (Figure 2.16, top) to the S_1* state (Figure 2.16, bottom) shows that relaxation induces a symmetry breaking where one of the **T3** planarizes, localizing the charge and collapsing the CR state.[125,126] The bottom panel of Figure 2.16 shows that there is now a net partial electron transfer to the other **T3**. The S_1* state thus has a net dipole and can be thought of as a true CT state. Surprisingly, the overall CT contribution at the S_1* optimized geometry of **T3SO$_2$** in dichloromethane is on the order of 25%, slightly lower in comparison to the 35% computed at the ground-state geometry. However, the most important difference is that in the ground-state geometry, the CT character is symmetrically shared between the two **T3** fragments, while in the S_1* structure 22% is localized on one **T3** fragment and 3% on the other.

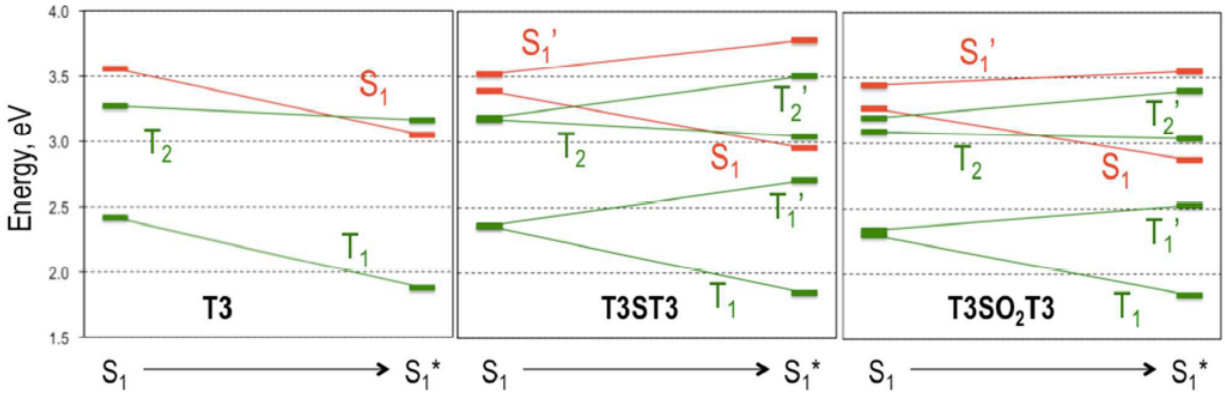

Figure 2.17. Excitation energy diagram (eV) of the lowest singlet (red) and triplet (green) states of **T3**, **T3S** and **T3SO$_2$** in dichloromethane. Horizontal axis represents the decay from S_1 to S_1* states in arbitrary units. For each graph, horizontal bars indicate vertical excitation energies at the ground (left) and lowest excited singlet (right) optimized geometries.

2.6.3 Increasing CT Decreases Intersystem Crossing

The CR/CT character of the S_1* state provides a qualitative explanation for the longer fluorescence lifetimes of the dimers. In unsubstituted **T3**, the lowest excited singlet decays rapidly to a high-lying triplet state which has been variously assigned as T_2 or T_4 .[46,127,128] This state then internally converts to the lowest triplet state (T_1) on a sub-picosecond time scale. This ISC process limits the fluorescence quantum yield of **T3** to 5% or less in solution. In the dimers, our calculations indicate that the triplet levels on separate **T3** chromophores combine to form new excitonic states. These new excitonic states are denoted T_1 and T_1' (from mixing the original T_1 states on different **T3**s), while T_2 and T_2' arise from mixing the original T_2 states on different **T3**s (Figure 2.17). The excitonic T_1 , T_1' , T_2 , and T_2' triplet states are all close in energy to the S_1/S_1* singlet states, and calculations indicate that all these states have predominantly neutral character. Due to the one electron nature of the spin−orbit operator, CT contributions to S_1/S_1* cannot couple to the neutral terms in the triplet-state wave functions. If the S_1 state in the dimer has a pure neutral character, the ISC rate should be similar to that of **T3**. Increasing the CR/ CT character of S_1/S_1* should lead to less effective singlet− triplet coupling and less efficient ISC. This reasoning has also been used to rationalize the decreased ISC rates in oligothiophenes [41,46] and helps explain the increased fluorescence as the sulfur linker is oxidized from S to SO to SO_2 . The ISC rate in the dimeric species also decreases with increasing solvent polarity from cyclohexane to dichloromethane. This behavior can again be rationalized in terms of increased CT mixing in the lowest excited state. This trend of increasing CT state mixing does not explain the shorter fluorescence lifetime in acetonitrile, however. It is likely that other factors affect the lifetime of the S_1* state in highly polar solvents, for example, the smaller S_0− S_1* and S_1*− T_1 energy gaps that could facilitate more rapid internal conversion or ISC.

The overall picture of the excited-state dynamics that emerges is summarized schematically in Figure 2.18. Photo excitation leads to an excitonic S_1 state with symmetric CR character that relaxes rapidly (<10 ps) to an asymmetric S_1* state with strong CT character. Although the excited-state structure of the dimers have been described, the question remains as to how the oxidation state of sulfur controls the amount of CT character. Below, two possible mechanisms are considered. One mechanism by which the sulfur oxidation state could affect the electronic coupling is through inducing changes in the dimer

geometry. To investigate the impact of the molecular geometry on the S_1 state, the **T3S** and **T3SO** dimers were constrained to adopt the **T3SO$_2$** optimized geometry (Table 2.5), and their lowest electronic transitions were analyzed. The results obtained for these models, both regarding the CT character of the electronic transition and the neutral-CT energy difference, are similar to the values obtained for **T3S** and **T3SO** with their own optimized geometries. That is to say, changes in the **T3SO$_2$** geometry cannot explain the enhanced CT character of the S_1 state. Moreover, the data in Table 2.5 show that when the relative arrangement of the two **T3** units is fixed, a clear correlation between the exciton splitting $\Delta\varepsilon$ and the oxidation state of the sulfur atom in the linker emerges (one that follows the experimental data closely).

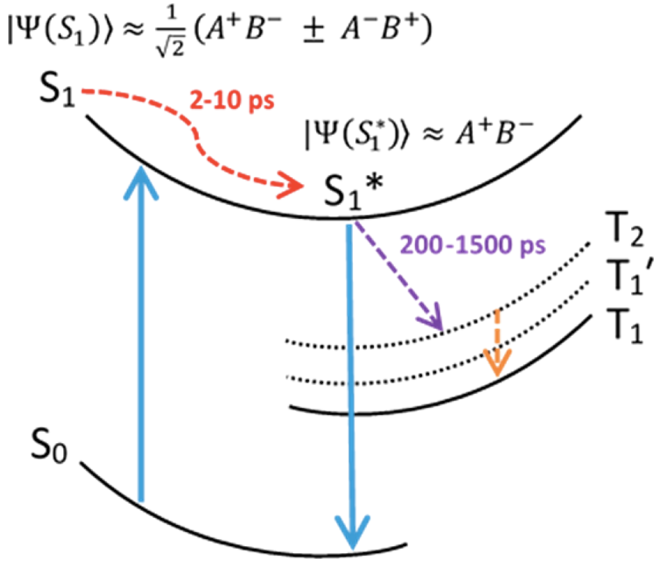

Figure 2.18. Schematic illustration of excited-state relaxation in the dimers. Note that the S_1 and S_1* states are in general superposition states with contributions from both CT and neutral states.

2.6.4 Role of Sulfur Lone Pair Electrons

A second possible mechanism for the changes in electronic coupling involves different Coulombic interactions. A major electronic structure difference between the SO_2 bridge and the S and SO linkers is the absence of sulfur lone pairs in the former. To investigate this difference in more detail, the electronic structure at the SO_n linkers in the **T3SO$_n$** dimers were evaluated by means of a natural bond order (NBO) analysis.[129] Table 2.6 summarizes the most relevant results obtained. The charge of the

bridging sulfur atom increases with oxidation state, while the oxygen charge (SO vs SO_2) remains almost constant. This behavior is a consequence of the strong polarity of the SO bonds toward the oxygen atom, as indicated by the decrease in the electronic occupation of p orbitals involved in the SO bonds ($3p_x$ and $3p_z$) and constant occupation of the p orbital oriented in the perpendicular direction ($3p_y$). In other words, the oxygen atoms pull electron density away from the sulfur atom in the bridge. These results are in line with a study of the nature of bonding in sulfoxide and sulfone systems by Chesnut and Quin.[130]

Table 2.5. Computed CT contributions (% CT), energy gap (ΔE) between the lowest neutral, and CT diabatic states and their absolute electronic coupling (Neutral-CT Coupling) for the S_1 state in the **T3SO$_n$** series at their optimized and **T3SO$_2$**-like geometries.

		Molecule		
	Parameter	**T3S**	**T3SO**	**T3SO$_2$**
Optimized Geometry	% CT	5	1	35
	ΔE (eV)	1.00	0.95	0.53
	Neutral-CT Coupling	149	41	429
T3SO$_2$ Geometry	% CT	7	8	35
	ΔE (eV)	0.98	0.79	0.53
	Neutral-CT Coupling	238	269	429

To further explore the impact of the electronic configuration of the sulfur atom in the bridge, the neutral-CT mixing and electronic couplings were computed for two additional, hypothetical **T3** dimers, **T3SH$_4$** and **T3SF$_4$**. As in the SO_2 case, the SH_4 and SF_4 linkers lack electron lone pairs on the sulfur atom (Table 2.6), but represent very different situations with respect to the polarization of the SX bonds. NBO analysis shows that the electron occupation of the 3p level of the sulfur atom in SH_4 (3.85 electrons) is of the same magnitude as that in **T3S**, while in **T3SF$_4$** the electron density is polarized toward the fluorine atoms (2.37 electrons in the 3p level). As a result, **T3SH$_4$** shows strong electronic screening, similar to that in the **T3S** dimer, while the neutral-CT mixing and coupling obtained for the SF_4 linker is similar to that of the SO_2 bridge (Figure 2.19).

Table 2.6. Atomic charges and electron occupancies of $3p_x$, $3p_y$,and $3p_z$ orbitals. Bridging sulfur atom (S) orbital localization at the SO_n, SH_4, and SF_4 bridges obtained from NBO Analysis at the CAM-B3LYP/6-31+G(d) level, in dichloromethane solvent.

		Molecule				
		T3S	**T3SO**	**$T3SO_2$**	**$T3SH_4$**	**$T3SF_4$**
Charge	Bridging S	0.351	1.383	2.269	0.655	2.322
	X[a]	—	-1.023	-0.985	-0.003/0.021	-0.518/-0.510
Orbital Occupancy	3p	3.99	3.06	2.50	3.85	2.37
	$3p_x$	1.82	1.14	0.72	1.37	0.66
	$3p_y$	0.89	0.89	0.93	1.25	0.90
	$3P_z$	1.27	1.03	0.85	1.23	0.82

[a] X = O, H, F.

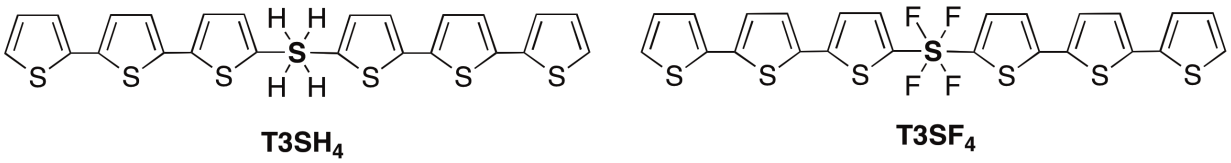

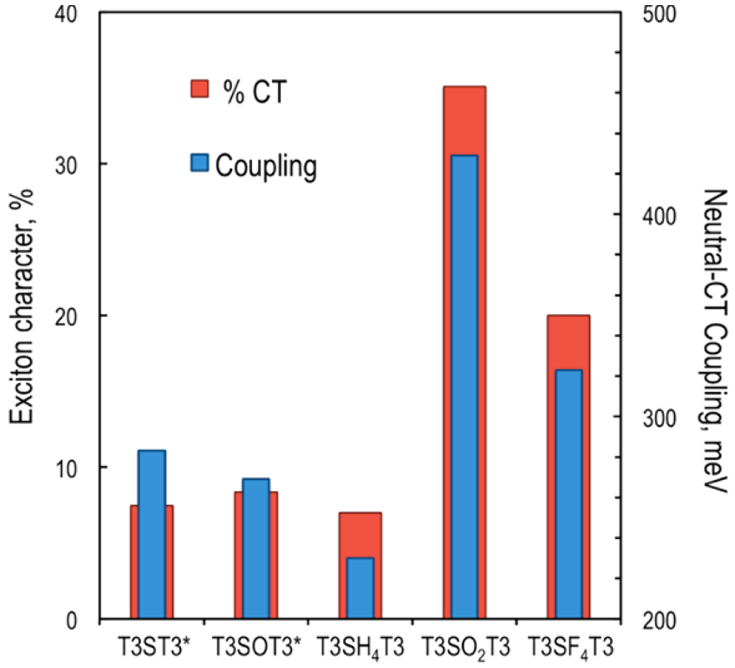

Figure 2.19. Structures of model dimers **$T3SH_4$**, and **$T3SF_4$** and exciton character as contributions (in %) of CT diabatic states to S_1 transition (red wide bars) and neutral-CT couplings (blue thin bars) for the **$T3SO_2$**, **$T3SH_4$**, and **$T3SF_4$** dimers and the **T3S*** and **T3SO*** molecular models obtained at the CAMB3LYP/ 6-31+G(d) computational level in dichloromethane.

Decreased CT coupling was also observed when the linker was changed to an O atom, which has lone pairs, while a CH_2 linker (with no lone pairs) resulted in a CT coupling comparable to the SO_2 linker. These results suggest that the electronic configuration of the sulfur atom in the SO_n bridge is the key factor that can suppress or enhance the neutral-CT mixing. In particular, it is concluded that the presence of electron lone pairs in the bridge can screen Coulombic interactions between **T3** moieties and suppress intra-dimer electronic coupling that stabilizes delocalized CR states. It is also suggested that the polarization of the SO bonds has a major role in this mechanism and that in SX_4 linkers, with formally no available electron lone pairs on the sulfur atom, polarization of the SX bonds dictates the screening strength of the electronic interactions between the **T3** moieties.

2.7 Discussion

The first important point of the work presented in this chapter is that the sulfur bridge itself has only a minor effect on the behavior of the molecule. For example, in the **T3SO$_n$** monomers, the presence of the additional sulfur functionality leads to a slight (**~** 20 nm) redshift of the absorption spectrum in the monomer series (**T3SO$_n$Me**) relative to unsubstituted **T3**, while the overall shape of the spectrum remains largely unchanged. The PL lifetime (τ_{PL}) of the **T3SO$_2$Me** monomer is nearly identical to that of unsubstituted **T3** (**~** 200 ps). The **T3SO$_n$Me** monomer series show very similar features in the transient absorption data to that of **T3**. As in **T3**, the excited state of the monomers evolves from a singlet state (S_1) with predominantly neutral character to a triplet state (T_1) through ISC. The addition of a second **T3** chromophore generates qualitative changes in the electronic structure and photophysics of the dimers. The appearance of a splitting in the dimer absorption is a clear indication that interaction between the two absorbing units has an important role in the excited-state dynamics. The solvatochromism in the steady-state fluorescence behavior of the dimers, which is absent in the monomers, indicates stabilization of a polarized CT excited-state, denoted S_1*, that is present only in the S-bridged dimers. This CT state leads to a fluorescence lifetime and quantum yield for the dimer (**T3SO$_2$**) that are significantly greater than those of **T3SO$_2$Me** or unsubstituted **T3**.

The second major finding is the dynamic nature of the S_1* state, which is formed within 10 ps, consistent with relaxation via symmetry breaking. The ability of an initially delocalized system to relax into an asymmetric charge distribution is an interesting fundamental process[131] and has been characterized in several types of multichromophoric systems,[10,11,12,49,132,133] including bianthryl.[48] Common features in the photophysics of this class of molecules include the shift of the CT emission with solvent polarity, with no shift in absorption, and the rapid relaxation from the neutral absorption state to the CT emitting state. However, there are also some notable differences between our sulfur-bridged dimers and the prototypical bichromophore, bianthryl. In bianthryl, the absorption spectrum closely resembles that of monomeric anthracene. The initial excited state of bianthryl is assumed to be localized on one of the anthracenes and is referred to as the "locally excited" (LE) state. In the **T3** dimers, the two chromophores have significant interactions even in the ground-state configuration, as evaluated from the changes in the absorption spectra. This is likely the result of the following: the larger transition dipole moment of the **T3** chromophore, the sulfur bridge orienting the transition dipole moments of the chromophores at an oblique angle, and more facile electron-transfer interactions through the bridge. Strong interchromophore interactions are in a sense built into our sulfur-bridged dimers. A second major difference is that **T3**, unlike anthracene, has a very low fluorescence quantum yield to begin with due to rapid ISC. Typically, the quantum yield of dimeric anthracenes decreases relative to the monomer due to the lower radiative rate of the dimer CT state.[134,135] In the **T3** dimers, the lower ISC rate in the CT state more than compensates for the decrease in radiative rate, and the fluorescence quantum yield increases by an order of magnitude for **T3SO$_2$** in dichloromethane.

The most obvious difference between the sulfur-bridged dimers and bianthryl is the ability to tune the amount of electronic coupling by changing the oxidation state of the bridging sulfur. The computational results indicate that the electron lone pairs present in the S and SO bridges screen the interaction between the π electrons from the two T3 chromophores. Oxidation of the sulfur atom to form the sulfone (SO_2) linker leads to polarized bonds that decrease this screening, stabilizing the CT contributions that mix with the neutral states. It might naively be expected that greater electron density on the sulfur would facilitate electronic communication between the **T3** chromophores, but our results show

that the opposite occurs. The role of solvent in screening electrostatic interactions between different regions of molecules that undergo electron transfer has been the subject of theoretical attention,[136,137] but the possibility that the polarization of the bridge valence electrons can modulate interchromophore electronic interactions has not been a significant focus.[138] Both our experimental and computational results provide evidence that the electron distribution on the bridge atom can suppress the electrostatic interactions that stabilize a luminescent CT state, suggesting that this may be an effective strategy to explore in molecular design.

The ability of the SO_2 linker to facilitate the formation of CT states may explain its utility in chromophores that show TADF, where CT interactions lead to small exchange energies and near degeneracy of the singlet and triplet states.[15,16] Oxidizing the sulfur in polythiophenes has also been shown to be an effective way to modulate the polymer bandgap,[139] most likely due to the creation of extended CT states. Our results provide an explanation for these results and, furthermore, show that formation of CT states can suppress ISC and lead to higher fluorescence quantum yields. The SO_2 linker has the added advantage of being stable against further oxidation.

While enhancement of CT interactions led to a high PL yield in our **T3** dimers, it is possible that this approach can be used in other systems to suppress CT formation. For example, if the chromophore neutral states are highly emissive (i.e., not subject to rapid ISC), then one would want to avoid CT mixing that lowers the radiative rate. To make a superradiant assembly of such chromophores,[140]one would want to use the unoxidized S linker in order to prevent CT state formation. Another application for tuning the amount of CT interaction would be to optimize singlet fission. There is general agreement that efficient singlet fission requires some CT interaction,[141,142,143,144] but too much CT character can lead to excimer formation that competes with the fission channel. Although the examples given above are somewhat speculative, they serve to illustrate how controlling interchromophore interactions in covalent assemblies could be useful for the design of functional supermolecules.

2.8 Conclusions

In this Chapter, a combination of spectroscopy and computation were used to obtain a comprehensive picture of the photodynamics of sulfur-bridged terthiophene dimers. Their novel excited-state behaviors (high fluorescence quantum yields, solvatochromism, two-step excited-state relaxation) stem from the formation of a delocalized charge resonance (CR) state (S_1) that relaxes quickly (<10 ps) to a charge transfer (CT) state (S_1*). The amount of CT in S_1 and S_1* can be modified by changing the oxidation state of the bridging sulfur group. Computational work indicates that electrostatic screening by the sulfur valence electrons is the key parameter that controls the amount of CT participation. The results presented in this Chapter provide a new strategy for tuning interchromophore interactions in covalent dimers.

2.9 Experimental

2.9.1 Steady-State UV−Vis/Photoluminescence

Electronic absorption spectroscopy was performed on a Varian Cary 5000 spectrophotometer. Corrected emission measurements were performed on a PTI QuantaMaster 50 fluorimeter at room temperature, unless otherwise specified.

2.9.2 Time-Resolved Spectroscopy

Time-resolved PL lifetime experiments were performed by frequency doubling the 750 nm output of a tunable Ti:sapphire Mai Tai laser to generate the excitation wavelength (375 nm) or using the 400 nm output of the 1 kHz laser system described below. Spectra were recorded with a Hamamatsu C4334 Streakscope which has a time resolution of 15 ps and wavelength resolution of 2.5 nm. The spectra were collected in a front face configuration utilizing magic angle polarization. TA measurements were performed using a 1 kHz Coherent Libra laser system with an Ultrafast Systems Helios TA spectrometer. The pump beam (400 nm) was generated by frequency doubling the fundamental 800 nm output. A small portion of the fundamental beam was focused onto a 3 mm sapphire plate to generate the white-light continuum probe beam. The pump and probe beams were focused onto the same spot on a 1 mm path

length, quartz flow cell. A 4 cm focal length lens was used to collect the scattered probe beam which was then coupled into an Ocean Optics S2000 spectrometer. Nonresonant contributions to the TA signal were removed by measuring each solvent response under the same experimental conditions and were subtracted from the signal using Ultrafast Systems Surface Xplorer software.[145] Pump fluences for each TA measurement were kept between 20 and 200 μJ/cm^2.

2.9.3 Computational Details

Electronic structure calculations of terthiophene (**T3**), **T3SO$_n$Me**, and **T3SO$_n$** molecules were performed using density functional theory (DFT)[146,147] with the long-range corrected version of B3LYP energy functional (CAM-B3LYP).[148] Electronic transitions were obtained with the time-dependent version of DFT (TDDFT)[149,150] and with the Tamm−Dancoff approximation.[151,152] The 6-31G(d) and 6-31+G(d) basis sets were employed for molecular geometry optimizations and the computation of excitation energies to low-lying states, respectively. The B3LYP energy functional has shown good performance in the computation of electronic excitations of sulfur-organic compounds.[153] Although it is often advisable to use tight d-functions to account for core polarization effects when dealing with second row elements such as sulfur, our chosen atomic basis functions gave similar optimized geometries and transition energies. One of the main limitations of TDDFT is its difficulty with CT-type excitations. For this reason, the long-range corrected version of the B3LYP energy functional CAM-B3LYP were used, which has shown to be capable of reliably computing CT transitions in organic molecules.[154,155,156] The effect of the solvent was taken into consideration in all calculations with the polarizable continuum model (PCM).[157] Diabatic states have been constructed with the Edmiston−Ruedenberg localization scheme[158] as linear combinations from the four lowest excited singlet eigenstates. Coupling energies between locally excited (LE) and CT diabats correspond to off diagonal terms of the four by four diabatic Hamiltonian. All calculations were done using the QChem program.[159] Natural bond orbital (NBO) analysis was performed at the CAM-B3LYP/6-31+G(d) level in dichloromethane with the NBO 5.0 package.[160]

2.9.4 General

All solvents used for photochemical measurements, dichloromethane, cyclohexane, and acetonitrile were analytical HPLC grade, and used as received from Fisher Scientific. Samples were purged with argon for no less than 15 min before emission studies. Photoluminescence quantum yields (Φ_f) for each compound were calculated according to equation 2.5, using 9-cyanoanthracene as a standard. In equation 2.5, *A* is the measured absorption at the excitation wavelength for the standard (s) and the compound of interest (x), *F* is the integrated area under the emission spectrum, η is the refractive index of the solvent and Φ_s is the known quantum yield for the standard in a given solvent [Φ_f(9-cyanoanthracene) = 0.80 in methanol, excited at 364 nm].[161] The following excitation wavelengths were used for the compounds: for all **T2SO$_n$** = 335 nm, **T3SO$_n$** = 375 nm, **NapSO$_n$** = 304 nm, and **PySO$_n$** = 362 nm. To correct for excitation intensity variation as a function of wavelength, the relative intensity of the excitation light at each wavelength was determined by integrating the excitation profile obtained with no sample present. The collected emission spectra (F_x) for the samples were then scaled relative to the excitation intensity at 364 nm where the standard was excited. To analyze the statistical significance of this method, and to ascertain the statistical significance of the observed increase in Φ_f as a function of the bridging sulfur oxidation state, data was collected for each sample at three different concentrations for all compounds including 9-cyanoanthracene. The Φ_f was calculated using equation 2.5 (below) at each concentration and the resulting data was plotted against the known concentrations.

(2.5)
$$\Phi_x = \left(\frac{A_s}{A_x}\right)\left(\frac{F_x}{F_s}\right)\left(\frac{n_x}{n_s}\right)^2 \Phi_s$$

The standard deviation in Φ_f was calculated using the measured Φ_f at different concentrations. Nuclear magnetic resonance (NMR) experiments were performed on either a 300, 400, or 600 MHz Bruker spectrometer in deuterated chloroform ($CDCl_3$) or dichloromethane (CD_2Cl_2). Compounds **T2SO$_n$** and **T3SO$_n$** were characterized by one-dimensional ^{1}H NMR only. The structures of the naphthalene and pyrene dimers (**NapSO$_n$** and **PySO$_n$**) were assigned using two-dimensional NMR experiments, including

COSY, ^{1}H-^{13}C HSQC, and HMBC. Infrared spectroscopy (IR) was performed on an attenuated total reflection (ATR) crystal using a Perkin- Elmer Frontier FT-IR spectrometer.

2.9.5 Synthetic Details

T2 & **T3**: Bithiophene & terthiophene were synthesized according to a previously published procedure.[162]

T2S: To a solution of 2,2'-bithiophene (360 mg, 2.2 mmol) in dry tetrahydrofuran (8.0 mL) at -78 ºC under nitrogen was slowly added n-butyllithium (1.6 M in hexanes, 1.4 mL, 2.2 mmol). The mixture was stirred for 1 h. To the resulting mixture was added drop-wise a solution of bis(phenylsulfonyl)sulfide (366 mg, 1.2 mmol) in dry tetrahydrofuran (5.0 mL) and the mixture was stirred overnight. The mixture was poured over water (25 mL) and extracted with diethylether (3 x 15 mL). The organic layers were combined and dried over anhydrous magnesium sulfate, filtered, and concentrated under vacuum. Purification by column chromatography (silica, hexanes) gave a yellow-white solid. Yield: 250 mg, 0.7 mmol, 65%. ^{1}H NMR (400 MHz, CD_2Cl_2): δ 7.26 (dd, 2H, J = 1.3, 5.1 Hz), 7.17-7.15 (m, 4H), 7.05 (d, 2H, J = 3.7 Hz), 7.01 (dd, 2H, J = 3.7, 5.0 Hz). HRMS (ESI): m/z calculated: 361.9386, found 361.9389.

T2SO: To a solution of **T2S** (130 mg, 0.4 mmol) in dichloromethane (6.0 mL) at 0 ºC was added meta-chloroperoxybenzoic acid (*m*-CPBA, 70%, 90 mg, 0.4 mmol) and the mixture was stirred for 15 min. The reaction mixture was poured over a saturated aqueous solution of sodium bicarbonate (15 mL) and ice, and was then extracted with dichloromethane (3 x 10 mL). The organic layers were combined, dried over anhydrous magnesium sulfate, filtered, and concentrated under vacuum. Purification by column chromatography (silica, dichloromethane) gave a white solid. Yield: 86 mg, 0.2 mmol, 64%. ^{1}H NMR (300 MHz, $CDCl_3$): δ 7.47 (d, 2H, J = 3.9 Hz), 7.31 (dd, 2H, J = 1.3, 5.1 Hz), 7.24, (dd, 2H, J = 1.4, 3.7 Hz), 7.15 (d, 2H, J = 3.9 Hz), 7.04 (dd, 2H, J = 3.7, 5.0 Hz). HRMS (ESI): m/z calculated: 378.9413, found 378.9416. IR (neat): (σ SO) 1049 cm^{-1}.

T2SO$_2$: To a solution of **T2S** (200 mg, 0.6 mmol) in dichloromethane (9.0 mL) at 0 ºC was added *m*-CPBA (70%, 270 mg, 1.1 mmol) and the mixture was stirred for 15 min. The reaction mixture was poured over a saturated aqueous solution of sodium bicarbonate (20 mL) and ice and extracted with dichloromethane (3 x 15 mL). The organic layers were combined, dried over anhydrous magnesium sulfate, filtered, and concentrated under vacuum. The crude material was purified by column chromatography (silica, 2:1 hexanes: dichloromethane) to afford a white solid. Yield: 120 mg, 0.3 mmol, 55%. ^{1}H NMR (400 MHz, CD_2Cl_2): δ 7.64 (d, 2H, *J* = 3.9 Hz), 7.34 (dd, 2H, *J* = 1.2, 5.1 Hz), 7.27-7.26 (m, 2H), 7.12 (d, 2H, *J* = 4.1 Hz), 7.06 (dd, *J* = 3.7, 5.0 Hz). HRMS (ESI): m/z calculated: 393.9284, found 393.9285. IR (neat): (ν SO_2) 1147 cm^{-1}, 1280 cm^{-1}and 1328 cm^{-1}.

T3S: Prepared in the same manner as **T2S**. Yield yellow solid: 53%. ^{1}H NMR (400 MHz, CD_2Cl_2): δ 7.26 (dd, 2H, *J* = 0.9 Hz, 5.2 Hz), 7.20 (dd, 2H, *J* = 0.9 Hz, 3.5 Hz), 7.16 (d, 2H, *J* = 3.6 Hz), 7.09 (d, 2H, *J* = 3.6 Hz), 7.07 (d, 2H, *J* = 3.9 Hz), 7.05 (d, 2H, *J* = 3.6 Hz), 7.04 (d, 2H, *J* = 3.6 Hz), 7.03 (d, 2H, *J* = 3.6 Hz). HRMS (ESI): m/z calculated: 525.9141, found 525.9144.

T3SO: Prepared in the same manner as **T2SO**. Yield yellow solid: 79%. ^{1}H NMR (400 MHz, CD_2Cl_2): δ 7.50 (d, 2H, *J* = 4.0 Hz), 7.33 (dd, 2H, *J* =1.2, 5.2 Hz), 7.27, (dd, 2H, *J* = 0.9, 3.5 Hz), 7.22 (d, 2H, *J* = 3.9 Hz), 7.21 (d, 2H, *J* = 3.9 Hz), 7.17 (d, 2H, *J* = 3.6 Hz), 7.09 (d, 1H, *J* = 3.7 Hz), 7.08 (d, 1H, *J* = 3.7 Hz). HRMS (ESI): m/z calculated: 542.9168, found 542.9167. IR (neat): (ν SO) 1047 cm^{-1}.

T3SO$_2$:Prepared in the same manner as **T2SO$_2$**. Yield yellow solid: 45%. ^{1}H NMR (400 MHz, $CDCl_3$): δ 7.64 (d, 2H, *J* = 3.9 Hz), 7.31 (dd, 2H, *J* = 0.9, 5.1 Hz), 7.25, (d, 2H, *J* = 1.4, 3.4 Hz), 7.23 (d, 2H, *J* = 3.6 Hz), 7.15 (dd, 2H, *J* = 1.2, 4.0 Hz), 7.07 (d, 1H, *J* = 3.7 Hz), 7.06 (d, 1H, *J* = 3.6 Hz). HRMS (ESI): m/z calculated: 557.9039, found 557.9047. IR (neat): (ν SO_2) 1019, 1148 cm^{-1}, 1330 cm^{-1}.

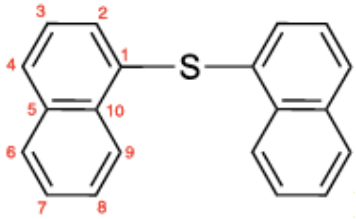

NapS: Prepared in the same manner as **T2S**, except from 1-iodonaphtalene. Recrystallized from DCM. Yield colorless crystals: 30%. ^{1}H NMR (600 MHz, CD_2Cl_2): δ 8.45 (m, 2H, H9), 7.95 (m, 2H, H6), 7.85 (m, 2H, H4), 7.58 (m, 4H, H7/H8), 7.37 (m, 4H, H7/H8). ^{13}CNMR (600 MHz, CD_2Cl_2): δ 133.69 (C5), 132.05 (C10), 131.85 (C1), 129.52 (C2), 128.13 (C6), 127.56 (C4), 126.28 (C8), 125.97 (C7), 125.37 (C3), 124.40 (C9). ^{1}HRMS (ESI): m/z calculated: 286.0816, found 286.0820.

NapSO: Prepared in the same manner as **T2SO**. Yield white solid: 56%. ^{1}H NMR (400 MHz, CD_2Cl_2): δ 8.35 (m, 2H), 8.04 (dd, 2H, J = 0.91, 7.31 Hz), 7.99, (d, 2H, J = 7.31 Hz), 7.61 (d, 1H), 7.58 (d, 1H, J = 8.22 Hz), 7.55 (m, 4H). HRMS (ESI): calculated m/z 303.0844, found 303.0846. IR (neat): (ν SO) 1041 cm^{-1}.

NapSO$_2$: Prepared in the same manner as **T2SO$_2$**. Yield white solid: 17%. ^{1}H NMR (400 MHz, CD_2Cl2): δ 8.64 (dd, 2H), 8.56 (m, 2H), 8.15, (dd, 2H, J = 8.6 Hz), 7.94 (m, 2H, J = 2.7, 6.7 Hz), 7.72 (d, 2H, J = 7.6 Hz), 7.70 (d, 2H, J = 8.3 Hz), 7.55 (m, 2H). HRMS (EI): calculated m/z 318.07145, found 318.07117. IR (neat): (ν SO_2) 1119, 1155 cm^{-1} and 1306 cm^{-1}.

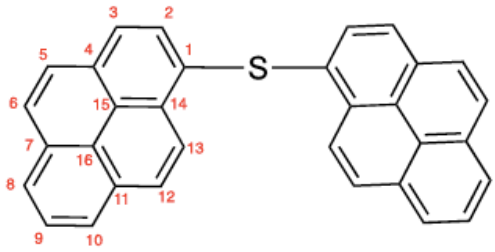

PyS: Prepared in the same manner as **T2S**, except from 1-bromopyrene. Yield yellow solid 86%. ^{1}H NMR (400 MHz, CD_2Cl_2): δ 8.77 (d, 2H, J = 9.14 Hz, H13), 8.25 (d, 4H, J = 7.61 Hz, H10), 8.17, (d, 2H, J = 9.14 Hz, H8), 8.12 (d, 1H, J = 8.83 Hz, H12), 7.08 (d, 1H, J = 7.31 Hz, H6), 8.05 (d, 2H, J = 7.31 Hz, H9), 8.04 (d, 2H, J = 8.83 Hz, H5), 8.03 (d, 2H, J = 8.22 Hz, H3), 7.85 (d, 2H, J = 8.22 Hz, H2). ^{13}C NMR (600 MHz, CD_2Cl_2): δ 131.91 (C7), 131.57 (C11), 131.38 (C4), 131.30 (C14), 130.90 (C1), 130.58 (C2), 128.92 (C12), 128.25 (C6), 127.79 (C5), 126.95 (C9), 126.13 (C8), 126.08 (C10),

125.89 (C15), 125.80 (C3), 124.97 (C16), 124.75 (C12). HRMS (ESI): calculated m/z 434.1129, found 434.1128.

PySO: Prepared in the same manner as **T2SO**. Yield yellow solid: 30%. ^{1}H NMR (400 MHz, CD_2Cl_2): δ 8.75 (d, 2H, *J* = 9.22 Hz, H13), 8.56 (d, 2H, *J* = 8.19 Hz, H2), 8.29, (d, 2H, *J* = 8.19 Hz, H3), 8.27 (d, 2H, *J* = 8.88 Hz, H8), 8.25 (d, 2H, *J* = 8.19 Hz, H10), 8.20 (d, 2H, *J* = 9.56 Hz, H12), 8.17 (d, 2H, *J* = 9.22 Hz, H6), 8.09 (d, 2H, *J* = 8.88 Hz, H5), 8.07 (1H, *J* = 7.51, H9), 8.05 (1H, *J* =7.85, H9). ^{13}C NMR (400 MHz, CD_2Cl_2): δ 137.76 (C1), 133.43 (C4), 131.23 (C7), 130.52 (C11), 129.64 (C12), 129.41 (C6), 128.67 (C14), 127.28 (C5), 126.77 (C9), 126.49 (C10), 125.60 (C3), 124.65 (C15), 124.34 (C16), 123.46 (C2), 121.50 (C13) HRMS (EI): calculated m/z 450.10784, found 450.10760. IR (neat): (ν SO) 1046 cm^{-1}

PySO$_2$: Prepared in the same manner as **T2SO$_2$**. Yield yellow solid: 24%. ^{1}H NMR (400 MHz, CD_2Cl_2): δ 9.16 (d, 2H, *J* = 8.22 Hz), 8.95 (d, 2H, *J* = 9.44 Hz), 8.43, (d, 2H, *J* = 8.53 Hz), 8.30 (d, 2H, *J* = 7.61 Hz), 8.25 (d, 4H, *J* = 8.83 Hz), 8.17 (dd, 4H, *J* = 2.13, 9.14 Hz) 8.08 (d, 1H, *J* = 7.61 Hz), 8.06 (d, 1H, *J* = 7.61 Hz). HRMS (ESI): m/z calculated: 467.1106, found 467.1104. IR (neat): (ν SO_2) 1122, 1153 cm^{-1}, and 1296 cm^{-1}.

T3SMe: To a solution of terthiophene (500 mg, 2 mmol) in dry THF (20 mL) was added n-butyllithium (1.25 mL, 2 mmol, 1.6 M in hexanes) drop-wise at -78 ºC under a nitrogen atmosphere. The reaction was allowed to proceed 1.5 h at -78 ºC after which time dimethyl disulfide (400 µL, 396 mg, 4 mmol) was added in two portions. The orange solution was brought to room temperature after addition of the electrophile and allowed to stir for an additional hour. The reaction was then quenched with water and extracted with dichloromethane (3 × 50 mL). The organic extracts were combined and the solvent was removed under vacuum. The crude, dark yellow solid was purified using flash column chromatography (silica, hexanes) to yield 300 mg of pure product, 1.2 mmol, 60%. ^{1}H NMR (400 MHz, CD_2Cl_2) δ 7.26 (dd, ^{1}H, *J* = 5.2, 1.2 Hz), 7.20 (dd, 1H, *J* = 3.7, 1.2 Hz), 7.10 (d, 1H, *J* = 3.7), 7.26 (dd, 1H, *J* = 5.2, 1.2

Hz), 7.05 (m, 3H), 6.99 (d, 1H, J = 3.7 Hz), 2.52 (s, 3H). HRMS m/z calculated 293.9665, found 293.9666.

T3SOMe: To a solution of **T3SMe** (100 mg, 0.3 mmol) in dichloromethane (5 mL) was added *m*-CPBA (84 mg, 0.5 mmol) at room temperature with stirring. After ~5 min a yellow solid precipitated out of solution and starting material was no longer present by thin layer chromatography. The rest of the solid was precipitated out of solution by adding ~20 mL hexanes. The solid was filtered off and purified by column chromatography with (silica, 1:1 hexanes/dichloromethane). The pure product was obtained as a yellow solid, 33 mg, 0.1 mmol, 32%. ^{1}H NMR (400 MHz, CD_2Cl_2) δ 7.36 (d, 1H, J = 3.9 Hz), 7.29 (dd, 1H, J = 4.9, 0.9 Hz), 7.24 (dd, 1H, J = 3.7, 0.9), 7.20 (d, 1H, J = 3.9 Hz), 7.16 (d, 1H, J = 3.7 Hz), 7.14 (d, 1H, J = 3.7 Hz), 7.06 (d, 1H, J = 3.7 Hz), 7.05 (d, 1H, J = 3.7 Hz), 2.91 s (3H). HRMS m/z calculated 309.9614, found 309.9614. IR (neat) (ν SO) 1040 cm^{-1}.

T3SO$_2$Me: To a solution of **T3SMe** (100 mg, 0.3 mmol) in dichloromethane (5 mL) was added *m*-CPBA (171 mg, 1 mmol) at room temperature with stirring. After ~5 min a yellow solid precipitated out of solution and starting material was no longer present by thin layer chromatography. The rest of the solid was precipitated out of solution by adding ~20 mL hexanes. The solid was filtered off and purified by column chromatography (silica, 1:1 hexanes/dichloromethane). The pure product was obtained as a yellow solid, 45 mg, 0.13 mmol, 42%. ^{1}H NMR (400 MHz, CD_2Cl_2) δ 7.60 d (^{1}H, J = 3.9 Hz), 7.31 dd (1H, J = 5.1, 1.2 Hz), 7.25 m (2H), 7.19 d (1H, J = 3.9 Hz), 7.16 d (1H, J = 3.7 Hz), 7.06 dd (1H, J = 4.8, 3.6 Hz), 3.19 s (3H). HRMS m/z calculated 325.9563, found 325.9561. IR (neat) (ν SO$_2$) 1140, 1301 and 1310 cm^{-1}.

CHAPTER 3*

The Photochemistry of Sulfur-Bridged Anthracene Dimers

3.1 Introduction

With the intention of expanding the scope of sulfur-bridged aromatics that exhibit enhanced electronic coupling, anthracene was bridged symmetrically about sulfur to yield 9,9'-bis(anthracene)sulfide (**AnS**, Scheme 3.1). Much like the naphthalene and pyrene monomers from Chapter 2, anthracene absorbs light in the near UV (~300 - 400 nm) which is characterized as a π - π* transition. Additionally, the transition dipole for this π - π* transition is polarized along the short molecular axis.

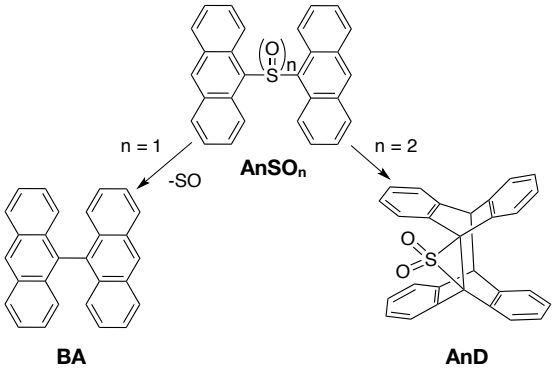

Figure 3.1. Structures of S-bridged anthracene dimers (**AnSO$_n$**) and the oxidation-state dependent photoproducts **BA** and **AnD**.

As such, it was expected that similarly enhanced fluorescence quantum yields would be observed as the oxidation state of the bridging sulfur between anthracene is increased from S (**AnS**), to SO (**AnSO**), to SO_2 (**AnSO$_2$**). Surprisingly, it was instead found that sulfur-bridged anthracene exhibits photo-reactivity that is dependent on the oxidation-state of the bridging sulfur (Figure 3.1, Scheme 3.1). The sulfide (**AnS**) exhibits relatively weak photoluminescence and dilute solutions are stable to irradiation at 365 nm. Irradiation of **AnSO** under the same conditions results in rapid loss of the bridging SO and formation of a new carbon-carbon bond yielding 9,9'-bianthryl (**BA**) in >99% isolated yields. Interestingly, irradiation of **AnSO$_2$** using the same light source yields a bridged anthracene dimer (**AnD**) containing a three-membered "episulfone" ring. In the dark, the bridged compound **AnD** reverts thermally back to **AnSO$_2$**. No formation of **BA** has been observed from **AnSO$_2$** or the dimer **AnD**.

* The crystallographic data presented section 3.3.1 were collected and analyzed by Brian Patrick and Élise Caron (UBC). The content of this chapter has been published previously:

Christensen, P. R.; Patrick, B. O.; Caron, E.; Wolf, M. O. *Angew. Chem. Int. Ed.* **2013**, *125*, 13184

3.2 Synthesis

Scheme 3.1. Synthesis and photochemical reactivity of sulfur-bridged anthracenes.

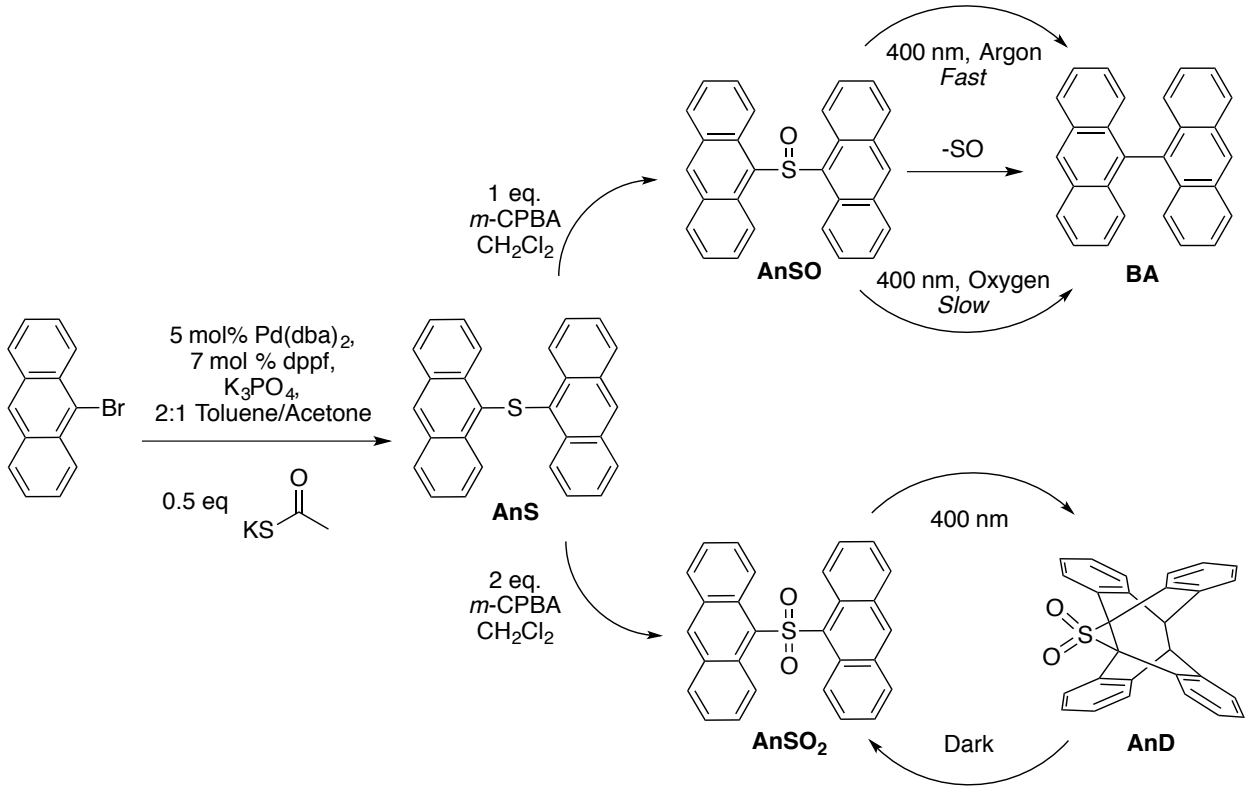

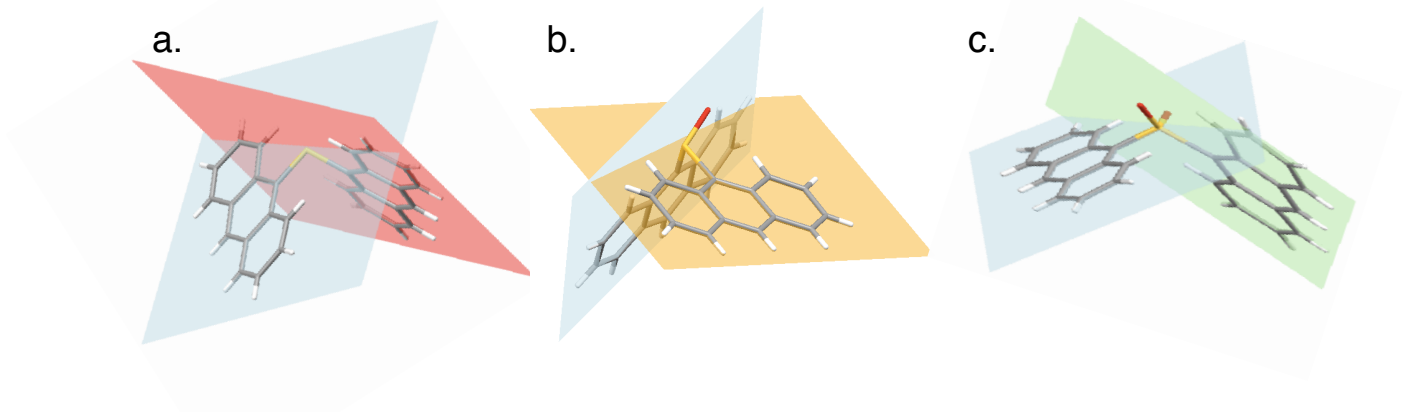

Figure 3.2. Solid-state structures of **AnS** (a), **AnSO** (b), and **AnSO₂** (c) determined by single crystal XRD. The two anthracene planes are highlighted using different colors.

The sulfide (**AnS**) was synthesized using palladium-catalyzed cross-coupling[163] of 9-bromoanthracene and potassium thioacetate (Scheme 3.1). Attempts to use Cu[164,165] or Pd[166] catalysts to couple 9-anthracenethiol and 9-bromoanthracene were unsuccessful, possibly because of catalyst poisoning with the electron-rich thiol. The corresponding sulfoxide (**AnSO**) and sulfone (**AnSO$_2$**) were obtained by oxidation of **AnS** with one, or two equivalents, respectively, of meta-chloroperoxybenzoic acid (*m*-CPBA).

3.3 Structural Characterization

3.3.1 X-Ray Crystallography.

Single crystals of compounds **AnS**, **AnSO**, and **AnSO$_2$**, and **AnD** were obtained by slow evaporation of saturated dichloromethane solutions and the structures were determined using X-ray diffraction (Figures 3.2 & 3.3).[167] Crystallographic data for 9,9'-bianthryl (**BA**) have been previously reported.[168] The molecular structures of all **AnSO$_n$** are qualitatively similar, with only minor differences observed in the solid-state geometries. The intramolecular anthracene–anthracene centroid (An–An) distance remains relatively constant throughout the series (**AnS** = 5.10 Å , **AnSO** = 4.98 Å, **AnSO$_2$** = 5.02 Å), and the through space distance between the bridge-head (C-S-C) carbons are all ~ 2.9 Å. One noteworthy point is that the closest intermolecular An-An contacts decrease as the oxidation state of the bridging sulfur increases (**AnS** = 5.75 Å, **AnSO** = 4.48 Å, **AnSO$_2$** = 3.94 Å). This trend in intramolecular

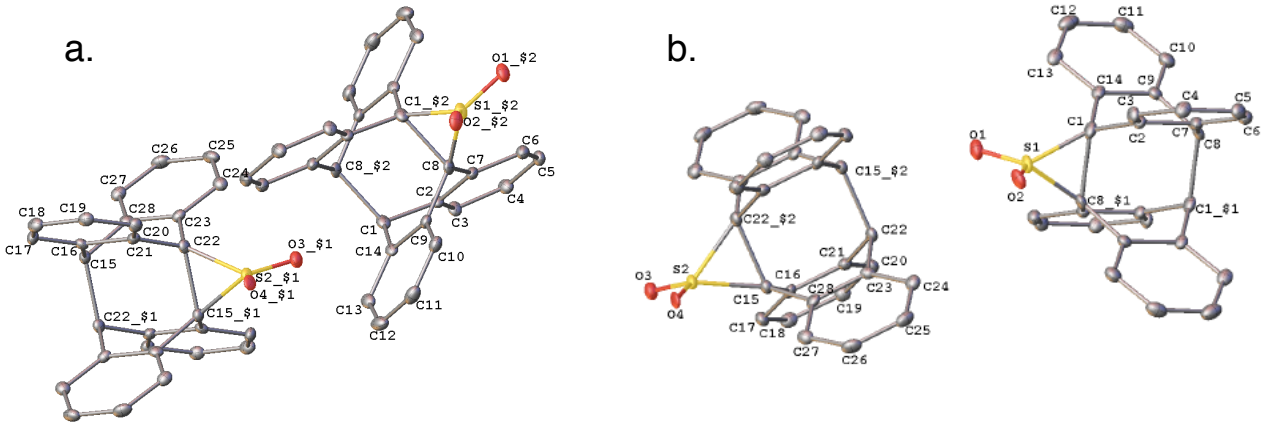

Figure 3.3. Solid-state structure of **AnD** showing the two observed packing orientations (a) and (b) (twinned crystal).

packing is consistent with that of anthracene derivatives having electron-withdrawing groups (*e.g.* perfluoroanthracenes) that are known to exhibit contracted intermolecular packing compared to unsubstituted anthracene.[169,170] Compared to the S-bridged anthracenes, the solid-state structure of **BA** is unique in that the anthracene units are nearly orthogonal (~88º) to one another.

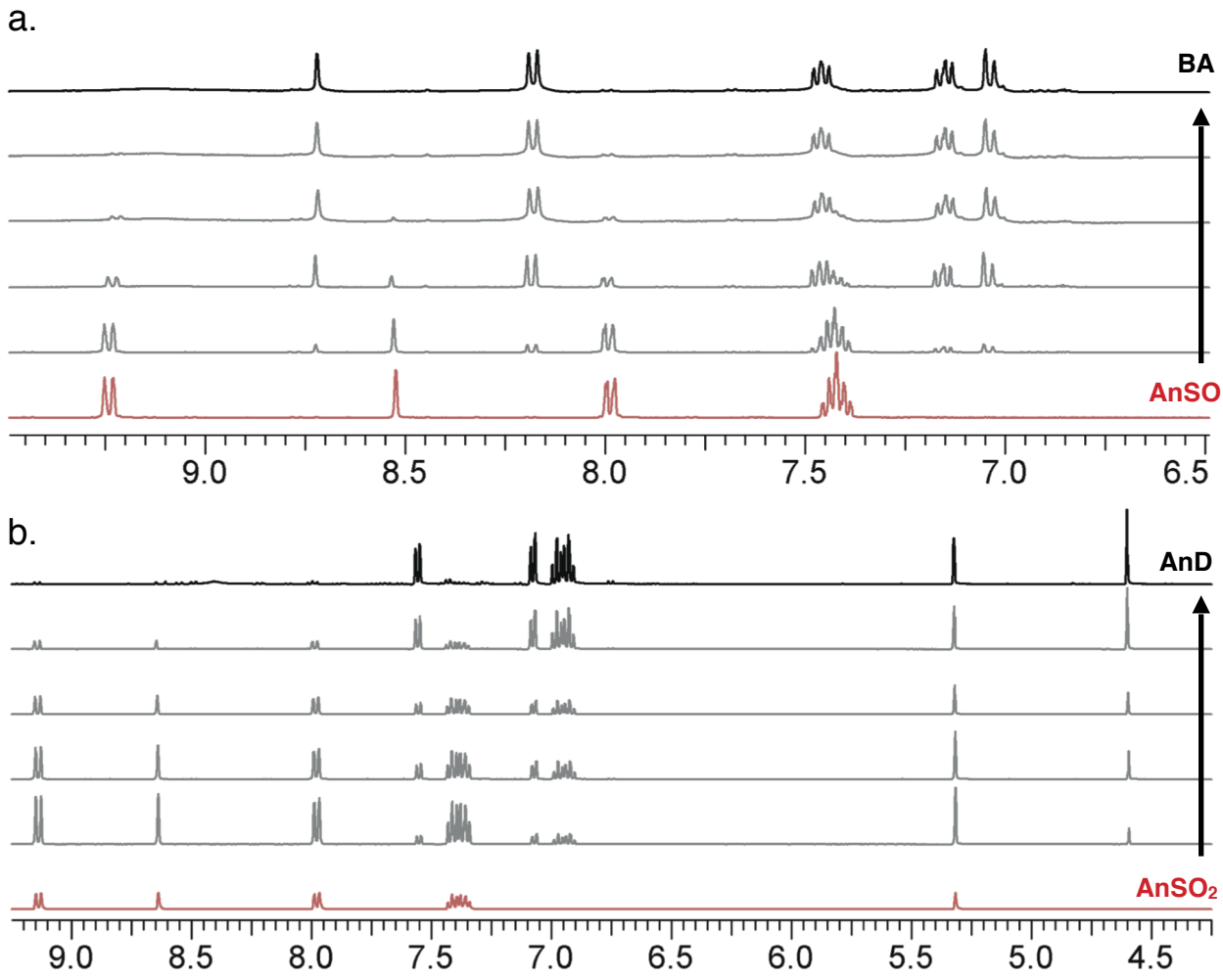

Figure 3.4. ^{1}H NMR spectra showing the conversion of (a) **AnSO** (—) to **BA** (—), and (b) the conversion of **AnSO$_2$** (—) to the bridged dimer (—).

The SO_2-bridged dimer (**AnD**) crystallized with two statistically relevant components (twinned), and the structure of each component was solved (see 3.9.2 for details). The structures of the bridged dimer contain a three-membered episulfone ring with bond angles of 60.8º at each vertex (Figure 3.3). Bridged anthracene dimers are well-known; the [4+4] cycloaddition of anthracene is one of the oldest documented

photoreactions, first observed in 1867 by Fritzsche,[171] and has since been reviewed several times.[172,173,174] Strained carbon-sulfur bonds have been synthetic targets for several decades as precursors for introducing unsaturated bonds into organic compounds.[175,176,177] Additionally, tethered anthracenes, for instance 9,9' methylene bridged anthracenes are known to undergo similar photodimerization through the 9 and 10 positions of each anthracene (see Discussion, Scheme 3.6).

3.3.2 Nuclear Magnetic Resonance (NMR).

^{1}H NMR spectroscopy was employed to monitor the conversion of **AnSO** to **BA**, and of **AnSO$_2$** to the bridged species **AnSO$_2$** (Figure 3.4). Notably, the singlet at δ = 8.68 ppm in the spectrum of **AnSO$_2$**, which corresponds to the aromatic proton directly opposite to the sulfur bridge, is shifted upfield at δ = 4.64 ppm for **AnD**, typical of anthracene photodimers.[11] Under the same irradiation conditions no change was observed in the ^{1}H NMR spectrum of **AnS**. From these ^{1}H NMR experiments it is clear to see that the conversion of both **AnSO** to **BA** and from **AnSO$_2$** to **AnD** occurs without the formation of noticeable byproduct or degradation.

3.4 Photophysical Characterization

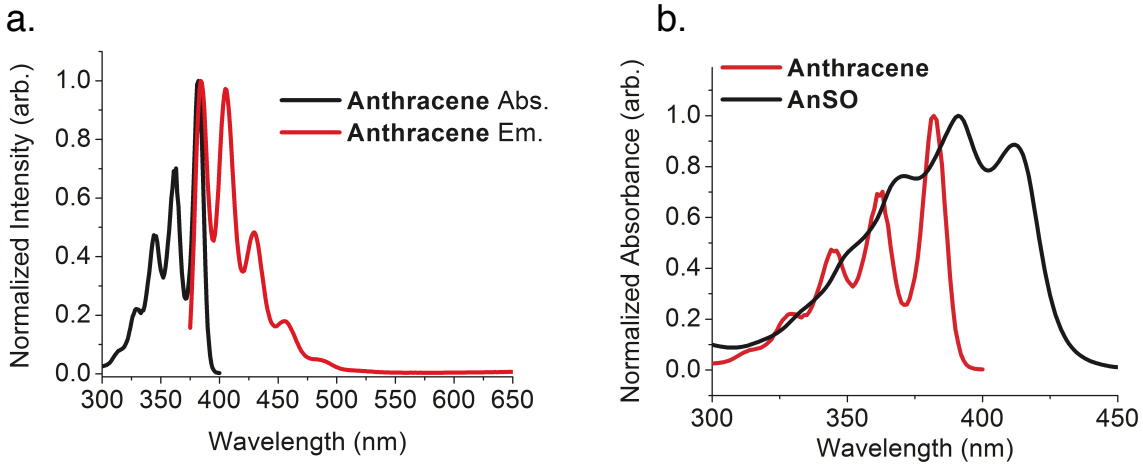

Figure 3.5. Absorbance and photoluminescence spectra for unsubstituted anthracene (a) and absorption spectra of **AnSO** compared to unsubstituted anthracene (b).

In order to better understand how and why the change in oxidation state of the bridging sulfur results in significantly different reaction pathways, the steady state photo physical properties were studied. By exploring the differences in light absorption and emission as a function of oxidation state, it is possible to learn more about the excited state from which this variable reactivity occurs. Compared to unsubstituted anthracene, all **AnSO$_n$** exhibit broadened and red-shifted absorption profiles (Figures 3.5 and 3.6).

3.4.1 UV-Vis Spectroscopy

The UV-Vis absorption band of unsubstituted anthracene exhibits sharp and structured features between 300 - 400 nm. Although broader, and slightly red-shifted, the UV-Vis absorption spectra of all members of the **AnSO$_n$** series show the structured "fingerprint" profiles common of anthracene (Figure 3.6d-f). For all **AnSO$_n$**, the broadening can be attributed to interaction between the transition dipoles of

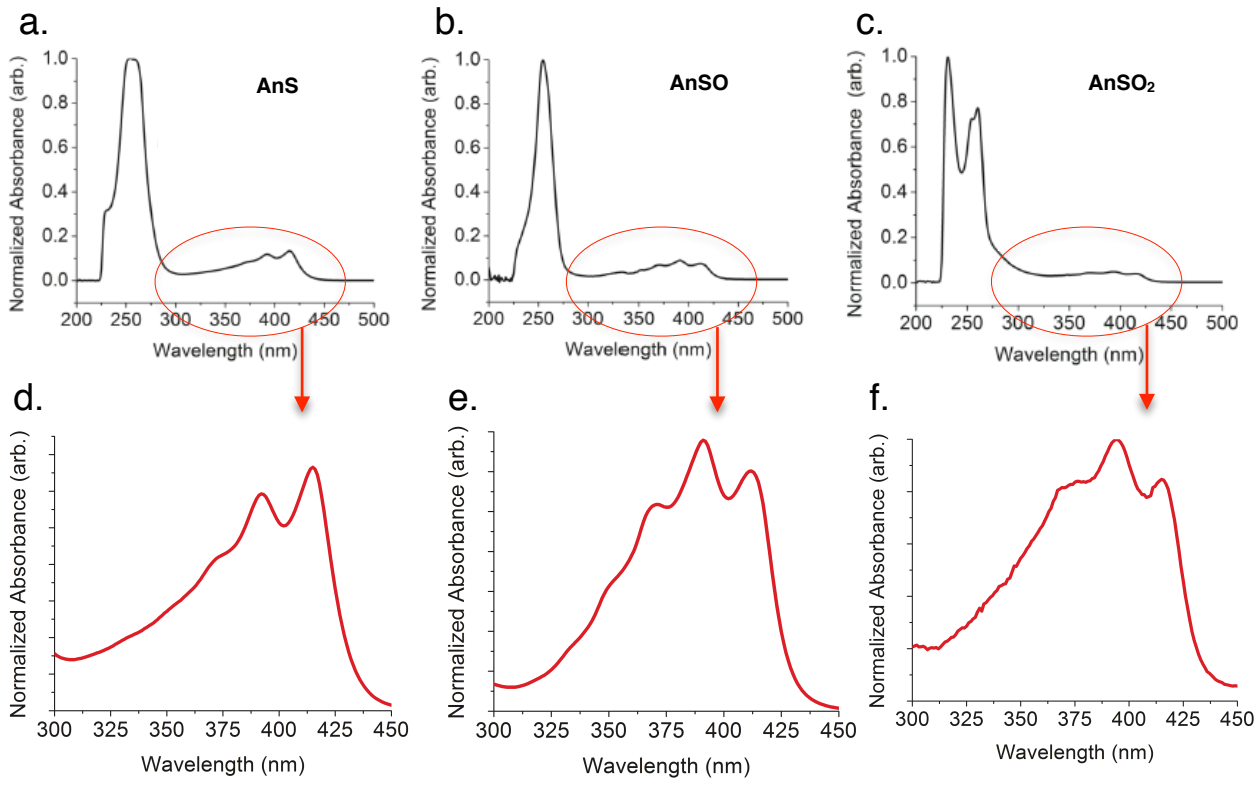

Figure 3.6. UV-Vis spectra for (a) **AnS**, (b) **AnSO** and (c) **AnSO$_2$**. The π-π* region of the UV-Vis spectrum (300 - 450 nm) are shown directly below each spectrum, (d) **AnS**, (e) **AnSO** and (e) **AnSO$_2$**.

the bridged anthracenes. Upon formation of **BA** from **AnSO**, the absorption spectrum exhibits loss of the band centered at 410 nm and an increase in the vibrational structure between 300 - 400 nm (Figure 3.7a). Much like the terthiophene dimers presented in Chapter 2 the transition dipole for the low energy π-π* transition (300 - 400 nm) in anthracene is polarized in the direction of the sulfur-bridge (short molecular axis).

The formation of **AnD** from **$AnSO_2$** results in a decrease in the structured absorbance between 325 - 425 nm (Figure 3.7b). This increased sharpness upon formation of **BA** is attributed to a decrease in interaction between anthracene as the geometry changes from bent (**AnSO**, ~110º) to orthogonal (minimal π - π overlap). The decrease in oscillator strength between 325 - 450 nm for **AnD** is attributed to the loss of conjugation in each of the anthracene units.

3.4.2 Photoluminescence Spectroscopy

Photoirrradiation of **AnSO** results in a significant (10 fold) increase in PL intensity due to the formation of BA (Figure 3.7c). For **$AnSO_2$**, a decrease in PL intensity is observed as **AnD** is formed. The photoluminescence (PL) spectra of all **$AnSO_n$** are broad, less structured, and red-shifted relative to unsubstituted anthracene (Figure 3.7d). The origin of this broad, unstructured photoluminescence likely results from charge transfer (CT), or intramolecular excimer formation. In addition to being structurally analogous to all of the molecules in Chapter 2 where CT is central to the photophysics, intramolecular CT is also well known to occur in **BA**.[178,179] Additionally, in high enough concentrations, anthracene is known to form interfacial (π - π) aggregates which exhibit absorption and emission properties that are broader and red-shifted relative to the fully solvated molecular ensemble. These interfacial aggregates, which can be as small as two molecules in size, are known as excimers (same molecules) or exciplexes (different molecules). Often, to differentiate between CT and excimer/exciplex type excited states, the photoluminescence is measured in solvents of increasing polarity. The difference between excimer and CT emission, is that CT states, which are polar in nature are increasingly stabilized as the polarity of the surrounding medium is increased, while excimers are non-polar, and thus exhibit little or no solvent

dependence. Accordingly, the PL spectra for all **AnSO$_n$** molecules were studied in solvents of increasing polarity to probe the presence of CT (Figure 3.8).

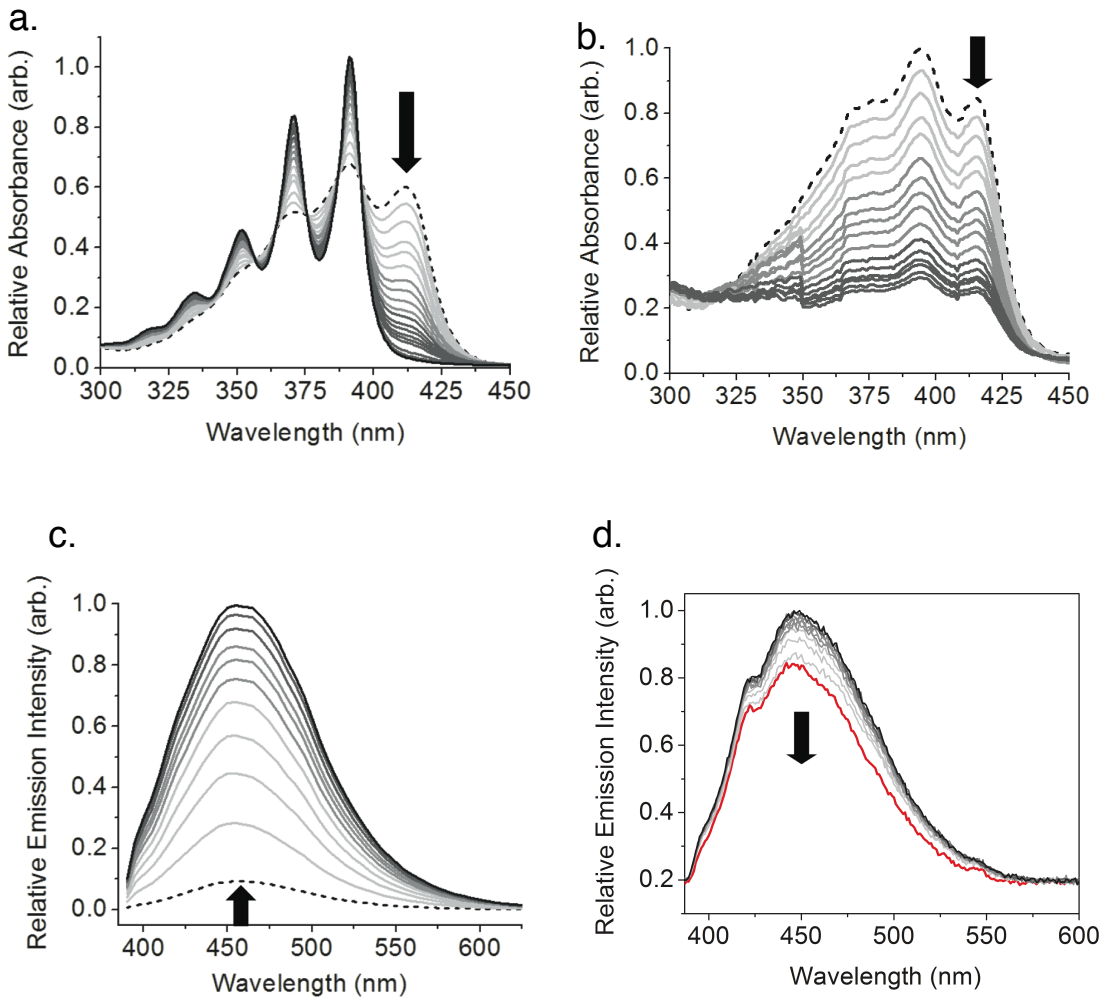

Figure 3.7. Change in UV-Vis spectra between 300 - 450 nm during the photochemical conversion of **AnSO** (- - -) to **BA** (——) (a) and **AnSO$_2$** (- - -) to the bridged **dimer** (——) (b). Upon formation of **BA**, a significant increase in photoluminescence is observed (c) while very little change is observed in the PL spectrum of **AnSO$_2$** (——) as the **dimer** (——) is formed (d).

A pronounced redshift in the PL spectrum of **AnSO** is observed as the solvent is changed from cyclohexane (CHx) to acetonitrile (ACN) indicating that emission from this SO-bridged anthracene is likely occurring from a CT state. It is also worth noting here that the emission that is observed in dilute solutions of **AnSO** could actually arise from trace amounts of the photoproduct **BA**. The PL spectra of

AnS exhibit complex, solvent-dependent profiles. In non-polar solvent (cyclohexane) a combination of structured PL between 390 - 450 nm is present along with broad, unstructured emission at wavelengths >450 nm (Figure 3.8a). Moreover, the broad, long-wavelength PL is most prominent in non-polar solvents.

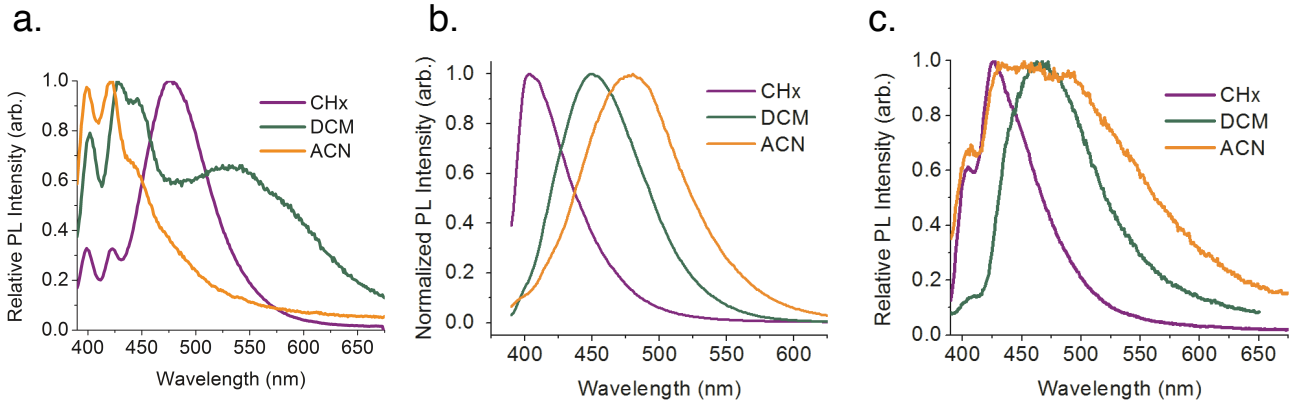

Figure 3.8. Normalized photoluminescence (PL) spectra for **AnS** (a), **AnSO** (b), and **AnSO$_2$** in cyclohexane (CHx), dichloromethane (DCM) and acetonitrile (ACN).

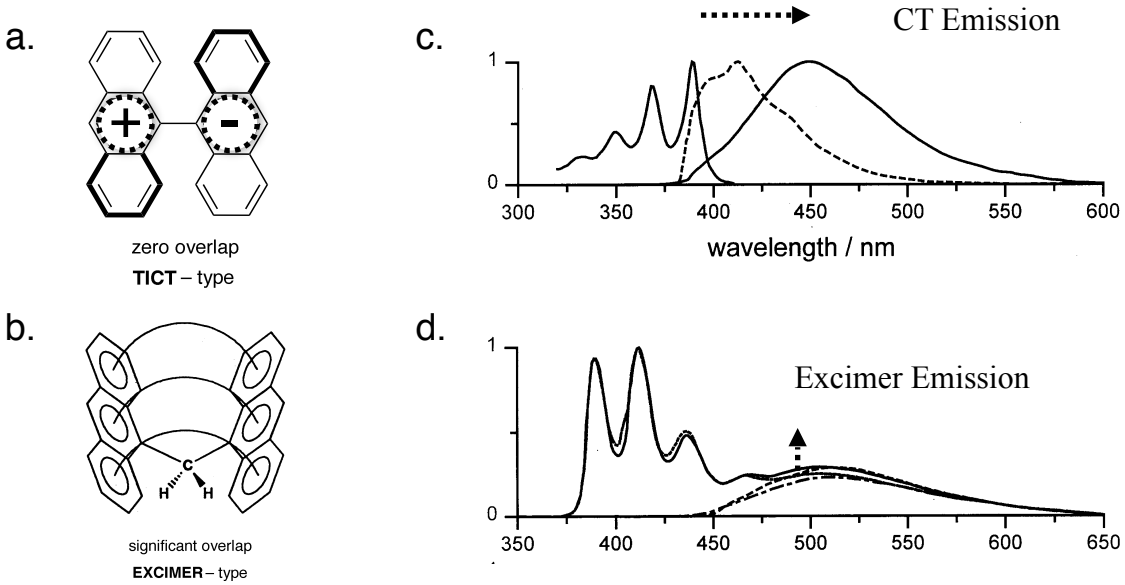

Figure 3.9. Illustration showing the difference between bridged anthracenes that are known to undergo charge transfer (a) and excimer type photoluminescence (c and d, respectively).

Previous studies have shown that anthracenes tethered together with alkyl linkers can exhibit broad emission resulting from a combination of excimer (Ex), and charge-transfer (CT) excited states, whereas structured, shorter-wavelength emission results from delocalized intra-anthracene excited states (Figure 3.9).[180] Accordingly, the structured photoluminescence observed in **AnS** (in all solvents) is attributed to localized-anthracene photoluminescence, similar to that of unsubstituted anthracene. The broad and red-shifted PL in **AnS**, which is most prominent in non-polar solvent, is attributed to excimer-like emission.

The significant increase in the excimer PL for **AnS** in cyclohexane could result from aggregation between **AnS** molecules due to limited solubility. Excimer formation for **AnS** is further supported by the presence of only structured PL in the most polar solvent (acetonitrile), which if the PL were due to a polar CT state, would be red-shifted. Furthermore, the major difference between PL for **AnS** compared to the reactive species (**AnSO**, **AnSO$_2$**) is that the structured (anthracene -localized) emission dominates.

The solvatochromic behavior of **AnSO$_2$** is different than in either **AnS** and **AnSO**. As the solvent polarity is increased from non-polar cyclohexane to moderately polar dichloromethane a significant red-shift is observed, indicating stabilization of a polar emitting state. However, in highly polar solvent (acetonitrile) a broad, superposition of the PL in cyclohexane and dichloromethane is observed. The presence of both short and long wavelength components in **AnSO$_2$** in polar solvents suggests that a combination of excimer and CT interactions is occurring between anthracenes.

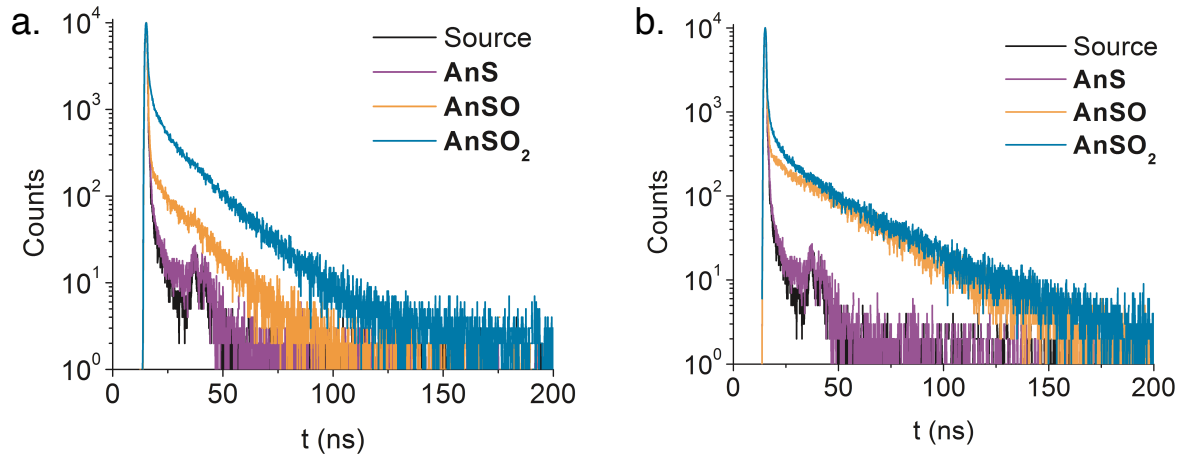

Figure 3.10. Photoluminescence lifetime data for all **AnSO$_n$** in air (a) and sparged with argon (b).

3.4.3 Photoluminescence Lifetimes

The photoluminescence lifetimes (τ_{PL}) of all **AnSO$_n$** species were found to be dependent on the oxidation state of the bridging sulfur. All of the compounds exhibit short (≤ 1 ns) τ_{PL} while **AnSO** and **AnSO$_2$** exhibit multi-exponential lifetimes with a substantially longer (~30 ns) component (Figure 3.10, Tables 3.1 and 3.2). Previous studies[18] have correlated longer-lived bi-exponential τ_{PL} in tethered anthracenes to the rate of deactivation of "excimer" states where longer τ_{PL} indicates longer-lived excimer states. The longer τ_{PL} of **AnSO** and **AnSO$_2$** suggests that long-lived excited-state species may be responsible for the observed reactivity. While the excited state of **AnS** is deactivated rapidly through either non-radiative intersystem crossing or through prompt photoluminescence, **AnSO** and **AnSO$_2$** have sufficient time to undergo larger structural rearrangements in the excited state.

Table 3.1. Photoluminescence lifetimes for all **AnSO$_n$** taken under ambient conditions (air).

	Molecule		
AIR	**AnS**	**AnSO**	**AnSO$_2$**
τ_1	≤ 1 ns (100%)	≤ 1 ns (93%)*	≤ 1 ns (57%)
τ_2	—	15 ns (7%)	16 ns (31%)
τ_3	—	—	2.5 ns (12%)

*For the fits that yield multiple components, the percent contribution to the lifetime is also shown (X%).

Table 3.2. Photoluminescence lifetimes for all **AnSO$_n$** taken under argon.

	Molecule		
ARGON	**AnS**	**AnSO**	**AnSO$_2$**
τ_1	≤ 1 ns (100%)	≤ 1 ns (63%)	≤ 1 ns (71%)
τ_2	—	15 ns (37%)	16 ns (22%)
τ_3	—	—	2.5 ns (7%)

3.5 Kinetics

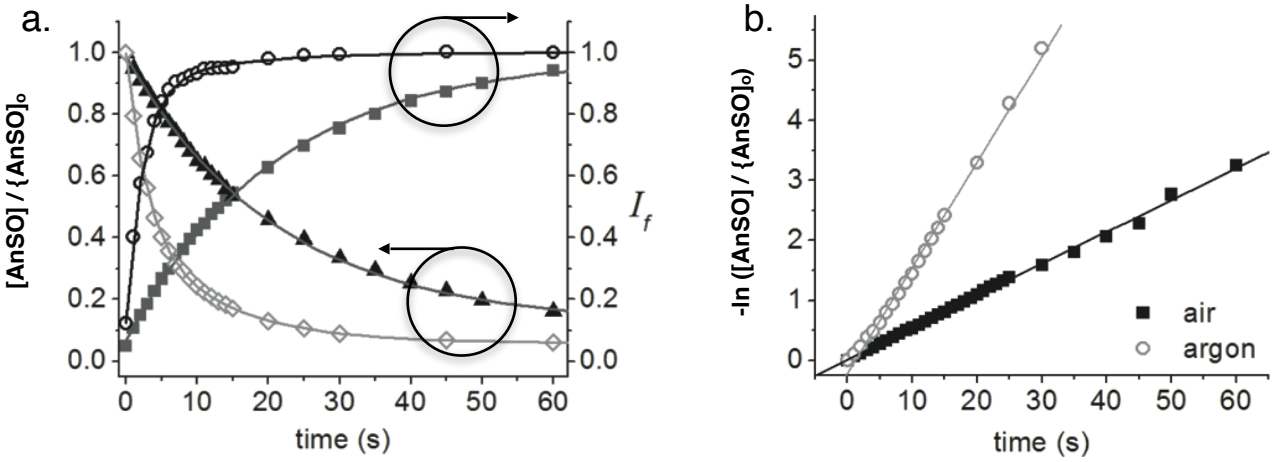

Figure 3.11. Kinetic data showing the loss of **AnSO** and the concomitant increase in PL intensity (I_f) in the presence (solid shapes), or absence of oxygen (open shapes). (b) The corresponding kinetic fits for the formation of **BA** from **AnSO** in the presence and absence of oxygen.

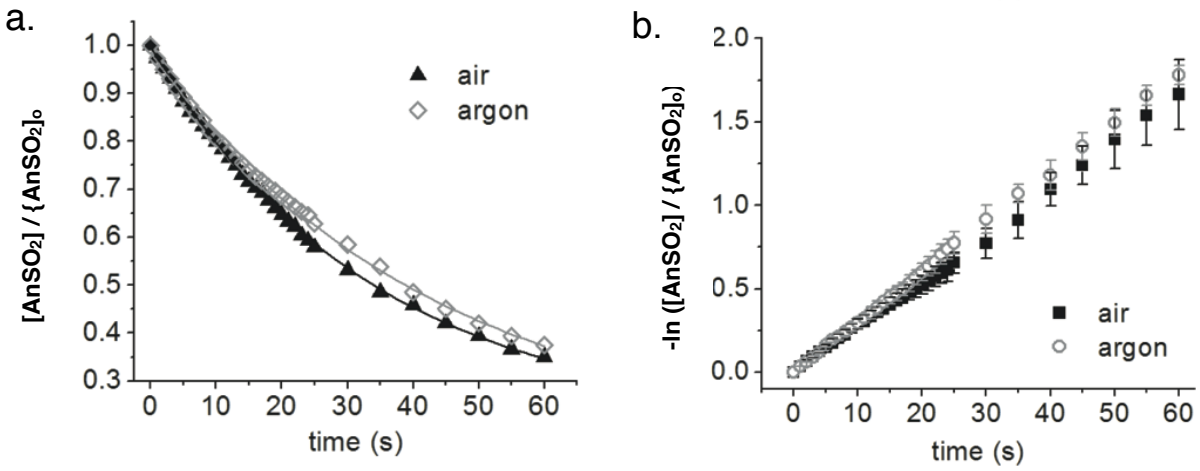

Figure 3.12. Kinetic data showing the loss of **AnSO$_2$** in the presence (solid shapes), or absence of oxygen (open shapes). (b) The corresponding kinetic fits for the formation of **AnD** from **AnSO$_2$** in the presence and absence of oxygen.

Kinetic data for the conversion of **AnSO** to **BA** were collected by measuring the loss in absorbance at 410 nm and the increase in PL at 455 nm (Figure 3.11). Likewise, kinetic data for the formation of the bridged dimer **AnD** were collected by measuring the change in **AnSO$_2$** absorbance at 415 nm (Figures 3.12). The loss in absorbance (as a function of time) for both **AnSO** and **AnSO$_2$** was fit to a single exponential trace and rate constants were extracted. Interestingly, the formation of **BA** from

AnSO was found to be dependent on the presence of oxygen. After sparging solutions of **AnSO** with argon prior to photoirradiation, the formation of **BA** occurs five times faster (Table 3.3). Conversely, the formation of **AnD** from **$AnSO_2$** shows no dependence on the presence of oxygen.

3.6 Triplet Sensitization

While it is clear, based on the significant difference in photoreactivity, that the excited-state of all **$AnSO_n$** is greatly affected by the oxidation state of the bridging sulfur, the question of *why* this is the case has yet to be explored. The absorption, photoluminescence, and kinetic data presented so far yield some interesting information regarding the nature of the excited state. Notably, the molecules that exhibit photo-reactivity (**AnSO** and **$AnSO_2$**) exhibit multi-exponential photoluminescence with a component significantly longer-lived than that of **AnS**. While it's not clear why an increase in oxidation state would result in a longer - lived excited state (perhaps due to increased CT character) the formation of both **BA** and the bridged dimer (**AnD**) require significant geometry changes. Accordingly, albeit not necessarily causally, a longer-lived excited state could allow for the requisite geometric configuration(s) to be achieved. Besides the respective photoproducts, the major difference between **AnSO** and **$AnSO_2$** is the oxygen dependence of **BA** formation. This oxygen sensitivity implies the formation of a triplet state during the formation of **BA**.

To further explore the possibility of a triplet excited-state, the reactivity of **AnSO** was monitored in the presence of a triplet sensitizer tris(2,2'-bipyridine) ruthenium dichloride [**$Ru(bpy)_3Cl_2$**]. This ruthenium species is suitable as a triplet photosensitizer because the metal-to-ligand charge transfer (MLCT) absorption has a maximum near 450 nm and absorption is present to about 500 nm, allowing for selective long wavelength excitation of the **$Ru(bpy)_3Cl_2$** in the presence of **AnSO** (Figure 3.13a). Furthermore, due to the presence of a heavy atom, ruthenium polypyridyl dyes are known to exhibit quantitative formation of triplet excited states (^{3}MLCT) only picoseconds after light absorption.[181] Accordingly, dilute solutions of **AnSO** with 10 mol% **$Ru(bpy)_3Cl_2$** in dichloromethane were irradiated at 475 nm using a wavelength tunable nanosecond laser and kinetic information was extracted by

monitoring the loss of absorption at 410 nm in the presence and absence of the triplet sensitizer (Figure 3.13b).

Table 3.3. Rate constants (*k*) for the formation of **BA** from **AnSO** in air, and sparged with argon.

AnSO	***k* (s^{-1})**	
Concentration (10^{-6})	**AIR**	**ARGON**
2	0.08 (±0.001)	0.33 (±0.07)
5	0.065 (0.002)	0.29 (±0.02)
7	0.057 (±0.001)	0.21 (±0.02)
9	0.045 (±0.001)	—
12	0.037 (±0.003)	0.20 (±0.01)
15	—	0.16 (±0.01)

Without the photosensitizer, excitation at 475 nm causes only a slight decrease in **AnSO** concentration. When 10 mol% of the ruthenium photosensitizer is added to the solution, rapid depletion of **AnSO** results upon excitation at 475 nm. These results indicate a few important characteristics of the **AnSO** to **BA** mechanism summarized in Scheme 3.2. First, the experiment without the photosensitizer indicates that energy transfer from the ruthenium dye to **AnSO** is inducing the formation of **BA**. Secondly, the ruthenium dye exhibits a triplet excited state when it "encounters" **AnSO**, indicating that a triplet state is involved in the formation of **BA**. The conservation of spin (angular momentum) does not allow the direct formation of an excited singlet state [^{1}**(AnSO)**] during energy transfer from the triplet excited (^{3}MLCT) ruthenium dye to **AnSO**, thus the resulting excited **AnSO** species should also possess triplet character [^{3}**(AnSO)**]. Scheme 3.2 and equations 3.1-3.6 show the key steps in the [**Ru(bpy)$_3$**]$^{2+}$ sensitization mechanism.

While the sensitization data in Figure 3.13 show that the formation of **BA** involves ^{3}**(AnSO)**, it is also possible that triplet-triplet annihilation (TTA) could result (Scheme 3.2).[182] In this scenario, two equivalents of ^{3}**(AnSO)** encounter one another and yield one equivalent of singlet **AnSO** [^{1}**(AnSO)**] and one equivalent of ground state **AnSO**. Additionally, TTA is well known to occur in various anthracences

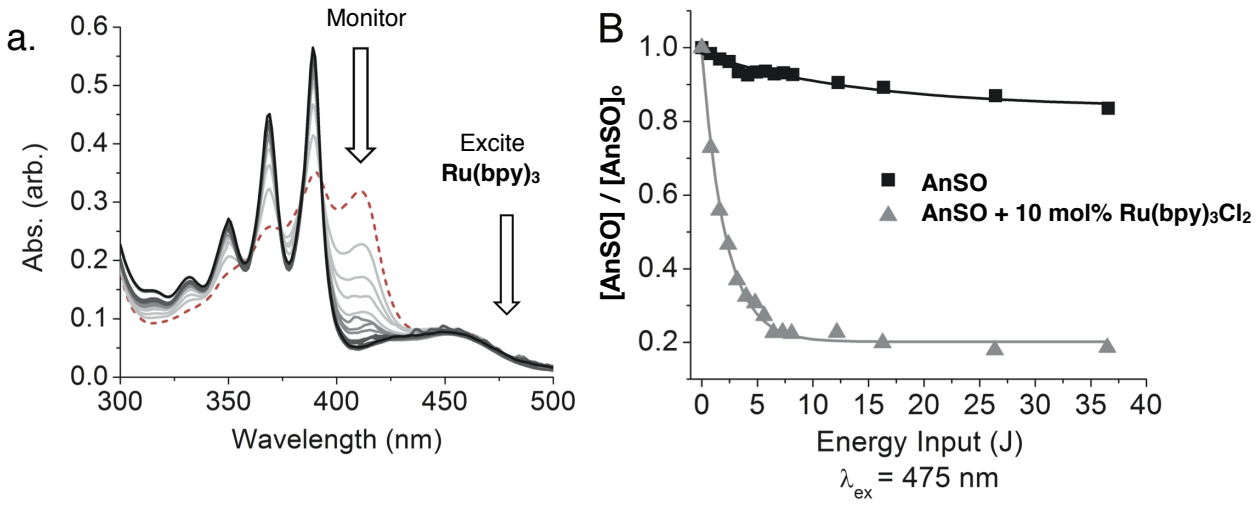

Figure 3.13. (a) Change in UV-Vis spectrum for the conversion of **AnSO** to **BA** in the presence of **Ru(bpy)$_3$** triplet sensitizer. (b) Change in **AnSO** concentration as a function of energy input (see Experimental Details) in the presence, and absence of **Ru(bpy)$_3$** photosensitizer.

Scheme 3.2. Mechanism for triplet sensitization of **AnSO** using **Ru(bpy)$_3$Cl$_2$** selectively excited at 475 nm showing formation of **BA** either directly through a triplet state [^{3}**(AnSO)**] or through a singlet state [^{1}**(AnSO)**] formed through a triplet-triplet annihilation mechanism (TTA).

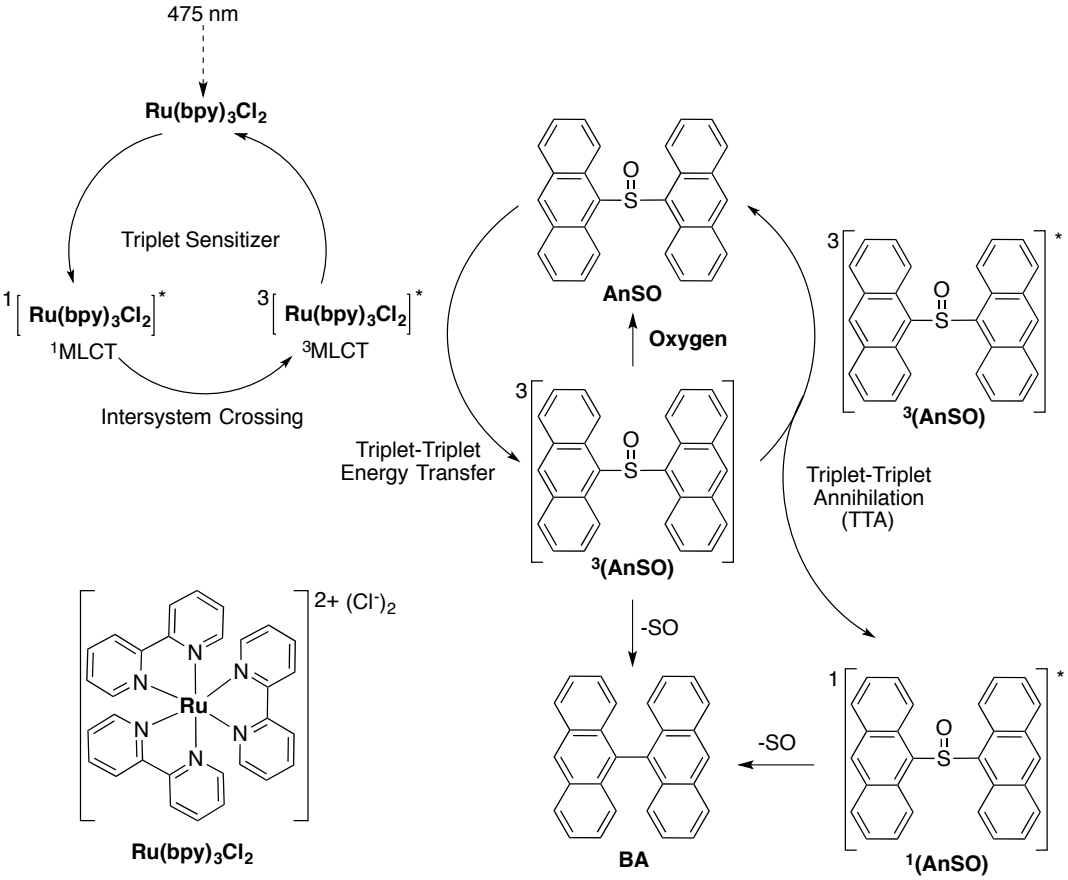

at high concentrations.[20] Triplet-triplet annihilation could also explain the bi-exponential PL lifetimes observed for **AnSO.** Regardless of whether the formation of **BA** occurs directly from a triplet state, or through a singlet state that results from TTA, the involvement of a triplet state in the rate limiting step distinguishes the reactivity of **AnSO** from **$AnSO_2$**.

(3.1)	hv + **$Ru(bpy)_3Cl_2$** ⟶ ^{1}[**$Ru(bpy)_3Cl_2$**]	Excitation 475 nm
(3.2)	^{1}[**$Ru(bpy)_3Cl_2$**] ⟶ ^{3}[**$Ru(bpy)_3Cl_2$**]	Intersystem Crossing
(3.3)	**AnSO** + ^{3}[**$Ru(bpy)_3Cl_2$**] ⟶ ^{3}(**AnSO**) + **$Ru(bpy)_3Cl_2$**	Triplet-Triplet Energy Transfer
(3.4)	^{3}(**AnSO**) ⟶ **BA** + SO	Triplet Reaction Pathway
(3.5)	^{3}(**AnSO**) + ^{3}(**AnSO**) ⟶ ^{1}(**AnSO**) + **AnSO**	Triplet-Triplet Annihilation
(3.6)	^{1}(**AnSO**) ⟶ **BA** + SO	Singlet Reaction Pathway

Another question regarding the formation of **BA** from **AnSO** is whether this occurs intramolecularly or through a dissociative, intermolecular mechanism. To probe this, a dimethyl analogue of **AnSO** (**Me_2AnSO**) was synthesized and a solution of 1:1 **AnSO**/**Me_2AnSO** was exposed to UV light (Figure 3.14). If the formation of **BA** occurs intermolecularly, the photolysis products of the 1:1 mixture of **AnSO**/**Me_2AnSO** should yield three different products: 9,9'-bianthryl (**BA**), 10,10'-dimethyl-9,9'-bianthryl (**Me_2BA**) and the mixed product 10-methyl-9,9'-bianthryl (**MeBA**, Figure 3.14). The reaction products of the mixed photolysis were analyzed using mass spectrometry (GC-MS) which showed only the symmetric products **BA** and **Me_2BA**. The lack of the mixed (cross) product **MeBA** suggests that the loss of the SO bridge occurs intramolecularly.

3.7 Discussion and Mechanism Proposal

The data presented in the preceding sections provide the foundation for a proposed mechanism for the disparate photochemistry of sulfur-bridged anthracenes. For all **$AnSO_n$** the absorbance spectra are similar, somewhat red-shifted and broader than that of unsubstituted anthracene. In all cases, the

broadening can be attributed to weak anthracene to anthracene orbital (π -π) interaction facilitated by the sulfur bridge. This π -π interaction can also be attributed as the cause of the broad and red-shifted photoluminescence. The photoluminescence of **AnSO** and **AnSO$_2$** shows solvatochromic behavior typical of charge transfer molecules. However, the photoluminescence observed in samples of **AnSO** may actually arise from trace amounts of **BA** in solution. For the sulfide (**AnS**) in non-polar solvent the presence of structured photoluminescence is likely due to excimer emission, however, the origin of this interaction may be due to intermolecular aggregation and not between bridged anthracenes. Nevertheless, both the lack of CT emission and the prominence of structured, short wavelength PL, which resembles unsubstituted anthracene, indicates that coupling between S-bridged anthracene (**AnS**) is minimal. This argument is further supported by the short-lived photoluminescence of **AnS**, similar to S-bridged terthiophene (**T3S**) in Chapter 2. It is likely, based on the calculations performed in Chapter 2 (Section 2.6.4), that the sulfur lone pairs in **AnS** screen the electronic coupling between anthracene molecules, resulting in short-lived weak fluorescence and no photo reactivity.

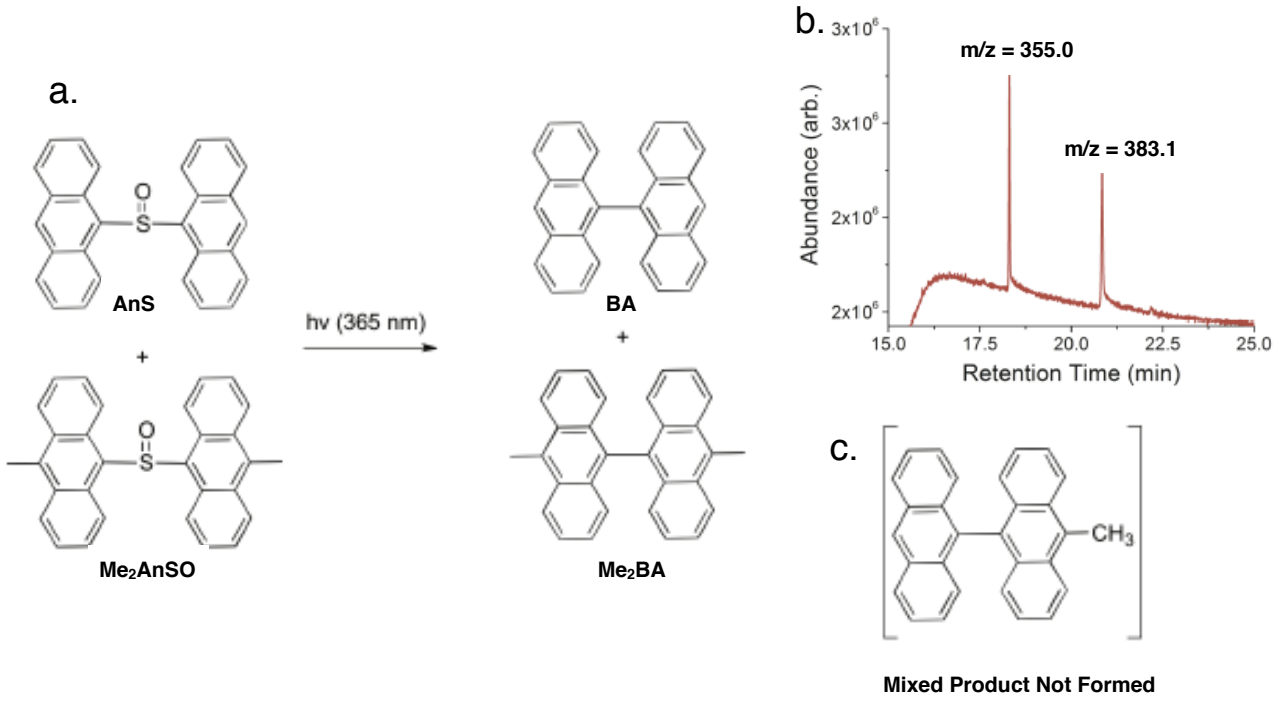

Figure 3.14. (a) Scheme showing the structures of **AnSO** and **Me$_2$AnSO** which were co-dissolved (1:1 molar ratio) and subjected to UV exposure. Gas chromatography Mass Spectrometry (GC-MS) of the irradiated mixture (b) shows only the homo-coupled products **BA** and **Me$_2$BA** and no formation of the cross-product **MeBA** (c).

The solvatochromic behavior of **AnSO**, while indistinguishable from the photoproduct **BA**, clearly indicates the contribution of CT to the excited-state (Figure 3.8). Likewise, the solvatochromic behavior of **AnSO$_2$** is typical of CT emission, albeit as a superposition of short and long wavelength emission in the most polar solvent. For both **AnSO** and **AnSO$_2$**, the PL lifetimes exhibit bi-exponential decays with a long-lived ~30 ns component, significantly longer than the prompt PL lifetime for **AnS**. These data suggest that as the sulfur bridge is oxidized, that communication between anthracene units is facilitated through both a decrease in lone-pair "screening" and electron exchange (CT) contributions. In particular, the longer lived photoluminescence lifetimes for **AnSO** and **AnSO$_2$** suggest that interaction between bridged anthracenes in the excited state through both excimer formation and charge transfer, facilitates the observed reactivity.

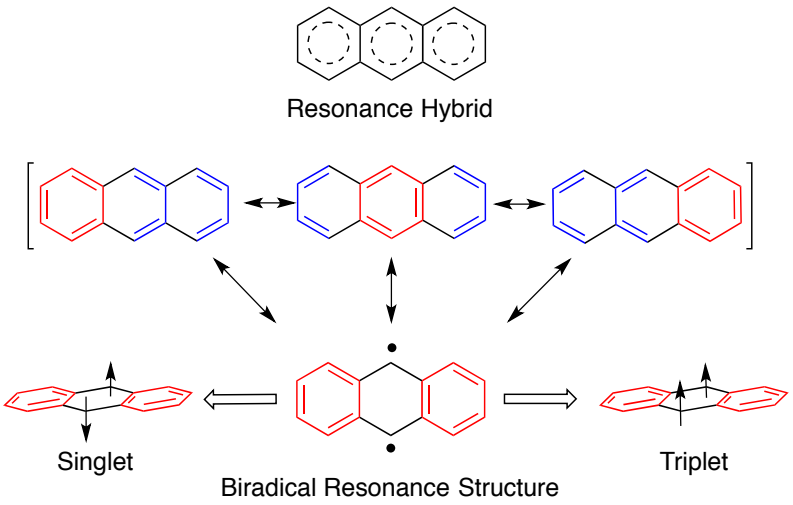

Figure 3.15. Resonance structures of anthracene showing a single benzene ring (red) with two additional diene-like rings (blue). An additional resonance structure, containing two benzene-like rings and two unpaired electrons (diradical) in the 9 and 10 positions is also shown.

What differentiates the reactivity of **AnSO** and **AnSO$_2$** from one another (other than the observed products) is the significant oxygen sensitivity of the photochemistry of **AnSO**. Both the enhanced rate of reaction of **AnSO** in the absence of oxygen and the [**Ru(bpy)$_3$**]$^{2+}$ sensitization results suggest that the

formation of **BA** involves a triplet excited-state. Conversely, the lack of oxygen sensitivity in the formation of the bridged dimer suggests that the reactivity of **AnSO$_2$** occurs through a singlet state.

To further rationalize the triplet vs. singlet reactivity observed in **AnSO** vs. **AnSO$_2$** (respectively) it is worth considering the electronic structure of anthracene. With 14 π electrons, anthracene is typically shown as a tricyclic molecule containing one 6π electron benzene ring attached to two 4π electron "dienes" (Figure 3.15). The biradical character of anthracene can exhibit either singlet or triplet spin configurations.

Scheme 3.3. Proposed biradical (a-c) and Norrish Type I (d-f) mechanisms for the formation of **BA**. The proposed orbital and spin interactions of (a - b) are further illustrated below (red and blue).

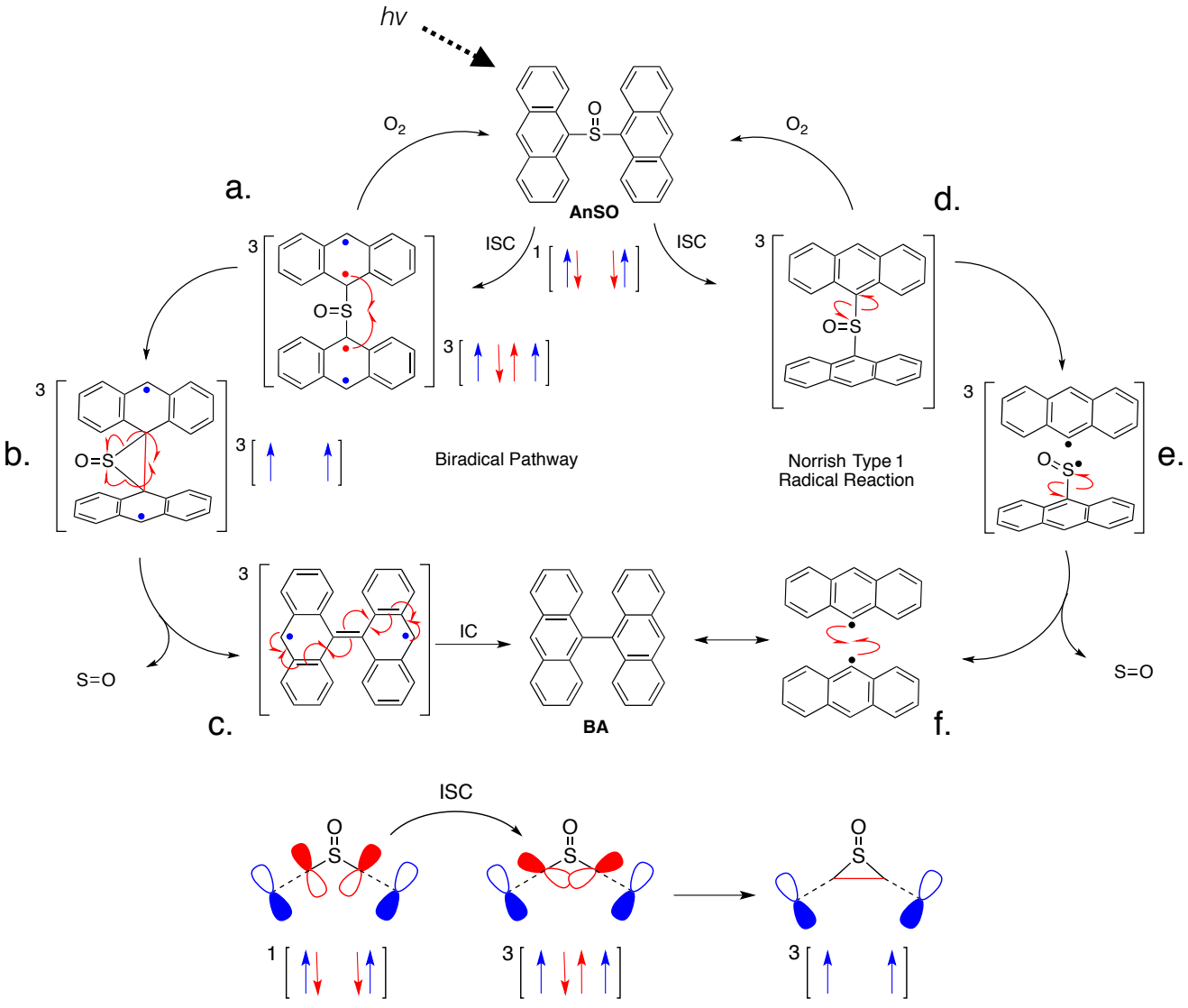

Based on the assumption that a triplet state is involved in the formation of **BA**, two separate reaction pathways are proposed (Scheme 3.3). The first proposed mechanism (Scheme 3.3a-c) involves the formation of a singlet biradical intermediate that undergoes intersystem crossing to the triplet state (Scheme 3.3a). This triplet biradical can also be quenched by oxygen through triplet-triplet energy transfer yielding the singlet ground-state of **AnSO**. Following ISC, the electrons (anti-parallel spins) on each of the bridgehead carbons (C-S) pair up to form a new carbon-carbon bond, yielding a three-membered bridged (SO) intermediate (Scheme 3.3b). Formation of the new C-C bond leaves two unpaired (parallel) electrons in the 10 and 10' positions with overall triplet character. In the final step, SO is released and the biradical rearranges (internal conversion, Scheme 3.3c) to form the more stable ground-state configuration 9,9'-bianthryl (**BA**). Like O_2, the sulfur monoxide (SO) also has a triplet ground state. Although the triplet configuration is more stable, the extrusion of SO in the formation of **BA** from **AnSO** could have either singlet or triplet electronic structure.[183]

The second proposed reaction pathway involves two sequential homolytic carbon-sulfur bond cleavage steps (Scheme 3.3d and e) to yield two equivalents of radical anthracene and free SO, likely in the triplet ground state. The two equivalents of radical anthracene, with anti-parallel spins (overall singlet state), then recombine to form the photoproduct **BA** (Scheme 3.3f). This second mechanism is based on the Norrish Type I reaction, which occurs in aryl and alkyl carbonyls (CO).[184] Additionally, the cleavage of the C-S bond in alkyl and aryl sulfoxides has been proposed as a mechanism for the photochemical racemization of chiral sulfoxides.[185]

The mechanism for the formation of the bridged dimer from **$AnSO_2$** likely involves a singlet excited state, based on the lack of oxygen sensitivity. The formation of 9-9',10-10' bridged anthracenes from unsubstituted and symmetrically tethered anthracene starting materials has been established previously (Scheme 3.4).[169,172] In the absence of a tether, or chemical linker between the two anthracene units the dimerization mechanism is thought to proceed through co-facial (excimer) interaction between one equivalent of photo-excited anthracene and one equivalent of ground-state anthracene (Scheme 3.4). The An-An excimer intermediate (singlet state) then undergoes a concerted $4\pi + 4\pi$ cyclodimerization reaction to yield the dimer.

Tethered anthracene on the other hand, for instance two anthracene linked symmetrically about the 9 and 9' positions with a CH_2 bridge appears to go through a singlet charge transfer (^1CT) intermediate, based on solvatochromic photoluminescence and transient absorption experiments. As discussed in the theory section of Chapter 2 (Section 2.6.4) a CH_2 linker between terthiophene units was calculated to possess similar charge transfer contribution to the excited-state wave function as the SO_2 linker (**T3SO$_2$**) based on the lack of electron lone-pair shielding. As such, it is not unreasonable that similar CT behavior as the CH_2-bridged anthracenes should be observed for the SO_2 linker (**AnSO$_2$**). Furthermore, the solvatochromic behavior observed in the photoluminescence of **AnSO$_2$** suggests contribution from a CT state. Accordingly, the most likely mechanism for the photodimerization of **AnSO$_2$** should involve a polar, CT intermediate (Scheme 3.5, middle). This pathway is preferred over two other proposed possibilities, including concerted 4π + 4π cyclodimerization (Scheme 3.5, left) and a stepwise biradical recombination (Scheme 3.5, right).

Scheme 3.4. Previously reported (Refs. 169, 172) photo-dimerization mechanisms for unsubstituted anthracene (top) and alkyl-linked anthracene (bottom).

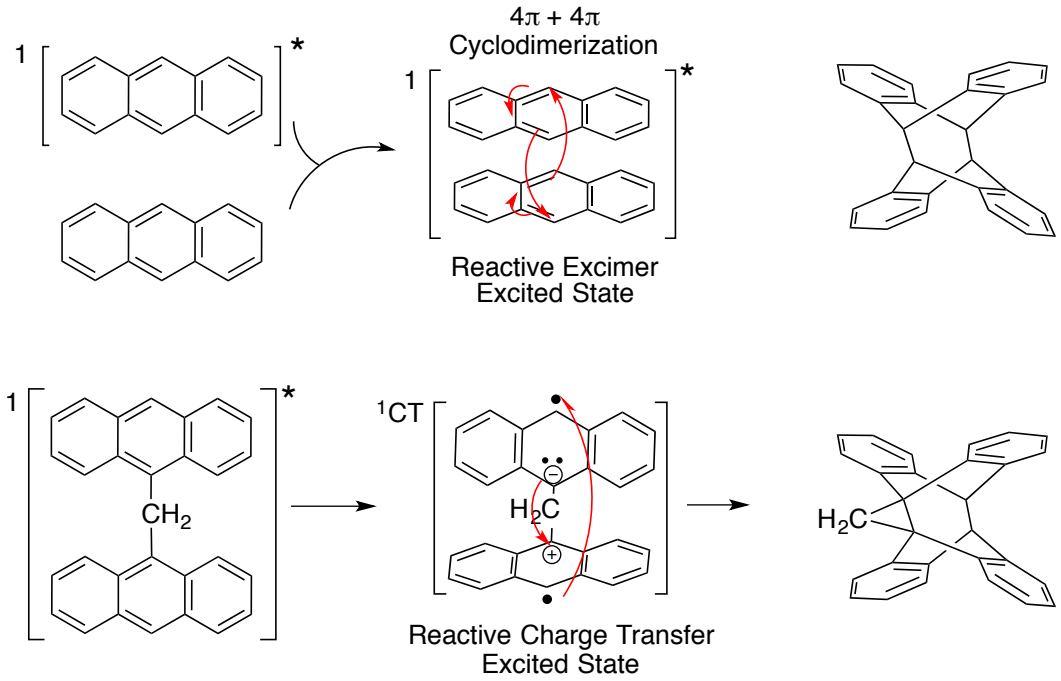

Scheme 3.5. Proposed photochemical pathways for the photochemical dimerization of **AnSO₂**. The favored pathway involving the CT intermediate is highlighted in blue.

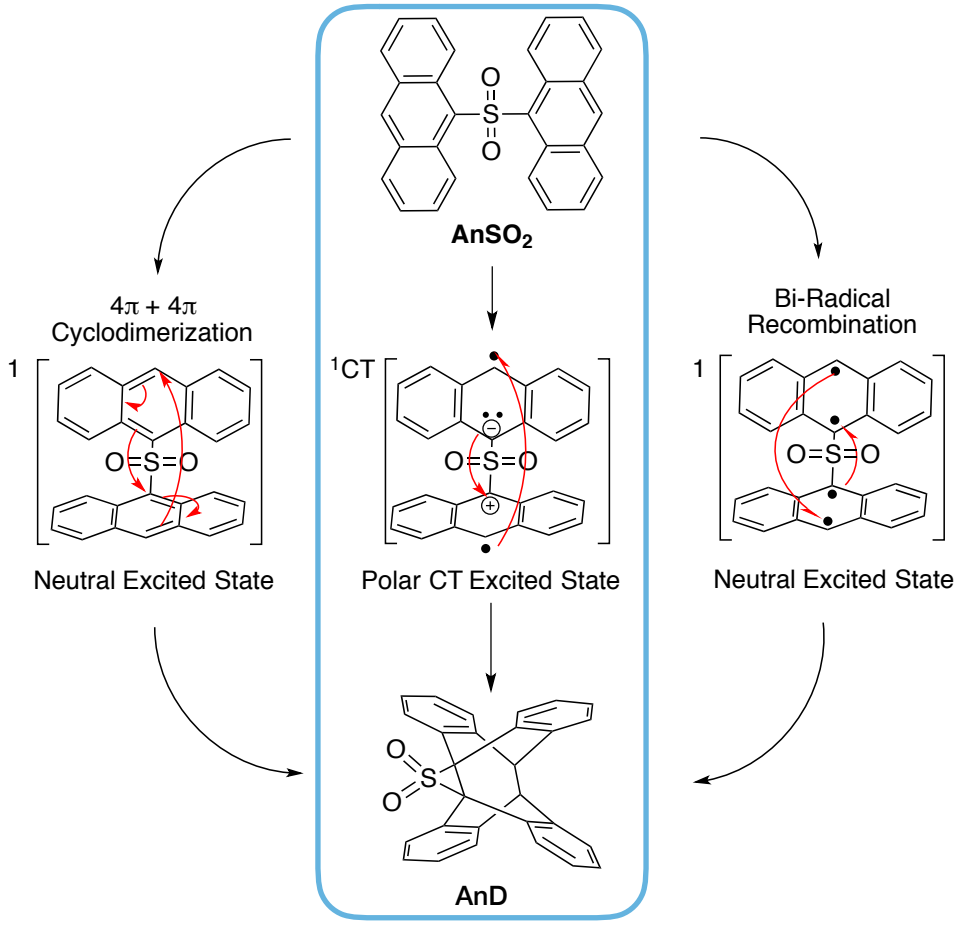

3.8 Conclusions

In summary, the photochemistry of sulfur-bridged anthracene (**AnSOₙ**) was shown to be dependent on the oxidation state of the bridging sulfur. No reactivity and only weak short-lived photoluminescence is observed for the sulfide **AnS** while 9,9'-bianthryl (**BA**) and an episulfone-bridged 9-9',10-10' anthracene dimer (**AnD**) were obtained from **AnSO** and **AnSO₂**, respectively. The difference in reactivity is likely due to an increased electronic interaction between bridged anthracene (S < SO < SO_2) with the reactivity of **AnSO₂** involving a significant amount of charge transfer between bridged anthracenes.

The formation of **BA** from **AnSO** likely involves a triplet excited state as determined by a significant increase in rate in the absence of oxygen and the clean and efficient conversion to **BA** in the presence of a triplet sensitizer [**Ru(bpy)$_3$**]$^{2+}$. The lack of oxygen sensitivity in the rate of formation of **AnD** suggests that this reaction proceeds through a singlet excited state, in agreement with previously reported photochemical anthracene dimerization reactions. The favored, proposed mechanism for the formation of **BA** from **AnSO** involves a triplet, bis-biradical intermediate. The favored, proposed mechanism for the formation of **AnD** from **AnSO$_2$** involves a polar, CT intermediate.

Besides the unique reactivity of this set of S-bridged molecules, the formation of a highly emissive photoproduct (**BA**) from a very weakly emissive starting material (**AnSO**) is a noteworthy photochemical process. In Chapter 4, the rapid photochemical transformation of **AnSO** into **BA** is leveraged to form fluorescent images for application in anti-counterfeit technology.

3.9 Experimental Details

3.9.1 General

9-Bromoanthracene (>95%) and 9,10-dibromoanthracene (>98%) were purchased from TCI and used without further purification. Meta-chloroperoxybenzoic acid (*m*-CPBA, 70-75%) was purchased from Acros Organics and recrystallized from dichloromethane before use. Ru(bpy)$_3$Cl$_2$ (bpy = 2,2'-bipyridine) was purchased from Strem Chemicals and was used as received. Solution 1D and 2D nuclear magnetic resonance (NMR) experiments were performed on a either a 300 or 400 MHz Bruker spectrometer in CD_2Cl_2. Infrared spectroscopy was performed on an attenuated total reflection (ATR) crystal using a Perkin-Elmer Frontier FT-IR spectrometer. Powder X-ray diffraction (PXRD) data were recorded on a 60 Bruker D8 Advance X-ray diffractometer using copper Kα radiation at 40 kV, 40 mA. UV-vis absorption spectroscopy was performed on a Varian Cary 5000 spectrophotometer. Corrected emission measurements were performed on a PTI QuantaMaster 50 fluorimeter at room temperature in analytical (HPLC) grade cyclohexane, dichloromethane, and acetonitrile from Fisher Scientific. All spectroscopy was performed in the presence of air unless otherwise specified. For spectroscopy performed

under argon, all samples were sparged with >99.9% argon for at least 15 minutes prior to measurement. Photoirradiation experiments were performed in analytical HPLC grade solvents from Fisher Scientific, or in CD_2Cl_2 from Sigma Aldrich. All solvents were used as purchased without further purification. Triplet photosensitization experiments were performed using a Continuum PL8010 pulsed laser operating at 10 Hz which pumped a Panther optical parametric oscillator (OPO) at 355 nm. The output from the OPO was tuned to 475 nm for all photosensitization experiments. The power incident on the sample was measured using two separate power meters (A and B) as shown in Figure 3.17. Experiments involving UV exposure to either **AnSO** or **$AnSO_2$** were performed using either a handheld lamp (365 nm, Entela), a 400 nm laser pointer (≤5 mW), or a computer controlled 400 nm UV LED (Wajun technologies).

3.9.2 Crystal Structure Solution and Refinement of AnD

The SO_2-bridged photo-dimer (**AnD**) crystallizes as a two-component twin with components one and two related by a 180º rotation about the (1 0 1) real axis (Figure 3.3). Data were integrated for both components, including both overlapped and non-overlapped reflections. In total 20,963 reflections were integrated (8,481 from component one only, 8,456 from component two only, 4,026 overlapped). Data were collected and integrated using the Bruker SAINT[186] software packages. The linear absorption coefficient, m, for Mo-Ka radiation is 1.87 cm^{-1}. Data were corrected for absorption effects using the multi-scan technique (TWINABS)[187₂] with minimum and maximum transmission coefficients of 0.924 and 0.993, respectively. The data were corrected for Lorentz and polarization effects.

The structure of **AnD** was solved by direct methods[188₃] using de-convoluted data from the major twin component. Subsequent refinements were carried out using an HKLF 4 format data set containing complete data from component one. The material crystallizes with two crystallographically independent half-molecules in the asymmetric unit, each half-molecule residing near an inversion center that generates the second half-molecule. Since the molecule itself does not have inversion symmetry, the sulfone group of each molecule is disordered about these inversion

centers. Figure 3.3 shows the expected orientations of the two molecules with respect to each other. All non-hydrogen atoms were refined anisotropically. All hydrogen atoms were placed in calculated positions. The final cycle of full-matrix least-squares refinement[189] on F2 was based on 3644 reflections and 321 variable parameters and converged (largest parameter shift was 0.00 times its esd) with unweighted and weighted agreement factors of:

$$R_1 = S \; ||F_o| - |F_c|| \; / \; S \; |F_o| = 0.108$$

$$wR_2 = [\; S \; (\; w \; (F_o^2 - F_c^2)^2 \;) / \; S \; w(F_o^2)^2]^{1/2} = 0.159$$

The standard deviation of an observation of unit weight[190] was 1.23. The weighting scheme was based on counting statistics. The maximum and minimum peaks on the final difference Fourier map corresponded to 0.27 and –0.34 ($e^-/Å^3$), respectively. Neutral atom scattering factors were taken from Cromer and Waber.[191] Anomalous dispersion effects were included in Fcalc;[192] the values for Df' and Df" were those of Creagh and McAuley.[193] The values for the mass attenuation coefficients are those of Creagh and Hubbell.[194] All refinements were performed using the SHELXL-2012[195] via the OLEX2[196] interface.

3.9.3 Kinetic Experiments

In order to measure accurately the kinetics of **AnSO** to **BA**, and **$AnSO_2$** to **AnD**, a custom made computer controlled LED setup was used to irradiate dilute solutions while simultaneously measuring change in absorbance (Figure 3.16). An Arduino micro-controller enables control over LED exposure times with microsecond precision. In a typical experiment the LED was turned on in one second intervals and between each exposure a new UV-Vis spectrum was taken. According to the Beer-Lambert relationship, the change in absorbance as a function of time (dA/dt) is directly related to the change in concentration (dc/dt) (equations 3.7 and 3.8).

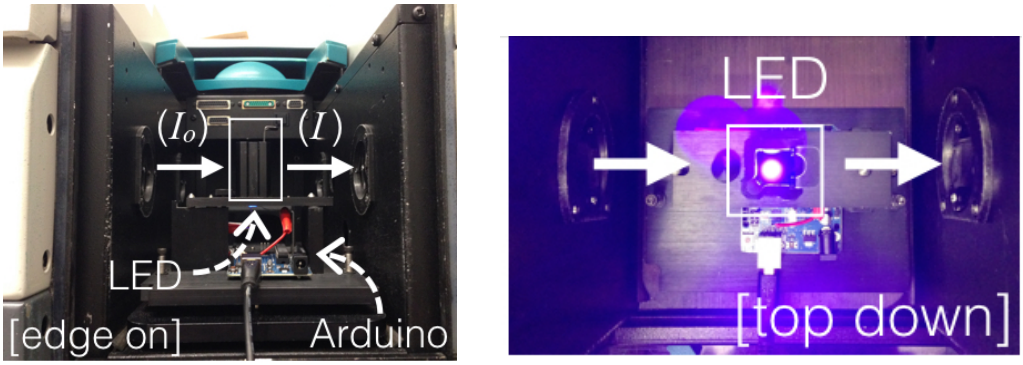

(3.7) $$A = -ln\left(\frac{I}{I_o}\right) = \varepsilon lc$$

(3.8) $$\frac{dA}{dt} = (\varepsilon l)\frac{dc}{dt}$$

Figure 3.16. Images showing the computer-controlled LED setup edge on (a) and from the top down (b) which interfaces directly with the Varian Cary 5000 UV-Vis spectrometer. Equations 3.7 and 3.8 showing the derivation of of the Beer-Lambert law that enables direct correlation of the change in measured absorbance (*dA/dt*) to the change in concentration (*dc/dt*).

3.9.4 Triplet Sensitization

Dilute solutions of **AnSO** (10^{-6} M) were prepared by adding 10 mol% **Ru(bpy)$_3$Cl$_2$**, all dissolved in dichloromethane, sparging with argon for at least 20 min prior to photoirradiation. Triplet photosensitization experiments were performed using a Continuum PL8010 pulsed laser operating at 10 Hz pumping a Panther optical parametric oscillator (OPO) at 355 nm. The output from the OPO was tuned to 475 nm for all photosensitization experiments in order to selectively excite the **Ru(bpy)$_3$** photosensitizer. The power incident on the sample was measured using two separate power meters (A and B) as shown in Figure 3.17. Light exiting the OPO was passed through a beam splitter and into both power meter A and the sample. Measurements were taken at power meter A and the ratio of the readings at A and B without any sample present (A/B) was used to correct the measurements for the relative amount of light passing through the beam splitter, which varied with the wavelength used. The double power meter setup also allowed for calculation of the amount of light (energy, J) absorbed by the samples.

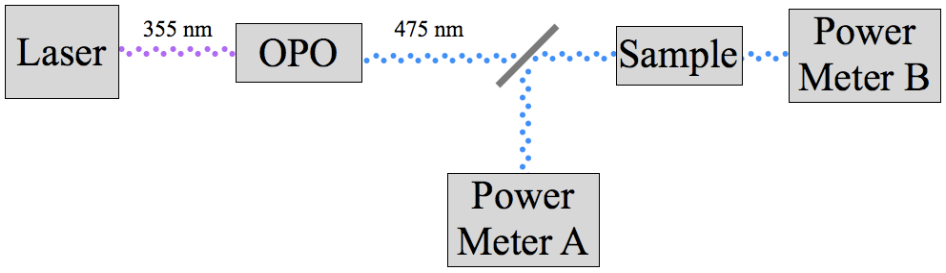

Figure 3.17. Illustration showing the experimental setup used in the **Ru(bpy)$_3$** triplet sensitization experiment to measure to amount of energy absorbed by the sample.

3.9.5 Synthesis

9,9′-bis(anthracene)sulfide (AnS). 9-Bromoanthracene (1.0 g, 4.0 mmol), potassium thioacetate (0.2 g, 2.0 mmol), and tribasic K_3PO_4 (1.0 g, 4.7 mmol) were dissolved in a 2:1 mixture of toluene and acetone (30 mL) and the solution purged with nitrogen. In a separate vessel $Pd(dba)_2$ (0.1 g, 0.2 mmol) and dppf (0.15 g, 0.3 mmol) were dissolved in 10 mL 2:1 toluene/acetone and stirred for 10 minutes before adding (drop-wise) to the 9-bromoanthracene mixture. The dark yellow/orange solution was heated at reflux for 48 h. Silica gel (~2 g) was added to the mixture and all of the solvent was removed. The dry silica, with adsorbed crude product, was then loaded onto a silica gel column and the product was eluted using 4:1 hexanes/dichloromethane to afford 250 mg, 0.6 mmol, 30%) of a yellow powder. The solid was recrystallized from 4:1 hexanes/dichloromethane to afford yellow needles of **AnS**. ^{1}H NMR (400 MHz, CD_2Cl_2): δ 8.81 (dd, 4H, *J* = 0.9, 8.8 Hz), 8.49 (s, 2H), 8.03 (d, 4H, J = 8.6 Hz), 7.47 (dd, 2H, *J* = 0.9, 6.7 Hz), 7.44 (dd, 2H, *J* = 0.9, 6.7 Hz), 7.39 (dd, 2H, *J* = 1.5, 6.7 Hz), 7.37 (dd, 2H, *J* = 1.2, 6.4 Hz). ^{13}C NMR (100.6 MHz, CD_2Cl_2): δ 133.7, 132.4, 131.4 , 129.8, 129.1, 127.3, 126.4, 125.9. HRMS: calculated m/z: 386.1129, found (ESI) m/z: 386.1134. m.p. 264 – 266 ºC.

9,9′-bis(anthracene)sulfoxide (**AnSO**): *m*-CPBA (19 mg, 0.1 mmol) was added to a solution of **AnS** (43 mg, 0.1 mmol) in dichloromethane (15 mL) which was heated to reflux and stirred overnight in the dark.

After this time, the reaction mixture was poured into a saturated aqueous solution of sodium bicarbonate and ice, and was then extracted with dichloromethane. The organic layers were combined, dried over anhydrous magnesium sulfate, filtered, and concentrated to afford a yellow solid. Purification was by column chromatography (silica, dichloromethane) and the product was recrystallized from 4:1 hexanes/ dichloromethane to afford long yellow crystalline needles of **AnSO**. Yield: 8.9 mg, 0.06 mol 60%. ^{1}H NMR (400 MHz, CD_2Cl_2): δ 9.28 (d, 4H, *J* = 8.8 Hz), 8.57 (s, 2H), 8.03 (dd, 4H, *J* = 1.8, 7.6 Hz), 7.49 (dd, 2H, *J* = 0.9, 5.5 Hz), 7.47 (dd, 2H, *J* = 1.8, 5.0 Hz), 7.45 (dd, 2H, *J* = 2.1, 6.8 Hz), 7.44 (dd, 2H, *J* = 1.6, 6.4 Hz). ^{13}C NMR (100.6 MHz, CD_2Cl_2): δ 134.7, 132.9, 131.8, 131.2, 130.0, 128.1, 125.9, 123.7. HRMS: calculated m/z: 402.10784, found (EI) m/z: 402.10748. m.p.: dec. > 150 ºC. IR (neat): (ν SO) 1049 cm^{-1}.

9,9′-bis(anthracene)sulfone (**$AnSO_2$**): To a solution of **AnS** (30 mg, 0.1 mmol) in dichloromethane (15 mL) at room temperature was added recrystallized *m*-CPBA (12 mg, 0.2 mmol) and the mixture was stirred while heating to reflux overnight. After cooling, the reaction mixture was poured into a saturated aqueous solution of sodium bicarbonate (20 mL) and ice, then extracted with dichloromethane. The organic layers were combined, dried over anhydrous magnesium sulfate, filtered, and concentrated to afford a yellow solid. The crude material was purified by column chromatography (silica, dichloromethane) and recrystallized from 4:1 hexanes/ dichloromethane to afford yellow prisms of **$AnSO_2$**. Yield: 16 mg, 0.03 mmol, 50%. ^{1}H NMR (400 MHz, CD_2Cl_2): δ 9.18 (d, 4H, *J* = 8.5 Hz), 8.68 (s, 2H), 8.02 (d, 4H, *J* = 8.3 Hz), 7.47 (dd, 2H, *J* = 0.9, 6.7 Hz), 7.44 (dd, 2H, *J* = 0.9, 6.7 Hz), 7.41 (dd, 2H, *J* = 1.5, 6.4 Hz), 7.39 (dd, 2H, *J* = 1.5, 6.4 Hz). ^{13}C NMR (100.6 MHz, CD_2Cl_2): δ 136.1, 134.5, 131.4, 130.4, 129.9, 129.1, 125.8, 124.4. HRMS: calculated m/z: 418.10275, found (EI) m/z: 418.10260. m.p.: dec. > 150 ºC. IR (neat): (ν SO_2) 1130 cm^{-1}, 1263 cm^{-1}, and 1298 cm^{-1}.

9,9′-Bianthryl (**BA**): Photoirradiation of **AnSO** (10 mg, 0.03 mmol) in dichloromethane with UV-light (365 nm, 400 nm) yielded **9,9′-bianthryl**. Purification for complete characterization was performed by column chromatography (silica, hexanes), and the resulting solid (8.8 mg, 0.03 mmol, >99% yield) was recrystallized from the same solvent. ^{1}H NMR (400 MHz, CD_2Cl_2): δ 8.76 (s, 2H), 8.22 (d, 2H, *J* = 8.5 Hz), 7.51 (dd, 2H, *J* = 1.2, 6.4 Hz), 7.49 (dd, 2H, *J* = 1.2, 6.7 Hz), 7.20 (dd, 2H, *J* = 1.2, 6.8 Hz), 7.18 (dd, 2H, *J* = 1.3, 6.9 Hz), 7.05 (d, *J* = 8.8 Hz). HRMS: calculated m/z: 354.14073, found (EI) m/z: 354.14085. m.p. 299 – 303 ºC.

SO_2-Bridged Anthracene Dimer (**AnD**): Photoirradiation of **$AnSO_2$** with either 365 nm or 400 nm UV light in the presence of oxygen, or when the solution is spared with argon yields the dimer **AnD**. The photo-product was purified by column chromatography (silica, 1:1 hexane/dichloromethane) and was crystallized from the same solvent. Obtaining a 100% pure sample is difficult by column chromatography as the dimer reverts back to **$AnSO_2$** on silica gel. Extended irradiation of **AnSO** and **$AnSO_2$** either leads to anthraquinone (with oxygen present) or a mixture of decomposition products. For more concentrated samples (~5mg/mL) it was found that a lower energy light source (~400 nm) works best for avoiding the formation of anthraquinone. ^{1}H NMR (400 MHz, CD_2Cl_2): δ 7.55 (dd, 4H, *J* = 1.2, 7.3 Hz), 7.08 (dd, 4H, *J* = 1.2, 7.3 Hz), 7.02 (dd, 2H, *J*= 1.5, 7.6 Hz), 6.98 (dd, 2H, *J* = 1.5, 7.3 Hz), 6.97 (dd, 2H, *J* = 1.2, 6.1 Hz), 6.93 (dd, 2H, *J* = 1.7, 7.7 Hz), 6.92 (dd, 2H, *J* = 1.0, 7.7 Hz), 4.60 (s, 2H). ^{13}C NMR (100.6 MHz, CD_2Cl_2): δ 144.9, 134.6, 128.6, 128.2, 126.6, 126.5, 74.8. 52.6. HRMS: calculated m/z: 418.10275, found (EI) m/z: 418.10255. IR (neat): (ν SO_2) 1130 cm^{-1}, 1263 cm^{-1}, and 1298 cm^{-1}.

Anthraquinone: Photoirradiation of **AnSO** or **$AnSO_2$** with a 365 nm lamp in the presence of oxygen for ~12 h yielded anthraquinone. ^{1}H NMR (400 MHz, CD_2Cl_2): δ 8.30 (d, 2H, *J* = 5.8 Hz), 8.29 (d, 2H, *J* =

5.8 Hz), 7.83 (d, 2H, *J* = 5.8 Hz), 7.82 (d, 2H, *J* = 5.8 Hz). HRMS: calculated m/z: 208.05243, found (EI) m/z: 208.05262. IR (neat) : (ν C=O) 1675 cm-1.

9-bromo-10-methylanthracene: *n*-Butyllithium in hexanes (1.6 M, 1.8 mL, 3.0 mmol) was added to a stirred solution of 9,10-dibromoanthracene (1.0 g, 3.0 mmol) in dry diethyl ether (20 mL) at 0 ºC under nitrogen atmosphere. The resulting bright orange solution was stirred at 0 ºC for 1 h. Iodomethane (2.8 g, 19 mmol) in dry tetrahydrofuran (5 mL) was added to the reaction drop-wise with stirring. Upon complete addition of iodomethane, the orange solution turned pale yellow. The resulting solution was allowed to stir an additional hour at room temperature, after which time water (25 mL) was added to quench the reaction. The organic products were extracted three times with dichloromethane (~ 20 mL each). The organic extracts were combined and dried over $MgSO_4$, filtered and evaporated under reduced pressure. The crude yellow solid was purified by column chromatography (silica, hexanes) to yield a pale yellow solid, 580 mg, 2.0 mmol, 70 %. ^{1}H NMR (300 MHz, CD_2Cl_2): δ 8.57 (d, 2H, *J* = 8.0 Hz), 8.35 (d, 2H, *J* = 7.4 Hz), 7.62 (dd, 2H, *J* = 1.2, 8.5 Hz), 7.56 (dd, 2H, *J* = 1.3, 8.4 Hz), 3.10 (s, 3H). HRMS: calculated m/z = 270.0044 and 272.0044, found (ESI) 270.0051 and 272.0044.

10,10′-Dimethyl-9,9′-dianthryl sulfide (**Me_2AnS**): 9-Bromo-10-methylanthracene (104 mg, 0.4 mmol), potassium thioacetate (22 mg, 0.2 mmol), and tribasic potassium phosphate (97 mg, 0.5 mmol) were mixed together with a 2:1 toluene/acetone mixture (1.5 mL) in a Biotage microwave reaction vial (5 mL volume) and allowed to stir under nitrogen atmosphere. In a separate scintillation vial, $Pd(dba)_2$ (12 mg, 0.02 mmol), and dppf (17 mg, 0.03 mmol) were dissolved in 2:1 toluene/acetone (1.5 mL) and stirred under nitrogen. After ~5 minutes of stirring, the $Pd(dba)_2$/dppf solution was added dropwise with stirring to the 9-bromo-10-methylanthracene mixture. The resulting dark orange mixture was sparged with nitrogen for ~5 minutes before sealing the microwave vial. The mixture was then subjected to microwave irradiation for 1 hour at 145 ℃, maintaining a pressure of 5 – 7 bar. The resulting bright yellow mixture

was worked up first by filtration and washing with dichloromethane until the liquid was clear, followed by rotary evaporation to remove excess solvent. The crude product was then purified by column chromatography on silica gel using a solvent gradient, starting with 100% hexanes and ending with 100% dichloromethane. The product was obtained as a bright yellow powder, 61 mg, 0.16 mmol, 80 %. ^{1}H NMR (300 MHz, CD_2Cl_2): δ 8.91 (d, 4H, *J* = 8.9 Hz), 8.31 (d, 4H, *J* = 8.9 Hz), 7.45 (dd, 4H, *J* =1.2, 6.9 Hz), 7.33 (dd, 4H, *J* = 1.2, 6.6 Hz), 3.08 (s, 6H). HRMS: calculated m/z: 414.1442, found (ESI) m/z: 414.1450.

10,10′-Dimethyl-9,9′-dianthryl sulfoxide (**Me_2AnSO**): A solution of **Me_2AnS** (20 mg, 0.05 mmol) in chloroform (10 mL) was stirred with mild heating to ensure complete solubilization. *m*-CPBA (8 mg, 0.05 mmol) was added and the reaction progress monitored by TLC. After the reaction was complete, the crude product was purified with column chromatography on silica gel, using a gradient of 100% chloroform to 100% ethyl acetate. The pure product **Me_2AnSO** was isolated as a yellow solid, 5 mg, 0.01 mmol, 25%). ^{1}H NMR (300 MHz, CD_2Cl_2): δ 9.33 (d, 4H, *J* = 8.5 Hz), 8.30 (d, 4H, J = 8.2 Hz), 7.44 (dd, 4H, *J* = 1.4, 8.7 Hz), 7.39 (dd, 4H, *J* = 1.4, 8.9 Hz), 3.05 (s, 6H). HRMS: calculated m/z: 431.1470, found (ESI) m/z: 431.1468. IR (neat) : (ν SO) 1040 cm^{-1}.

CHAPTER 4

Multidimensional Photopatterned Fluorescent Images

4.1 Introduction

The World Health Organization broadly classifies the purpose of anti-counterfeit technologies as "… to enable the authentication of an item, by government, industry investigators, or ideally, by the wider public".[197] This is of primary concern in the developing world where counterfeit medication has become a rampant problem.[198,199] For applications in pharmaceuticals in particular, anti-counterfeit technology that enables the individual to authenticate a product are preferred. As such, anti-counterfeit/ authentication technologies should be extremely difficult to replicate, inexpensive enough to become ubiquitous and most importantly, easy to authenticate using equally ubiquitous and inexpensive technologies.

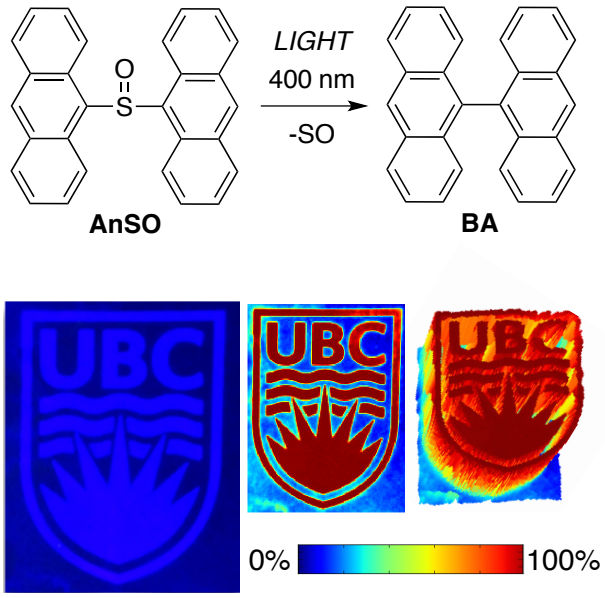

Figure 4.1. Photochemical transformation of weakly fluorescent **AnSO** to highly fluorescent BA (top). Photopatterned, fluorescent image showing the UBC logo and the extracted three-dimensional color intensity.

One type of common anti-counterfeit technology is the use of printed, or patterned fluorescence. Under ultraviolet illumination, the covert fluorescent image emits light in the visible spectrum, enabling rapid (subjective) visual authentication of the item. In most cases, fluorescent images found on passports, banknotes and anti-counterfeit packaging employ images with only a single luminescence intensity. While these features are covert, they lack the ability to display complex information. For instance, in order to pattern fluorescent images with complex features such as human portraits, spatial control over luminescence intensity is required. In this chapter, the photo-reactive small molecule 9,9'-bis(anthracene)sulfoxide (**AnSO**) is used to generate intensely luminescent images with high contrast ratios using light. Furthermore, the photochemistry of **AnSO** is leveraged to generate fluorescent images that have spatially controlled variable luminescence intensity. This method enables rapid access to covert

images with complex information that can easily be read and decoded using the inexpensive CCD camera of a cellphone.

Cellphones have become inexpensive enough that there are an estimated seven billion global subscriptions, of which, more than five billion are in the developing world.[200] Additionally, modern cellphones contain a CCD camera that when coupled with the phone's computational capabilities can be used by the individual to interpret complex information.[201,202] Two-dimensional barcodes, for example QR codes and data matrices, offer the ability to encode a large amount of information in a small and robust (error proof) image that can easily be decoded using modern cellphones (Figure 4.2). However, even if printed in covert fluorescent inks, rendering them invisible to the human eye, these barcodes are easily reproduced by the counterfeiter. The limited security of conventional fluorescent inks is largely due to the fact that a wide variety of organic molecules and polymers will yield very similar photoluminescence (i.e. color). Thus, a simple method whereby the high data storage capabilities of two-dimensional barcodes could be maintained, but with an added level of security that is easily decoded using an inexpensive CCD detector (camera phone), would be highly desirable.

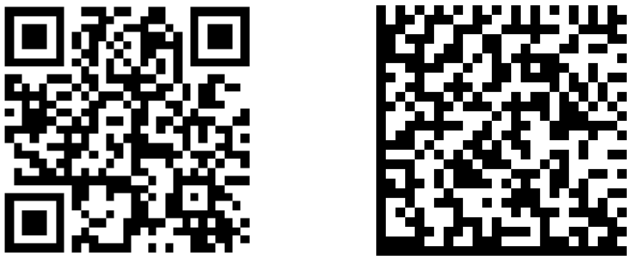

Figure 4.2. Quick response (QR, left) and data matrix (right) codes.

Two-dimensional barcodes, fluorescent or otherwise, actually display three-dimensional information. The black and white squares of a QR code or data matrix (Figure 4.2) correspond to binary 1s and 0s. It is the specific position of the binary data in two dimensional space that enables the storage of information. Accordingly, these barcodes have two-dimensions of positional information and a third dimension corresponding to either an intensity of 1 or 0. If it were possible to vary the intensity at a specific position from some minimal value (0) to some maximum value (1), then the data density of a

given barcode could be significantly increased. Furthermore, if it were possible to create such a variable intensity image using a fluorescent ink, the reproduction of these images would be significantly more difficult than their binary counterparts. The focus of this chapter is the proposal and demonstration of patterned photoluminescence with spatially controlled intensity. These variable intensity, or multidimensional, fluorescent images are proposed as a method for offering enhanced image security for anti-counterfeit applications.

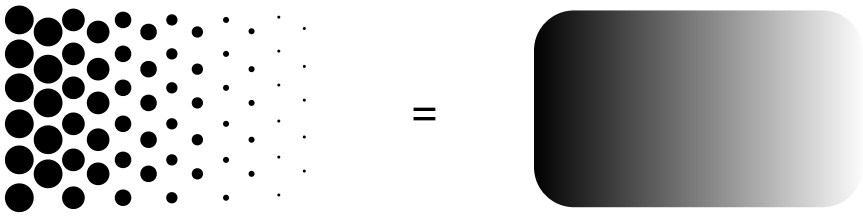

Figure 4.3. Greyscale, or monochrome images can be generated by depositing ink droplets of different sizes and separations, also known as a halftone.

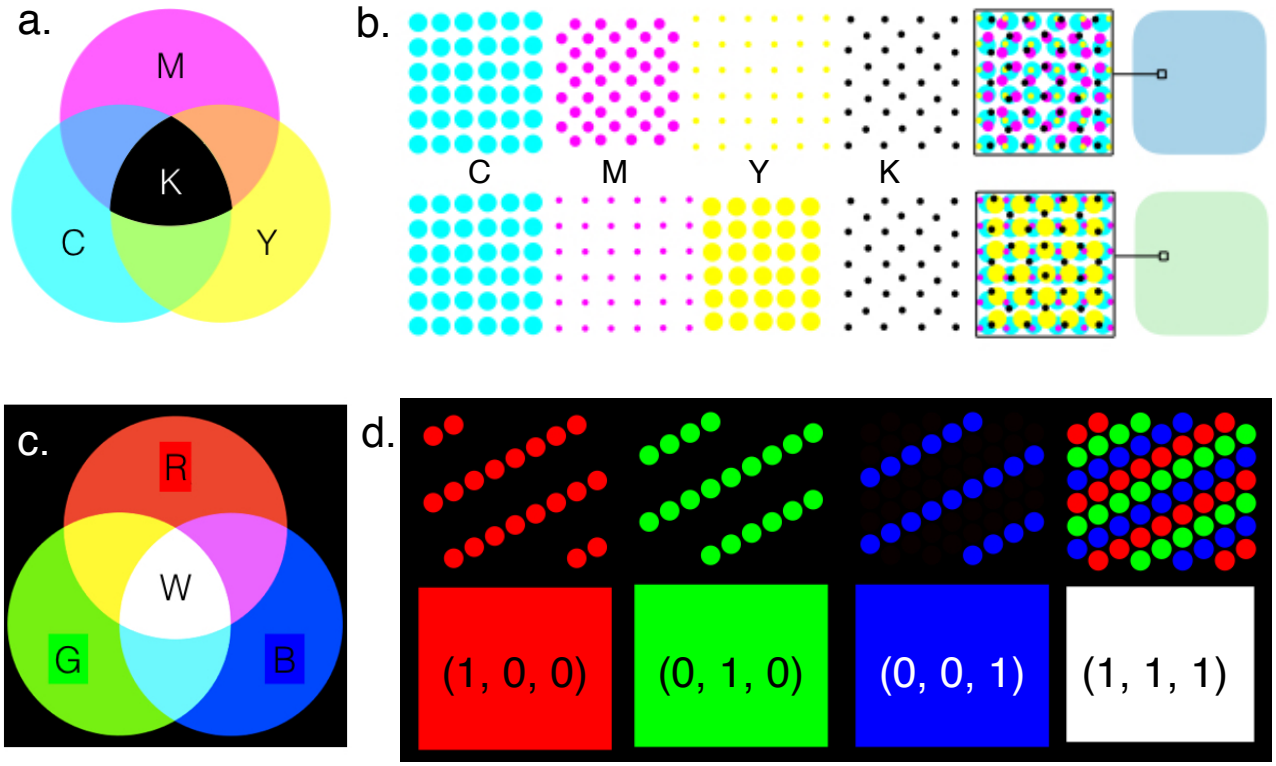

Figure 4.4. (a) Different dot sizes and densities of cyan (C), magenta (M), yellow (Y) and black (K) are used to "subtract" reflected color from the full spectrum white background. Two examples of CMYK colors are shown in (b). Conversely, different intensities ranging from 0 to 1 (0 to 255) of red (R), green (G), and blue (B) are "added" together against a zero color, or black background to access different colors in an additive (R,G,B) color image. (d) Shows independent R, G and B channels and full color white.

In addition to anti-counterfeit technology,[203,204,205,206,207] patterned luminescence is of interest for a variety of applications, including organic light emitting diodes (OLEDs),[208,209,210,211] bio-imaging,[212,213,214,215,216,217] and optical data storage.[218,219,220,221] Like visibly colored inks, fluorescent inks can be patterned using conventional printing methods. Variable fluorescence intensity can be achieved by creating an image "halftone" (Figure 4.3). Halftone (and also dithering) printing involves depositing ink droplets of various sizes and separation (density) that when viewed from afar, the average color intensity appears higher or lower. In full color (visible) printing, halftones of cyan, magenta, yellow and black (CMYK) inks are deposited on a white background (e.g. paper) in order to "subtract" the full spectrum (white) reflectance (Figure 4.4a,b). In contrast to subtractive, CMYK image generation, additive RGB images, such as those found in electronic displays, are created by spatially separating the red, green, and blue colors and varying the intensity of each to achieve full color images (Figure 4.4c,d). In display technology the spatially separated red, green and blue fluorophores or phosphors can be controlled electronically by an external driving circuit. In printing a photoluminescent image, achieving variable intensity of each RGB color is more complicated than using a halftone scheme as with CMYK printing. The issue with printing halftone images using fluorescent or phosphorescent inks is that when multiple inks are used (e.g. RGB), fluorescence quenching can occur due to energy transfer between dye molecules in close proximity that are printed on top of one another. Fluorescence quenching is most likely to occur between inks with overlapping absorption and emission spectra (as is usually the case with different color dye molecules).

A slightly different approach to generating full color fluorescent images would be to pattern spatially separated dots with identical sizes and density, but with variable intensity (Figure 4.5). Such a patterning method would mimic the additive RGB capabilities of an electronically controlled dynamic display (e.g. cellphone screen or television). By controlling the fluorescence intensity of the red, green and blue ink droplets from 0% to 100%, full color images can be generated without the need for a halftone. Figure 4.6 illustrates this proposed printing method, whereby each red, green and blue ink is patterned using a flexographic roll-to-roll process. After depositing each of the RGB inks, the minimally fluorescent "dark" image is exposed to UV light through a rotating, variable transmittance shadow mask that is calibrated to the position of the substrate. This approach would result in spatially resolved red,

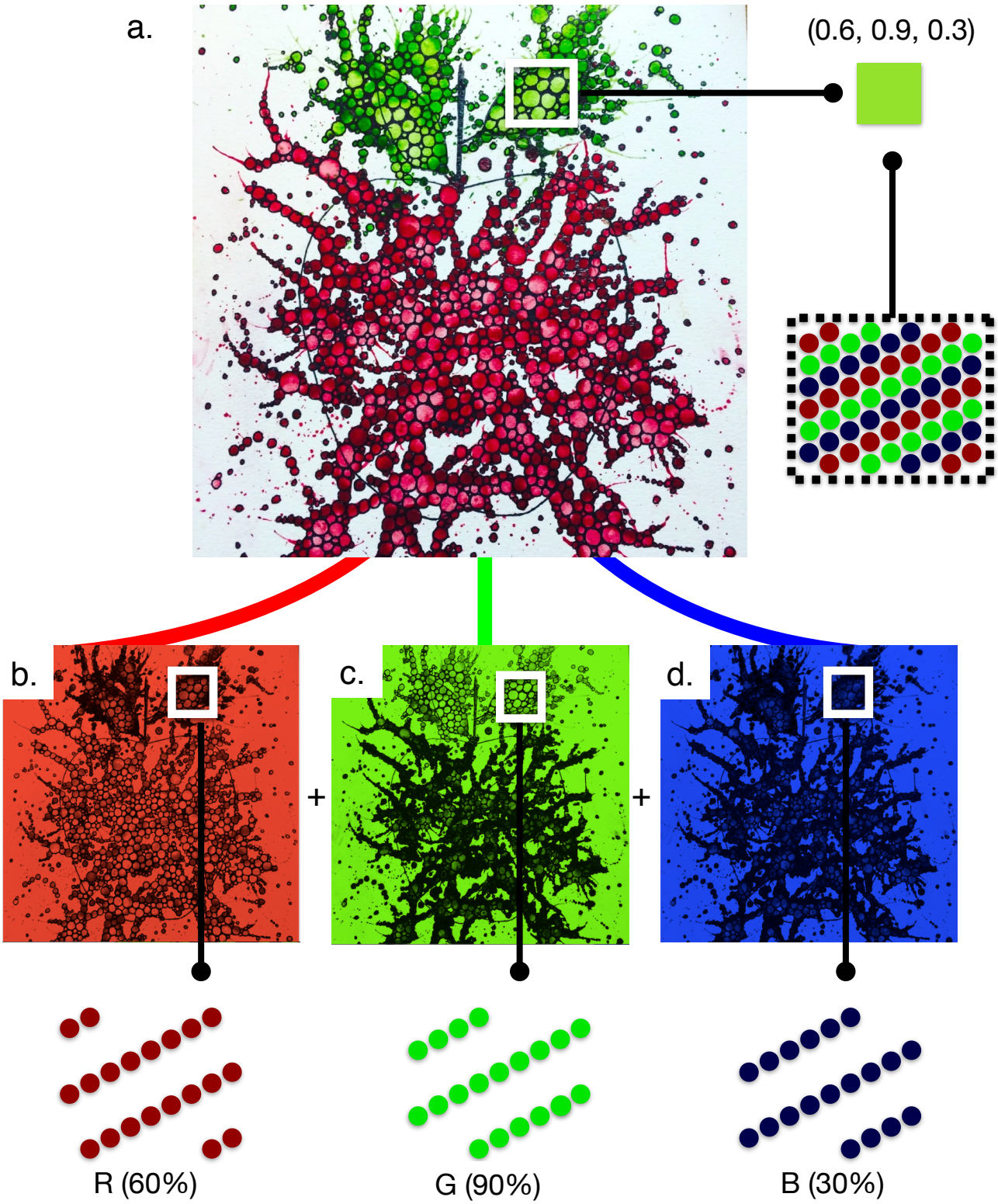

Figure 4.5. Much like an RGB electronic display, a full color image (a) with complex information can be generated using spatially separated ink droplets with variable intensity fluorescence. Any color image can be represented by extracting and reconstituting the red, green and blue channels (b - d). Painting is an original piece of artwork "Manzana", © Peter R. Christensen, 2016. For RGB extraction code see Appendix A1.

green and blue inks with photopatterned variable fluorescence intensity. Additionally, because the image is generated at the UV exposure stage, there is no need to switch out the offset pattern. If a new image is desired, only the shadow mask need be replaced, making this approach no more labor-intensive than commercially available offset printers used today.

In order for the printing method proposed in Figure 4.6 to work, inks that enable variable fluorescence intensity are required. The ideal ink formulation would be one whose fluorescence increases, or decreases in intensity after some input stimulus. Using light as a control stimulus is an ideal scenario due to the tunable and highly reproducible energy (wavelength) and resolution.

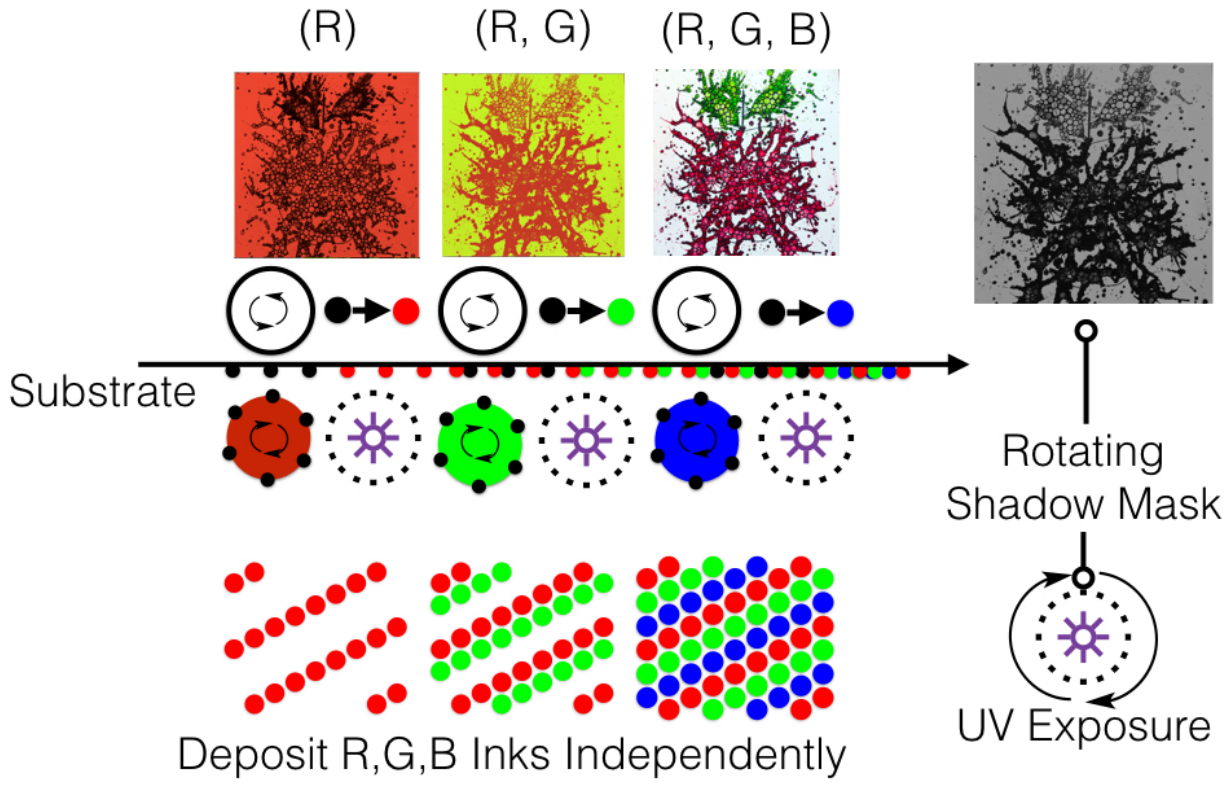

Figure 4.6. The concept behind additive RGB printing is very similar to roll-to-roll printing employed on an industrial scale for subtractive CMYK images. Three rolls, each containing a patterned surface, much like a stamp, draw the substrate through and deposit photopatternable red, green and blue ink. Each roll is calibrated such that the RGB inks are offset from one another, minimizing deleterious energy transfer. After depositing each color ink the image is exposed to UV light through a variable transmittance shadow mask (grey) that also rolls, calibrated to the position of the substrate before receiving the next color. This high throughput method should enable rapid printing of full color covert fluorescent images.

In recent years, several methods have been demonstrated whereby photoluminescent images can be patterned using light.[222,223,224,225,226] The most common approach to achieving photopatterned luminescence is through the use of photoacid de-protection. By protecting, or "caging", a fluorescent molecule with an acid-cleavable and fluorescence-quenching substituent, the fluorescence can be "turned on" by decreasing the pH of the environment. In this case, thin films containing the protected fluorescent molecule and a catalytic amount of photoacid can yield patterned luminescent images by exposure through a photomask. However, deprotection of fluorophores with photoacids typically occurs catalytically. In other words, only a catalytic amount of photoacid is required to deprotect an entire population of fluorescent molecules. Accordingly, it is difficult to selectively and reproducibly achieve control over the resulting fluorescence intensity using photoacid patterning methods. Furthermore, residual photoacid after patterning can result in image "bleaching" upon further exposure to light.

One molecule that shows photochemically controllable luminescence intensity is 9,9'-bis(anthracene)sulfoxide (**AnSO**), presented in chapter 3.[227] In the presence of UV light (300 - 425 nm) the weakly luminescent **AnSO** (Φ_{PL} < 1%) rapidly forms the highly luminescent molecule 9,9'-bianthryl (**BA**, Φ_{PL} ~ 80%)[228] in quantitative yields (Chapter 3.4.2). Of significant importance to the formation of images with controllable luminescence intensity, the conversion of **AnSO** to **BA** is not catalytic (with respect to the input of light) and, consequently, the fluorescence intensity of the mixture (**AnSO**:**BA**) can be controlled by careful exposure to light. Additionally, the formation of **BA** does not occur in the solid state, which is a highly attractive feature if lasting fluorescent images are desired.

In this chapter, the photochemical conversion of **AnSO** to **BA** is leveraged to form patterned fluorescent images with spatially controlled luminescence intensity (Figure 4.7). Making use of the optically controllable ratio of **AnSO**:**BA**, a new approach to achieve photopatterned covert barcodes is demonstrated. First**,** two-dimensional fluorescent barcodes containing an additional variable intensity verification feature "behind" the image are patterned and second, proof-of-concept three-dimensional barcodes that offer twice the data-storage capabilities (2 bits/pixel) of single color (binary, 1 bit/pixel) barcodes are generated.

4.2 Results

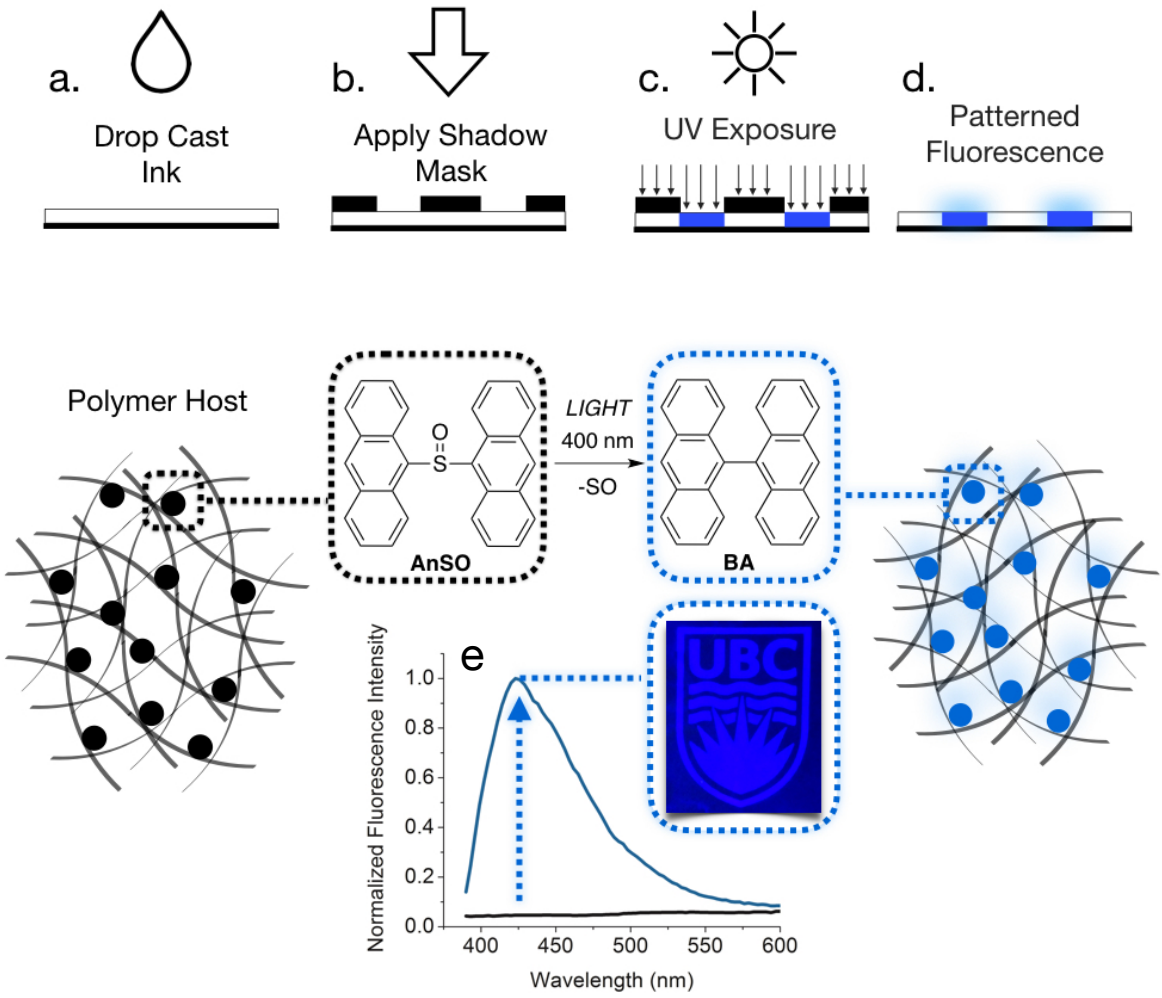

Figure 4.7. Photopatternable inks were formulated by doping **AnSO** at low concentrations into a polymer host. The **AnSO** ink was then drop cast onto a paper substrate (a) and exposed to near UV light (400 nm LED) for 2 seconds through a shadow mask (b-c). The photoproduct bianthryl (**BA**), shows a significantly higher fluorescence intensity resulting in a patterned fluorescent image (d-e). (Inset, e) Photograph of a photopatterned UBC logo on a paper substrate.

4.2.1 Ink Optimization

The photoluminescence of **BA** has been extensively studied due to its rare, symmetry breaking charge-transfer excited state.[229] While **BA** has high fluorescence quantum yields in dilute solutions, in higher concentrations **BA** tends to aggregate and crystallize, quenching photoluminescence.[230] It was found that **AnSO** should be doped at ~1 wt% in polymer host matrices in order to maintain high

fluorescence intensities (see Methods, section 4.4.1). When exposed to UV light, the polymer inks containing **AnSO** show very similar spectroscopic behavior to **AnSO** in solution (Figure 4.8; for solution spectra see section 3.4.2). Both the decrease in light absorption ~415 nm and, most importantly, the large increase in fluorescence intensity are observed.

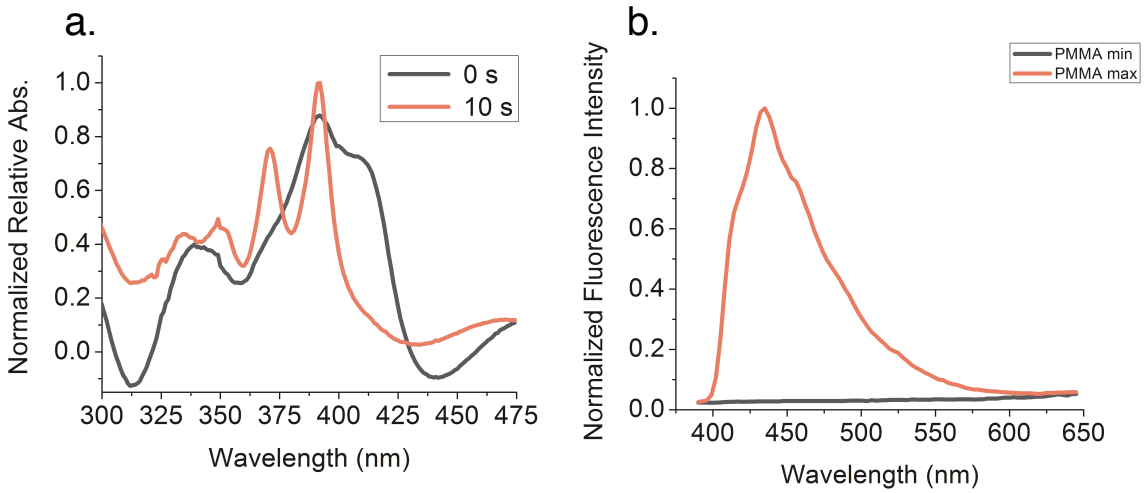

Figure 4.8. Change in UV-VIS at 0s and 10s of UV exposure for **AnSO** thin films in PMMA.

For application in image formation, the best ink formulation enables rapid photo-conversion of **AnSO** to **BA** when wet, and shows no further reactivity once dry. Since **AnSO** does not react in the solid state it is likely that the rigidity of the host material is relevant for optimizing image stability. Accordingly, **AnSO** was doped into a series of polymer host materials and the formation of **BA** was studied as a function of polymer glass transition temperature (T_g) (Figure 4.9).

The visibly transparent polymers poly(butylmethacrylate) (PBMA, T_g ~ 14 ºC), poly(methylmethacrylate) (PMMA, T_g ~ 105 ºC) and poly(*N*-vinylcarbazole) (PVK, T_g ~ 220 ºC) were chosen to yield a wide T_g range. **AnSO** was doped into each polymer host at 1 wt% and all solids were dissolved in a mixture of chloroform and chlorobenzene. Thin films of each ink were spin-coated onto glass substrates and exposed to 400 nm light at different time intervals using a custom -built LED photo-reactor (see Methods, section 4.4.6 for details). After allowing each film to dry, the fluorescence intensity was measured using a fluorimeter.

The conversion to **BA** is very fast in all polymer host materials. In PBMA, with a T_g below room temperature, the measured fluorescence intensity reaches a maximum in ~6 s. At longer irradiation times the PBMA films show a decrease in measured fluorescence intensity, likely due to either aggregation or photo-degradation. In PMMA, maximum fluorescence intensity is achieved in ~15 s and with extended irradiation begins to decrease in intensity. The PVK films, with the highest T_g, reach a maximum intensity in ~15 s and intensity decreases only slightly with further irradiation.

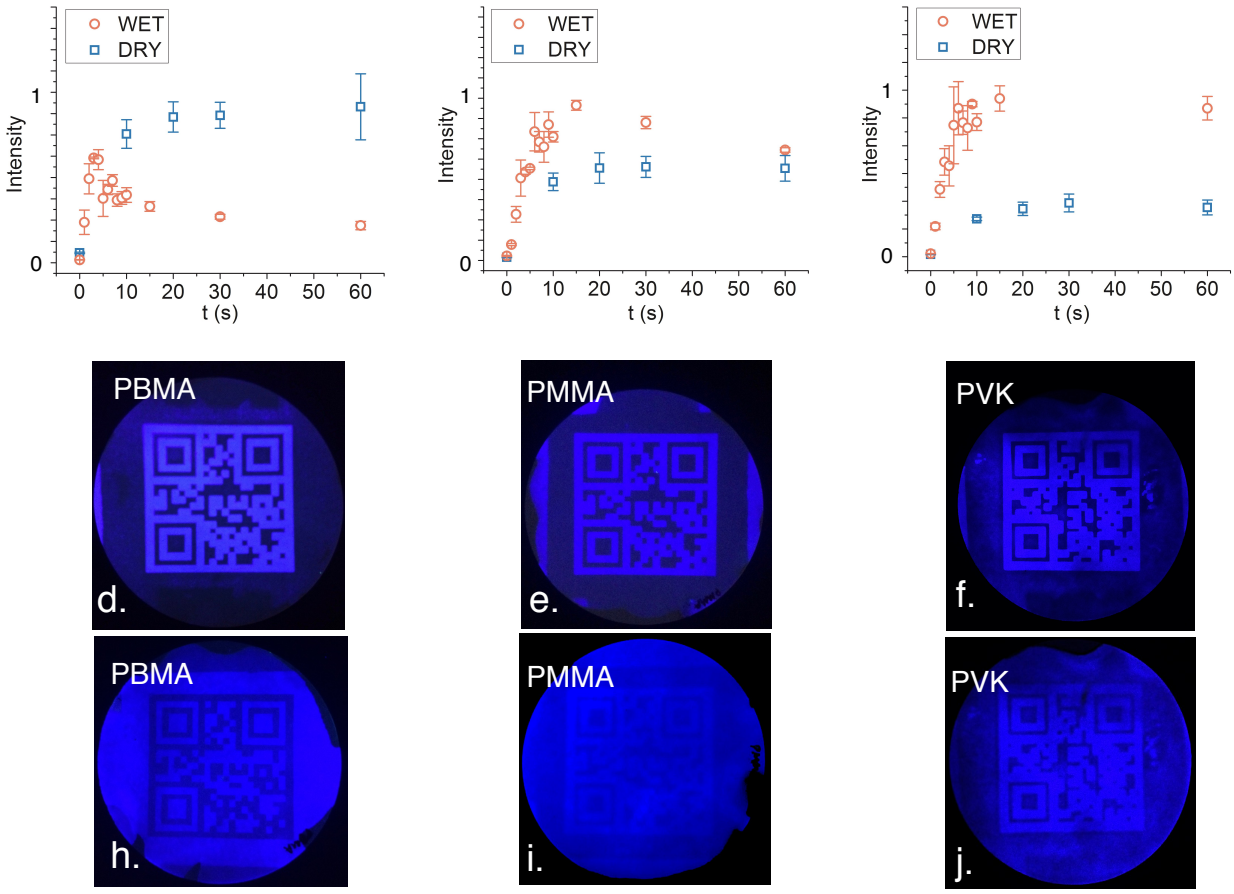

Figure 4.9. (a-c) Kinetic data for PBMA, PMMA and PVK host matrices directly after spin coating (wet, ——) and after drying (dry, ——). Pictures showing the patterned images on paper substrates in different polymer hosts as patterned (a-c), after an additional 60 s high intensity UV exposure (d-f).

To test the photo stability of unreacted ink, thin films of **AnSO**:polymer ink were spin coated onto glass substrates and dried in the dark. Following drying, the unexposed films were subjected to 400 nm light in 10 s intervals and the fluorescence intensity was measured. The dry PBMA films show an

increase in fluorescence intensity at the same rate as the wet films, reaching a maximum after ~20 s, with a slight decrease in intensity with exposure up to 60 s. Interestingly, after exposure, the dried PBMA films have a higher fluorescence intensity than that of the wet films. The dry PMMA films show an increase in intensity to ~60% of the maximum intensity obtained during wet patterning. The dry PVK films also show additional conversion but only to ~20% of the maximum obtained during wet patterning. Notably, as the T_g of the polymer host is increased, the rate of reactivity in the dried films decreases.

The photostability of patterned images also correlates well with the T_g of the polymer host (Figure 4.9d-j). After patterning (according to the scheme shown in Figure 4.7), residual solvent was removed under vacuum at room temperature and the images were subsequently exposed to further irradiation (60 s). For all polymers, the desired image is clearly visible (Figure 4.9d-f) in the region not covered by a photomask upon exposure to low intensity UV light (365 nm). For the images patterned in the PBMA host, after further exposure to intense UV light the background fluorescence increases significantly and the original image decreased in intensity yielding an "inverted" fluorescent image. For both PMMA and PVK, extended UV exposure after drying results in an increase in background fluorescence, but to a greater degree with PMMA. This experiment clearly shows that the rigidity of the host material plays a significant role in image stability. Accordingly, PVK was used as a host material throughout the remainder of the experiments presented in this chapter.

4.2.2 Variable Fluorescence Intensity

To demonstrate the variable fluorescence intensity capabilities of **AnSO**, monochrome images were created using grayscale shadow mask (Figure 4.10). In this experiment, paper substrates were coated with **AnSO**:PVK ink and exposed to 400 nm UV light for 2 seconds through the shadow mask. As shown in Figure 4.9, complex information such as a detailed portrait can be easily patterned using this approach. To measure the fluorescence intensity of the resulting patterned images, photographs were taken using a smartphone equipped with a CCD camera and the color intensity was extracted (Figure 4.10d-e).

The default settings for most camera phones is the JPEG (or JPG) image file format, which saves color information of a list (array) of RGB coordinates. A full color JPEG image will save RGB values from 0 to 255 (256 colors) for each pixel. For example, a black pixel will have an RGB value of (0,0,0)

whereas a white pixel will have a value of (255, 255, 255) yielding > 16 million possible colors. The position if each RGB value (or "tuple" in the Python programming language) in the list is representative of the position of the corresponding pixel in the image. Using this list of RGB color information, a simple piece of software was written to extract the color intensity of each pixel. Since the emission from the patterned BA is in the deep blue region of the spectrum, only the blue (B) color information from each RGB pixel was considered (see Methods, section 4.4.7, and Appendix A2 for details). Once the magnitude of the blue color for each pixel was extracted, a three dimensional plot was generated to illustrate the ability of this method to generate and extract complex covert information.

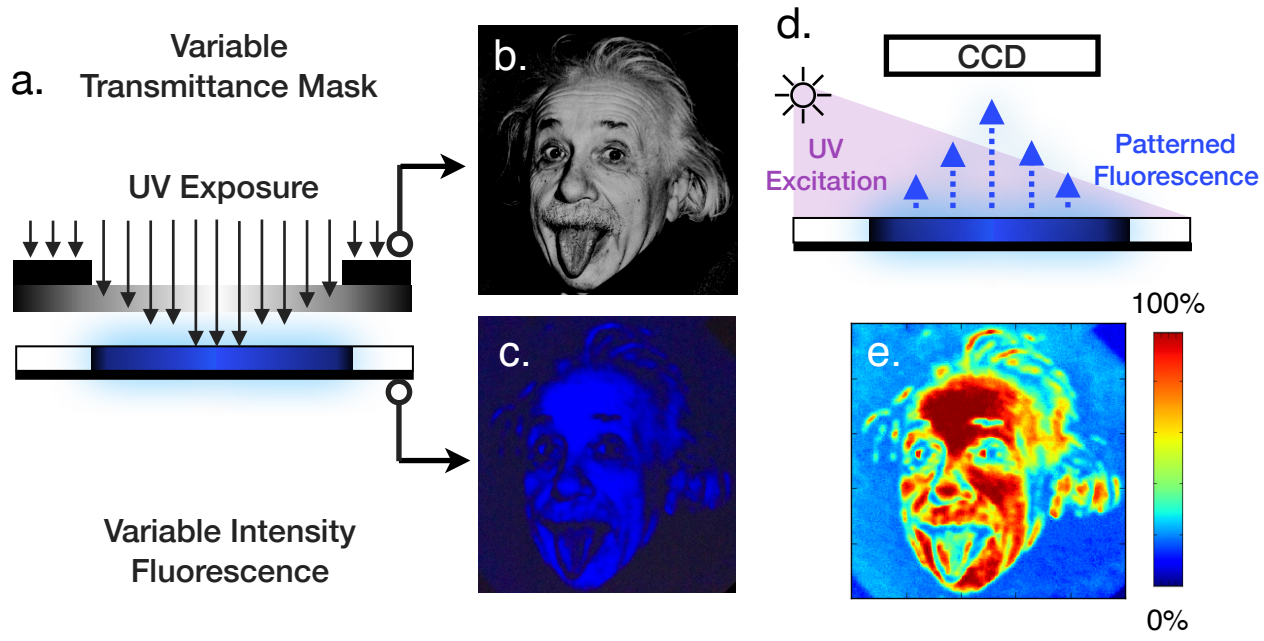

Figure 4.10. (a) Illustration showing UV exposure through a variable transmittance shadow mask (b) in order to generate a variable intensity fluorescent image on an **AnSO** ink (1% in PVK) coated paper substrate (c). The photoluminescence from the image (c) was captured using the CCD camera of an iPhone 5s (d) and the color intensity was extracted (e).

Figure 4.10c and e, respectively, show the photograph and the extracted color intensity for a portrait of Albert Einstein. This experiment demonstrates the feasibility of both creating spatially controlled luminescence intensity with complex information, and the ability to extract this information using inexpensive detection equipment.

4.2.3 Three Dimensional Covert Barcodes

To further demonstrate the multi-dimensional capabilities of the **AnSO** chromophore, three shadow masks (Figure 4.11a-c) were used, a) a two-dimensional (binary, 1/0) data matrix encoding the phrase "Hello World", b) a variable transmittance mask that has a radial gradient from 0% transmittance on the edges to 100% transmittance at the center, and c) a two stage mask containing both the two-dimensional data from (a) and the variable transmittance security feature from (b).

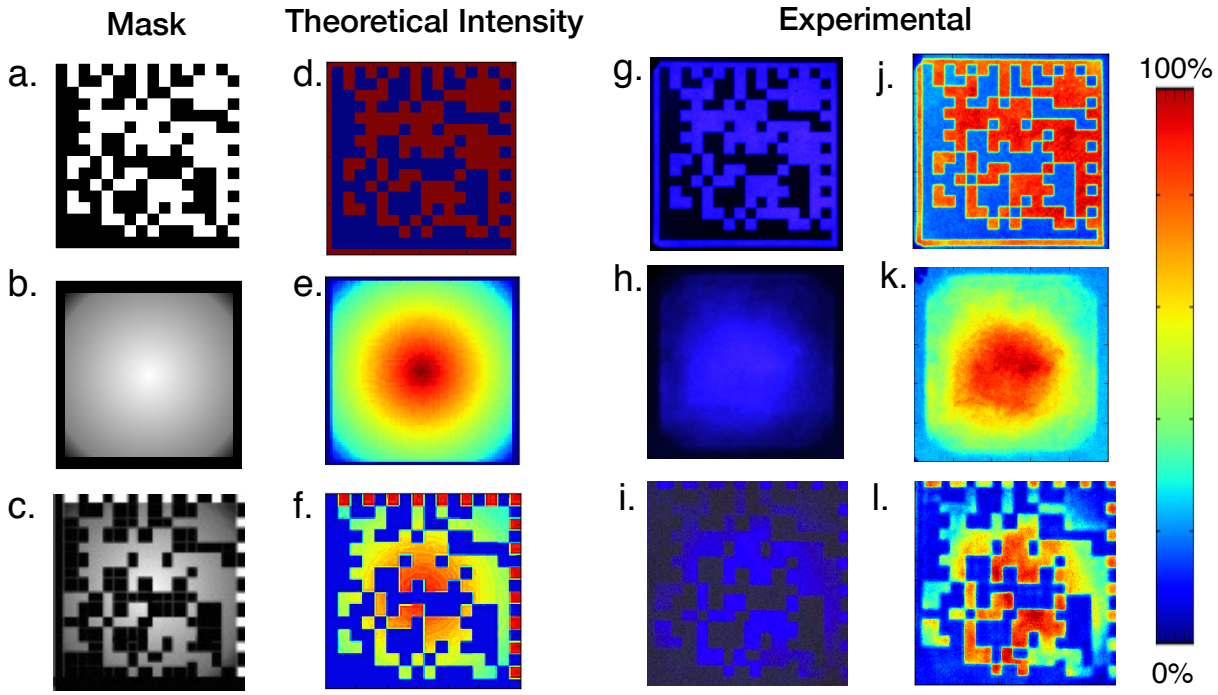

Figure 4.11. (a) Illustration showing the method used for creating variable intensity, three-dimensional fluorescent images. A two-layered mask containing both a binary data matrix (2D Data Mask) and a background image (Variable Transmittance Mask) was placed on top of a paper substrate freshly coated with **AnSO**:PVK ink. Upon exposure to 400 nm light for 2 s a 3D fluorescent image is created. (b) Images showing the three different shadow masks used and (c) the corresponding theoretical intensity from 0 - 100% of the resulting images. (d) Photographs showing fluorescent images generated using each of the masks and the computationally extracted fluorescence intensity (e).

The concept behind the two stage mask (Figure 4.11c) is that the resulting image should have two-dimensional data that is easily readable using readily available software, but "behind" this data is a variable intensity fluorescent security feature that serves as an authentication feature (Figure 4.11f). Accordingly, after UV-exposure, the resulting image should have a minimally luminescent data matrix

(corresponding to the black squares in the shadow mask) while also displaying a background fluorescent image (corresponding to the white/transparent squares) that varies from 100% in the center and radially decays to 0% at the image edges. Again paper substrates were coated with **AnSO** ink and exposed to 400 nm light for 2 seconds through each of the three shadow masks.

Indeed, Figure 4.11 (g-i) shows that this method is effective in generating multidimensional fluorescent barcodes. Under UV illumination (Figure 4.10d), both the 2D and 3D fluorescent images are readable using widely available data matrix decoding software.[231] The resulting fluorescent images (Figure 4.10g-i) were captured using the CCD camera of a cellphone and the fluorescent intensities were extracted (Figure 4.11j-i). The extracted intensities clearly show that 3D variable fluorescence can be created using this simple patterning approach. Furthermore both 2D and 3D images can be easily decoded using the CCD camera of a cellphone and a common UV or "blacklight", enabling image verification by the individual.

4.2.4 Covert Barcodes with Increased Data Density

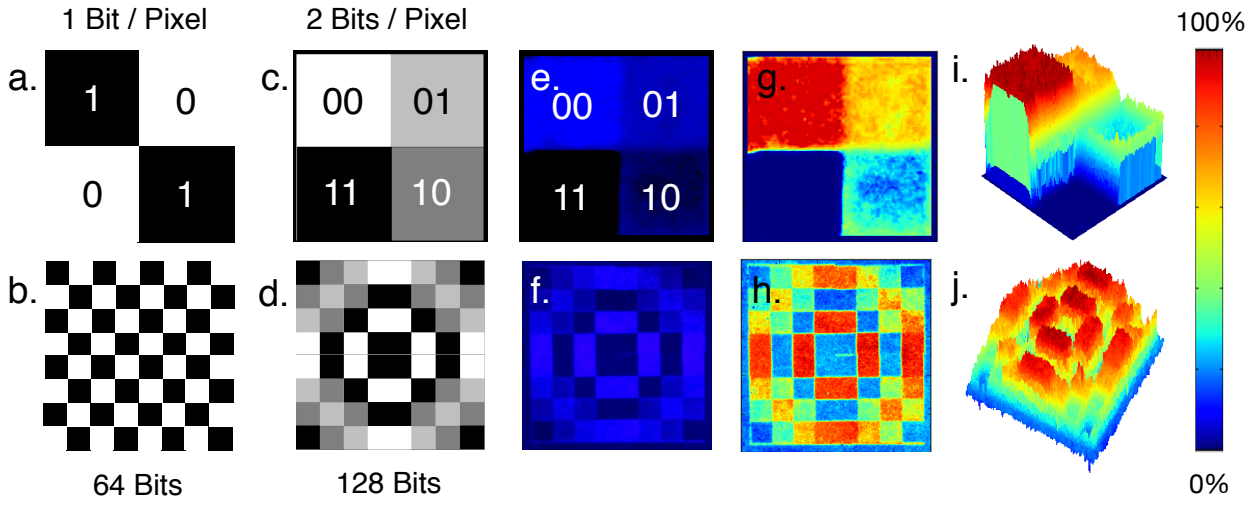

Figure 4.12. In order to increase the data density of standard binary barcodes (a-b) images containing four unique states are required (c-d). Using figures c & d as shadow masks, fluorescent images containing, respectively, 8 bits (1 byte) (e), and 128 bits (16 bytes) (e) were generated. To better visualize the two-bit/ pixel images (e-f), the fluorescence intensity was color mapped and three dimensional plots were generated (g-j).

Expanding on the three-dimensional barcode "verification" features presented in the previous section, patterned fluorescent images were created that leverage the variable intensity capabilities of the **AnSO** inks to create covert barcodes that contain twice the data storage capabilities of standard two-dimensional data matrices. With barcodes that use binary (e.g. QR and data matrices, Figure 4.2), the maximum data density that can be achieved is 1 bit/pixel from either of two states, 1 or 0. If, for example, we wanted to double the data storage of a barcode, there would need to be four accessible states (2 bits/ pixel). Figure 4.12 demonstrates this concept by showing the difference between a 1 bit and 2 bit image, where a binary 8 × 8 matrix contains 64 bits (8 bytes) of data while a quaternary matrix with the same dimensions contains 128 bits (16 bytes) of data.

In order to achieve a fluorescent image with 2 bit/pixel data density, the fluorescence intensity should be modulated in two-dimensional space with four unique and distinguishable intensities. To each of the four unique intensities (states) a 2 bit value is assigned (Figure 4.12c). To achieve a four-state fluorescent image, shadow masks were designed such that the transmission of light in various regions is set to 0% (11), 50% (01), 75% (10) or 100% (00) (Figure 4.12c and d). Paper substrates coated with **AnSO**:PVK ink were subsequently exposed to 400 nm light through shadow masks with four unique transparency “states”. As a proof of concept, two images were generated, one demonstrating the four unique fluorescence intensities (Figure 4.12e) and another demonstrating the use of these four-states in an 8 x 8, 128 bit image (Figure 4.12f). The three dimensional nature of these images is highlighted in Figure 4.12g-j. The fluorescence form all of these images can be captured using a cellphone CCD camera and a UV light source, and the information can be easily extracted using the method described in section 4.4.2 (also see Methods 4.4.7).

To further verify the ability to pattern and subsequently extract four different fluorescence intensities, the color information from each "quadrant" in Figure 4.12e (corresponding to states 00, 01,10, 11) was averaged (Figure 4.13). The extracted average values (see Appendix Figure A3 for source code) correspond quite well with the target values. The lower intensity states (0% and 50%) have the highest deviation from target intensities (measured 10% and 39% percent, respectively). The deviation from target values can be rationalized by looking at the mapped color intensities presented in Figure 4.12g. In

particular, the lower right quadrant (target 50%) shows incomplete conversion in the middle of the "pixel". Additionally, for all of the quadrants, the lines between each fluorescence "state" are not equal, yielding various sizes for each of the four patterned regions. By using a more well defined shadow mask and a more sophisticated color extraction algorithm, for instance, one that can identify the borders between states, it is likely that higher color accuracy and extraction can be achieved.

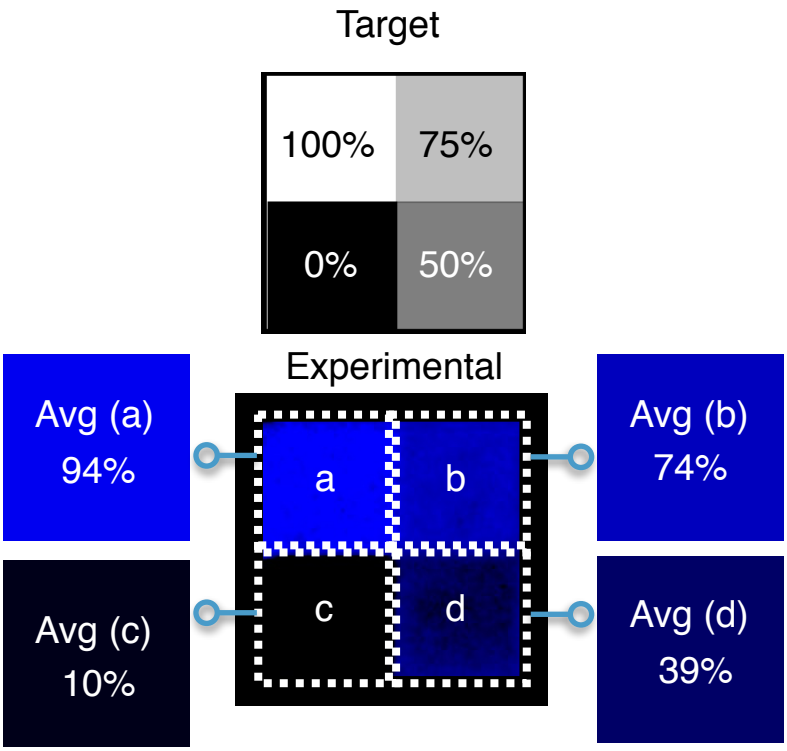

Figure 4.13. The magnitude of each "quadrant" (a-d) of the experimental four-state fluorescent images was averaged and compared to the theoretical (target) values.

4.3 Conclusions

In summary, it was demonstrated in this chapter that the rapid photochemical conversion of **AnSO** to **BA** can be used to create patterned fluorescent images. It was found that a low concentration of **AnSO** is necessary and that image stability is optimized with rigid host matrices. Additionally, it was demonstrated that through controlled light exposure, images with variable fluorescence intensity can easily be achieved. The stability of patterned images was found to be dependent on the glass transition

temperature, or rigidity of the host material. Leveraging the variable fluorescence capabilities of **AnSO**, “three-dimensional" barcodes were created as proof-of-concept covert security features. It is proposed that three-dimensional, variable fluorescence intensity can be used as an authentication feature for anti-counterfeit applications. The variable fluorescence intensity patterned images can also be used to generate covert barcodes with twice the data density of traditional binary barcodes. Generation of the patterned images and computational processing was carried out using inexpensive and ubiquitous equipment. Given its simplicity, it is possible the **AnSO** chromophore will find utility in a wide variety of applications where patterned fluorescence is of interest. Furthermore, by pushing the deep blue color of **BA** fluorescence into the green and red, for instance by substituting the 10 and 10' positions of **AnSO**, the printing method proposed in Figure 4.6 could be realized, offering a new and relatively simple approach to generating full color covert security features.

4.4 Methods

4.4.1 Synthesis and Reagents

The synthesis of **AnSO** is reported in Chapter 3 (3.9.5). Polymer host materials poly(butylmethacrylate) (PBMA, Avg. M_W ~ 320,000), poly(methylmethacrylate) (PMMA, Avg. M_W ~ 120,000), and poly(*N*-vinylcarbazole) (PVK Avg. M_W ~ 1,100,00) were purchased from Sigma Aldrich and used as received. Chloroform was purchased from Fisher Scientific and chlorobenzene was purchased form Across Organics; both solvents were used as received.

4.4.2 AnSO Loading Optimization (See Figure 4.14)

4.4.3 Polymer Host Optimization

Inks were formulated by mixing solid **AnSO** with poly(butylmethacrylate) (PBMA), poly(methylmethacrylate) (PMMA) or poly(*N*-vinylcarbazole) (PVK) and dissolving in a mixture of chloroform:chlorobenzene (2:1 for spin coating onto glass, 4:1 for paper substrates). The solvent was not optimized but was found to dissolve both **AnSO** and each polymer very well. For the purposes of

precisely measuring the **AnSO** to **BA** kinetics, a spin-coater was used in order to yield uniform and highly reproducible thin films. Standard glass microscope slides were cut into ~ 6 cm^2 pieces and were used as substrates for spin-coating. Tt was found that thin films should not be allowed to dry completely before exposure to light in order to achieve optimal conversion of **AnSO** to **BA**. Accordingly, the use of a high boiling solvent (e.g. toluene or chlorobenzene) and a short spin time (≤ 10 s) was determined to be necessary for optimal conversion of **AnSO** to **BA**. The entire surface of clean glass slides were covered with the **AnSO** ink using a pipette and first spun at 1000 rpm for 5 s, followed immediately by quickly accelerating to a spin rate of 2000 rpm for 5 s.

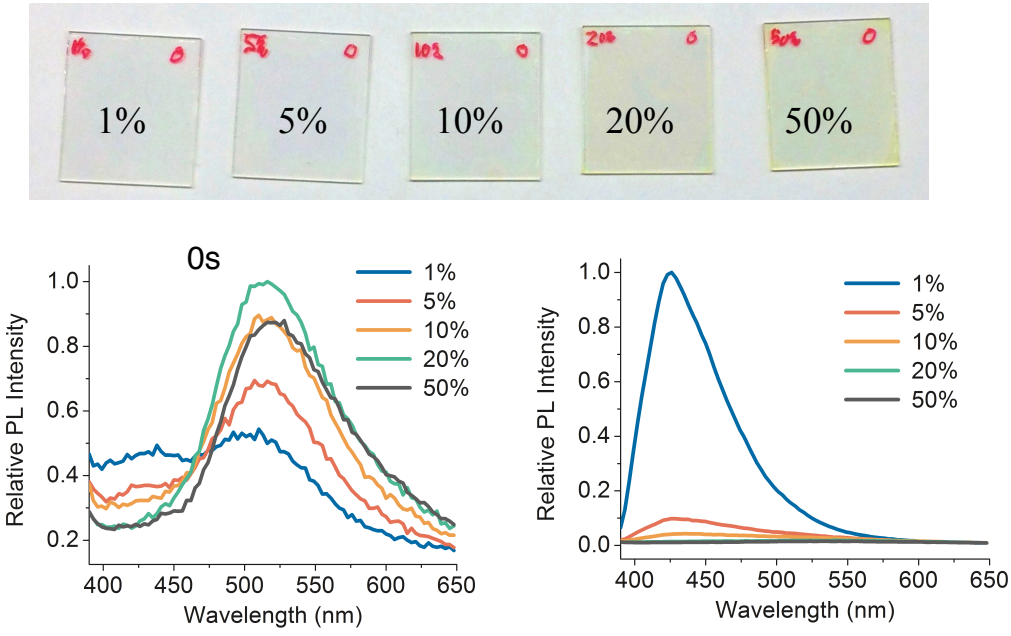

Figure 4.14. (a) Image showing the increase in yellow color of spin-coated thin films as the wt% of **AnSO** is increased from 1% to 50% in the PVK host. (b) Photoluminescence spectra of thin films without UV exposure showing an increase in PL ~515 nm with increased **AnSO** loading. (c) Photoluminescence spectra of thin films after 30 s UV exposure showing a significant decrease in PL intensity ~420 nm with increased **AnSO** loading.

4.4.4 Kinetic Measurements

Immediately after spin coating, the thin polymer films containing **AnSO** were subjected to 400 nm light using a custom built, computer controlled array of nine 3W 400 nm LEDs (full description of photoreactor can be found below, section 4.5.6). Following light exposure, the films were covered and dried under vacuum. The kinetics of **BA** formation were measured for each of the polymer hosts by

irradiating the freshly prepared thin films in one second intervals. After drying, the fluorescence intensity of each film was measured using a fluorimeter (PTI QuantaMaster 50).

4.4.5 Shadow Masks and Patterned Images

In order to generate patterned fluorescent images, the optimized ink formulation (1 wt % **AnSO** in PVK, dissolved in 4:1 chloroform/chlorobenzene) was drop-cast onto paper substrates (Whatmann Grade 1 cellulose filter paper, 55 mm) and immediately blown dry using a stream of compressed air. Prior to UV exposure, a shadow mask was placed on top of the air-dried ink-coated substrates. Shadow masks containing a variety of patterns were fabricated by printing black toner onto transparent acrylic sheets (A1 size, Figure 4.15). Following application of the shadow mask the freshly prepared thin-films were exposed to 400 nm UV light for 2 s. It was found that the conversion of **AnSO** to **BA** occurs significantly faster when it is adsorbed onto paper substrates, compared to free standing thin films.

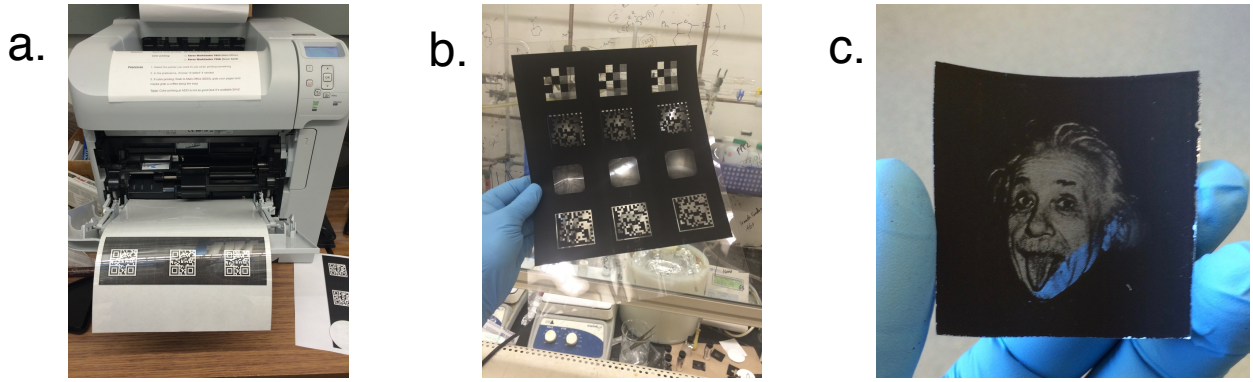

Figure 4.15. All of the shadow masks used in this study were printed on A1 size transparent acrylic sheets (a). After five passes through the printer sheets containing several sufficiently dark shadow masks were generated (b). Each mask was then cut out to yield several individual masks (c).

4.4.6 Light Source

To ensure uniform and reproducible light exposure of all samples, a custom built UV-LED photo-reactor was designed and fabricated (Figure 4.16). The main feature of this photo-reactor is the ability to easily program the intensity and duration of light exposure using an easy to use Arduino micro controller. Nine 3W UV-LEDs with a peak output wavelength of ~400 nm (Wayjun Technology Co.) were mounted

on a copper heatsink and the assembly was retrofitted with a CPU cooling fan using a 3D-printed ABS housing. The LED/fan assembly was then attached to an aluminum base, enabling the entire assembly to be moved up and down an aluminum rod. The LED assembly was held at a distance of 8 cm away from all samples, except for images where a photomask was applied (~5 cm) due to the use of clips that elevated the sample off of the platform.

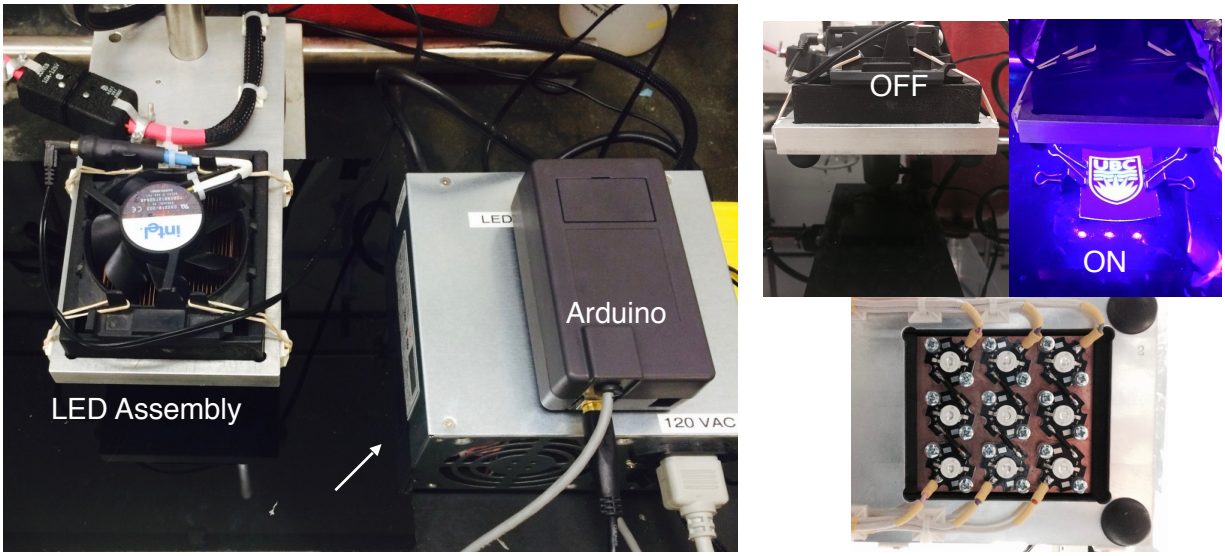

Figure 4.16. Pictures showing the photo-reactor setup used in all experiments.

4.4.7 Image Capture and Processing

The software used to analyze the images was written in the Python language using a variety of open source numerical, plotting and image manipulation packages, including Numpy, Matlotlib, Python Image Library (PIL) and OpenCV (Source code in Appendix).[232,233,234,235] First, images were captured using the CCD camera on an Apple iPhone 5s and exported in the JPG file format (this is the default setting). Images were then manually cropped to focus on the area of interest. Subsequently, the images were resized to 500 × 500 (pixels). A size of 500 × 500 was chosen because faster processing speeds were achieved while maintaining high resolution graphics. Following resizing, the intensity of the images were measured by considering the magnitude of the blue color (R,G,**B**) at each pixel. In the JPG format an

image file consists of an array (list) of RGB coordinates also known as “tuples” in the format [(red, green, blue)] where the RGB values range from 0 - 255. The list of RGB tuples was the converted to a list (newList) of single numbers that correspond to the magnitude of the blue color by taking the dot product of each RGB matrix using equation 4.1.

(4.1) $$\text{Intensity} = [R,G,B] \bullet [0,0,1]$$

This operation (equation 4.1) yields a new list (Intensity) of single floating points corresponding to the intensity of the blue color for each pixel. Following conversion to "Intensity", each value in the list was assigned a new color value (0 - 100 %, blue - red) representative of its magnitude from 0 - 255. These color mapped intensity values were then plotted three dimensionally (MatplotLib) to further illustrate the spatially variable color intensity.

REFERENCES

[1] Kardashev, N. S. *J. Sov. Astron.* **1964**, *8*, 217.

[2] U.S. Energy Information Administration. Primary Energy Production by Source, 2015 www.eia.gov/totalenergy/data/monthly/pdf/sec1_5.pdf (Accessed February 2016)

[3] Tsao, J.; Lewis, N.; Crabtree, G. *Solar FAQs* **2006**, [Online]. www.sandia.gov/~jytsao/Solar%20FAQs.pdf

[4] Calvin, M.; Benson, A. A. *Science* **1948**, *107*, 476.

[5] U.S. Energy Information Administration (EIA). How much energy is consumed in the world by each sector?, 2011 www.eia.gov/tools/faqs/faq.cfm?id=447&t=1 (Accessed February 2016)

[6] Lewis, N. S. *Science,* **2007** *315*, 798.

[7] Lewis, N. S. *Science* **2016**, *351*, 353

[8] Dunn, B.; Kamath, H.; Tarascan, J.-M. *Science* **2011**, *334*, 928.

[9] Tesla Corporation. Tesla Powerwall. www.teslamotors.com/en_CA/POWERWALL (Accessed February 2016)

[10] Weber, A. Z.; Mench, M. M.; Meyers, J. P.; Ross, P. N.; Gostick, J. T.; Liu, Q. *J. Appl. Electrochem.* **2011**, *41*, 1137.

[11] Bequerel, E. *C.R. Acad. Sci.* ,**1839**, *9*, 145.

[12] Einstein, A. *Ann. Phys.* **1905**, *17*, 132.

[13] Shockley, W. *Bell Labs Technical Journal* **1949**, *28*, 435.

[14] Ohl, R. S. "A Light Sensitive Electrical Device" U.S. Patent US2402662 A, **1946**.

[15] Van Noorden, R. *Nature* **2014**, *514*, 152.

[16] Rudan, M. *Physics of Semiconductor Devices,* Springer: New York, **2015**; p. 369.

[17] Rudan, M. *Physics of Semiconductor Devices,* Springer: New York, **2015**; p. 485.

[18] National Renewable Energy Laboratory (NREL). Research Cell Efficiency Chart. http://www.nrel.gov/ncpv/images/efficiency_chart.jpg (Accessed February 2016)

[19] Guter, W.; Schöne, J.; Philipps, S. P.; Steiner, M.; Sieger, G.; Wekkeli, A.; Weiser, E.; Oliva, E.; Bett, A. W.; Dimroth, F. *Appl. Phys. Lett.* **2009**, *94*, 223504.

[20] Fraunhofer ISE. Levelized Cost of Electricity Renewable Energy Technologies Study, 2013. https://www.ise.fraunhofer.de/en/publications/studies/cost-of-electricity (Accessed February 2016)

[21] Facchetti, A. *Chem. Mater.* **2011**, *23*, 733.

[22] Mei, J.; Diao, Y.; Appleton, A. L.; Fang, L.; Bao, Z. *J. Am. Chem. Soc.* **2013**, *135*, 6724.

[23] Yan, H.; Chen, Z.; Zheng, Y.; Newman, C.; Quinn, J. R.; Dötz, F.; Kastler, M.; Facchetti, A. *Nature* **2009**, *457*, 679.

[24] Hübler, A. C.; Kempa, H. in *Organic Photovoltaics*; Brabec, C.; Scherf, U.; Dyakonov, V., Wiley: Weinheim, Germany, **2008**; pp 513.

[25] Solopower Systems. Commercialized Flexible, Rollable Photovoltaic Device http://solopower.com/technology (Accessed February 2016)

[26] Akamatu, H.; Inokuchi, H.; Matsunaga, Y. *Nature* **1954**, *173,* 168.

[27] Shirakawa, H.; Louis, E. J.; MacDiarmid, A. G.; Chiang, C. K.; Heeger, A. J. *J. Chem. Soc., Chem. Commun.* **1977**, *16*, 578.

[28] Anthony, J. E.; Facchetti, A.; Heeny, M.; Marder, S. R. ; Zhan, X. *Adv. Mater.* **2010**, *22*, 3876.

[29] Ronali, J.; Leriche, P.; Blanchard, P. *Adv. Mater.* **2014**, *26*, 3821.

[30] Stübinger, T.; Bruiting, W. *J. Appl. Phys.* **2001**, *90*, 3632.

[31] Nenashev, A. V.; Baranovskii, S. D.; Wiemer, M.; Jansson, F.; Österbacka, R.; Dvurechenskii, A. V. Gebhard, F. *Phys. Rev. B.* **2011**, *84*, 035210.

[32] Kearns, D.; Calvin, M. *J. Chem. Phys.* **1958**, *29*, 950.

[33] Tang, C. W. *Appl. Phys. Lett.* **1986**, *48,* 183.

[34] Mikhnenko, O. V.; Blom, P. W. M.; Nguyen, T. -Q. *Energy Environ. Sci.* **2015**, *8*, 1867.

[35] Yu, G.; Gao, J.; Hummelen, J. C.; Wudl, F.; Heeger, A. J. *Science* **1995**, *270*, 1789.

[36] Guldi, D. M. *Chem. Commun.* **2000**, *5*, 321.

[37] Zhang, Q.; Kan, B.; Liu, F.; Lonog, G.; Wan, X.; Chen, X.; Zuo, Y.; Ni, W.; Zhang, H.; Li, M.; Hu, Z.; Huang, F.; Cao, Y.; Liang, Z.; Zhang, M.; Russel, T. P.; Chen, Y. *Nature Photon.* **2015**, *9*, 35.

[38] Zhao, J.; Li, Y.; Yang, G.; Jiang, K.; Lin, H.; Ade, H.; Ma, W. Yan, H. *Nature Energy* **2016**, *1*, 15027.

[39] Heliatek GmbH. Commercialized multi-junction OPV. http://www.heliatek.com/en/heliafilm/technical-data (Accessed April 2016).

[40] Lin, Y.; Zhan, X. *Mater. Horiz.* **2014**, *1*, 470.

[41] O'Regan, B.; Grätzel, M. *Nature* **1991**, *353*, 737.

[42] Nazeerudin, M. K.; Péchy, P.; Renouard, T.; Zakeeruddin, S. M.; Humphry-Baker, R.; Comte, P.; Liska, P.; Cevey, L.; Costa, E.; Shklover, V.; Spiccia, L.; Deacon, G. B.; Bignozzi, C. A.; Grätzel, M. *J. Am. Chem. Soc.* **2001**, *123*, 1613.

[43] Mathew, S.; Yella, A.; Gao, P.; Humphry-Baker, R.; Curchrod, B. F. E.; Ashari-Astani, N.; Tavernelli, I.; Rothlisberger, U.; Nazeeruddin, M. K. Grätzel, M. *Nature Chem.* **2014**, *6*, 242.

[44] Lee, M. M.; Teuscher, J.; Miyasaka, T.; Murakami, T. N.; Snaith, H. J. *Science* **2012**, *338,* 643.

[45] Green, M. A.; Ho-Baillie, A.; Snaith, H. J. *Nature Photon.* **2014**, *8*, 506.

[46] Zhou, H.; Chen, Q.; Li, G.; Luo, S.; Song, T.; Duan, H. -S.; Hong, Z.; You, J.; Liu, Y.; Yang, Y. *Science* **2014**, *345*, 542.

[47] Xing, G.; Mathews, N.; Sun, S.; Lim, S. S.; Lam, Y. M.; Grätzel, M.; Mhaisalkar, S.; Sum, T. C. *Science* **2013**, *342*, 344.

[48] Hao, F.; Stomps, C. C.; Cao, D. H.; Chang, R. P. H.; Kanatzidis, M. G. *Nature Photon.* **2014**, *8*, 489.

[49] Scholes, G. D. *J. Phys. Chem. Lett.* **2010**, *1*, 2.

[50] Roszak, A. W.; Howard, T. D.; Southall, J.; Gardiner, A. T.; Law, C. J.; Isaacs, N. W.; Cordell, R. J. *Science* **2003**, *302*, 1969.

[51] Paniz, M. Z.; Prince, S. M.; Howard, T.; Cordell, R. J.; Isaacs, N. W. *J. Mol. Biol.* **2003**, 1523.

[52] Jones, M. Bacterial Photosynthesis. http://photobiology.info/Jones.html (Accessed January, 2016)

[53] Schlau-Cohen, G. S.; Ishizaki, A.; Calhoun, T. R.; Ginsberg, N. S.; Ballotteri, M.; Bassi, R.; Fleming, G. R. *Nature Chem.* **2012**, *4*, 389.

[54] Collini, E.; Wong, C. Y.; Willk, K. E.; Curmi, P. M. G.; Brumer, P.; Scholes, G. D. *Nature* **2010**, *463*, 644.

[55] Johnson, J. C.; Nozik, A. J.; Michl, J. *J. Am. Chem. Soc.* **2010**, *132*, 16302.

[56] Zimmerman, P. M.; Zhang, Z.; Musgrave, C. B. *Nature Chem.* **2010**, *2*, 648.

[57] Zirzlmeier, J.; Lehnherr, D.; Coto, P. B.; Chernick, E. T.; Casillas, R.; Basel, B. S.; Thoss, M.; Tykwinski, R. R.; Guildi, D. M. *Proc. Natl. Acad. Sci.* **2015**, *112,* 5325.

[58] Sanders, S. N.; Kumarasamy, E.; Pun, A. B.; Trinh, M. T.; Choi, B.; Xia, J.; Taffet, E. J.; Low, J. Z. Miller, J. R.; Roy, X.; Zhu, X. -Y.; Steigerwald, M. L.; Sfeir, M. Y.; Campos, L. M. *J. Am. Chem. Soc.* **2015**, *137*, 8965.

[59] Korovina, N. V.; Das, S.; Nett, Z.; Feng, X.; Joy, J.; Haiges, R.; Krylov, A. I.; Bradforth, S. E.; Thompson, M. E. *J. Am. Chem. Soc.* **2016**, *138*, 617.

[60] Busby, E.; Xia, J.; Wu, Q.; Low, J. Z.; Song, R.; Miller, J. R.; Zhu, X. -Y.; Campos, L. M.; Sfeir, M. Y. *Nature Mater.* **2015**, *14*, 426.

[61] Johnson, J. C.; Nozik, A. J.; Michl, J. *Acc. Chem. Res.* **2013**, *46*, 1290.

[62] Cheng, Y. -C.; Fleming, G. R. *Annu. Rev. Phys. Chem.* **2009**, *60*, 241.

[63] Hsu, C.-P. You,Z.-Q.; Chen, H.-C. *J. Phys. Chem. C.* **2008**, *112*, 1204.

[64] Born, M.; Oppenheimer, R. *Ann. Phys.* **1927**, *389*, 457.

[65] Franck, J. Dymond, E. G. *Trans. Faraday Soc.* **1926**, *21*, 536.

[66] Condon, E. *Phys. Rev.* **1926**, *28*, 1182.

[67] Here *k* is the Boltzmann constant, 1.3806×10^{-23} m^2 kg s^{-2} K^{-1}, and T ~ 300 K.

[68] Turro, N. *Modern Molecular Photochemistry*, University Science Books: Sausalito, **1991**; pp 91-95.

[69] Turro, N. *Modern Molecular Photochemistry*, University Science Books: Sausalito, **1991**; pp 76-91.

[70] Scholes, G. D.; Ghiggino, K. P.; Oliver, A. M.; Paddon-Row, M. N. *J Am. Chem. Soc.* **1993**, *115,* 4345.

[71] Fassioli, F.; Dinshaw, R.; Arpin, P. C.; Scholes, G. D. *J. R. Soc. Interface* **2013**, *11*, 20130901.

[72] Kasha, M.; Rawls, H. R.; El-Bayoumi, M. A. *Pure Appl. Chem.* **1965**, *11*, 371 .

[73] Sundström, V.; Pullerits, T.; van Grondelle, R. *J. Phys. Chem.* **1999**, *103*, 2327.

[74] Scholes, G. D.; Rumbles, G. *Nature Mater.* **2006**, *5*, 683.

[75] Scholes, G. D. *Annu. Rev. Phys. Chem.* **2003**, *54*, 57.

[76] Dexter, D. L. *J. Chem. Phys.* **1953**, *21*, 836.

[77] Croce, R.; van Amerongen, H. *Nature Chem. Biol.* **2014**, *10*, 492.

[78] Ricks, A. B.; Brown, K. E.; Wenninger, M.; Karlen, S. D.; Berlin, Y. A.; Co, D. T.; Wasielewski, M. R. *J. Am. Chem. Soc*. **2012**, *134*, 4581.

[79] Mathew, S.; Yella, A.; Gao, P.; Humphry-Baker, R.; Curchod, B. F. E.; Ashari-Astani, N.; Tavernelli, I.; Rothlisberger, U.; Nazeeruddin, Md, K.; Grätzel, M. *Nature Chem*. **2014**, *6*, 242.

[80] Cheng, Y.-C.; Fleming, G. R. *Annu. Rev. Phys. Chem*. **2009**, *60*, 241.

[81] Collini, E.; Wong, C. Y.; Wilk, K. E.; Curmi, P. M. G.; Brumer, P.; Scholes, G. D. *Nature* **2010**, *463*, 644.

[82] Clayton, A. H. A.; Scholes, G. D.; Ghiggino, K. P.; Paddon-Row, M. N. *J. Phys. Chem.* **1996**, *100*, 10912.

[83] Curutchet, C.; Mennucci, B. *J. Am. Chem. Soc.* **2005**, *127*, 16733.

[84] Zhong, Y.; Trinh, M. T.; Chen, R.; Wang, W.; Khlyabich, P. P.; Kumar, B.; Xu, Q.; Nam, C.-Y.; Sfeir, M. Y.; Black, C.; Steigerwald, M. L.; Loo, Y.-L.; Xiao, S.; Ng, F.; Zhu, X. Y.; Nuckolls, C. *J. Am. Chem. Soc.* **2014**, *136*, 15215.

[85] Zhang, X.; Lu, Z.; Ye, L.; Zhan, C.; Hou, J.; Zhang, S.; Jiang, B.; Zhao, Y.; Huang, J.; Zhang, S.; Liu, Y.; Shi, Q.; Liu, Y.; Yao, *J. Adv. Mater.* **2013**, *25*, 5791.

[86] Kang, T. J.; Kahlow, M. A.; Giser, D.; Swallen, S.; Nagarajan, V.; Jarzeba, W.; Barbara, P. F. *J. Phys. Chem.* **1988**, *92*, 6800.

[87] Whited, M. T.; Patel, N. M.; Roberts, S. T.; Allen, K.; Djurovich, P. I.; Bradforth, S. E.; Thompson, M. E. Chem. Commun. **2012**, *48*, 284.

[88] Trinh, C.; Kirlikovali, K.; Das, S.; Ener, M. E.; Gray, H. B.; Djurovich, P.; Bradforth, S. E.; Thompson, M. E. *J. Phys. Chem. C.* **2014**, *118*, 21834.

[89] Bartynski, A. N.; Gruber, M.; Das, S.; Rangan, S.; Mollinger, S.; Trinh, C.; Bradforth, S. E.; Vandewal, K.; Salleo, A.; Bartynski, R. A.; Bruetting, W.; Thompson, M. E. *J. Am. Chem. Soc.* **2015**, *137*, 5397.

[90] Wohlgenannt, M.; Tandon, K.; Mazumdar, S.; Ramasesha, S.; Vardeny, Z. V. *Nature* **2001**, *409*, 494.

[91] Segal, M.; Singh, M.; Rivoire, K.; Difley, S.; Van Voorhis, T.; Baldo, M. A. *Nature Mater.* **2007**, *6*, 374.

[92] Endo, A.; Sato, K.; Yoshimura, K.; Kai, T.; Kawada, A.; Miyazaki, H.; Adachi, C. *Appl. Phys. Lett.* **2011**, *98*, 083302.

[93] Uoyama, H.; Goushi, K.; Shizu, K.; Nomura, H.; Adachi, C. *Nature* **2012**, *492*, 234.

[94] Sato, K.; Shizu, K.; Yoshimura, K.; Kawada, A.; Miyazaki, H.; Adachi, C. *Phys. Rev. Lett.* **2013**, *110*, 247401.

[95] Zhang, Q.; Li, J.; Shizu, K.; Huang, S.; Hirata, S.; Miyazaki, H.; Adachi, C. *J. Am. Chem. Soc.* **2012**, *134*, 14706.

[96] Zhang, Q.; Li, B.; Huang, S.; Nomura, H.; Tanaka, H.; Adachi, C. *Nature Photon.* **2014**, *8*, 326.

[97] Xu, B.; Holdcroft, S. *Macromolecules* **1993**, *26*, 4457.

[98] Christensen, P. R.; Nagle, J. K.; Bhatti, A.; Wolf, M. O. *J. Am. Chem. Soc.* **2013**, *135*, 8109.

[99] Lippert, E. *Z. Naturforsch. A: Phys. Sci.* **1955**, *10*, 541.

[100] Mataga, N.; Kaifu, Y.; Koizumi, M. *Bull. Chem. Soc. Jpn.* **1956**, *29*, 465.

[101] Onsager, L. *J. Am. Chem. Soc.* **1936**, *58*, 1486−1493.

[102] Grebner, D.; Helbig, M.; Rentsch, S. *J. Phys. Chem.* **1995**, *99*, 16991.

[103] Yassar, A.; Horowitz, G.; Valat, P.; Wintgens, V.; Hmyene, M.; Deloffre, F.; Srivastava, P.; Lang, P.; Garnier, F. *J. Phys. Chem.* **1995**, *99*, 9155.

[104] Kasha, M. *Radiat. Res.* **1963**, *20*, 55.

[105] Kasha, M.; Rawls, H. R.; Ashraf El-Bayoumi, M. *Pure Appl. Chem.* **1965**, *11*, 371.

[106] Spano, F. C. *Acc. Chem. Res.* **2010**, *43*, 429.

[107] Van Bolhuis, F.; Wynberg, H.; Havinga, E. E.; Meijer, E. W.; Staring, E. G. *J. Synth. Met.* **1989**, *30*, 381.

[108] Kouki, F.; Spearman, P.; Valat, P.; Horowitz, G.; Garnier, F. *J. Chem. Phys.* **2000**, *113*, 385.

[109] Beenken, W. J. D.; Pullerits, T. J. *Chem. Phys.* **2004**, *120*, 2490.

[110] Krueger, B. P.; Scholes, G. D.; Fleming, G. R. *J. Phys. Chem. B* **1998**, *102*, 5378.

[111] Scholes, G. D. *Annu. Rev. Phys. Chem.* **2003**, *54*, 57.

[112] Wong, K. F.; Bagchi, B.; Rossky, P. J. *J. Phys. Chem. A* **2004**, *108*, 5752.

[113] Harcourt, R. D.; Ghiggino, K. P.; Scholes, G. D.; Speiser, S. *J. Chem. Phys.* **1996**, *105*, 1897.

[114] Harcourt, R. D.; Scholes, G. D.; Ghiggino, K. P. *J. Chem. Phys.***1994**, *101*, 10521.

[115] Scholes, G. D.; Harcourt, R. D.; Ghiggino, K. P. *J. Chem. Phys.* **1995**, *102*, 9574.

[116] Thompson, A. L.; Gaab, K. M.; Xu, J.; Bardeen, C. J.; Martinez, T. J. *J. Phys. Chem. A* **2004**, *108*, 671.

[117] Rossi, R.; Ciofalo, M.; Carpita, A.; Ponterini, G. *J. Photochem. Photobiol. A* **1993**, *70*, 59.

[118] Becker, R. S.; Seixas de Melo, J.; Maçanita, A. L.; Elisei, F. *J. Phys. Chem.* **1996**, *100*, 18683.

[119] Bixon, M.; Jortner, J.; Verhoeven, J. W. *J. Am. Chem. Soc.* **1994**, *116*, 7349.

[120] Gould, I. R.; Young, R. H.; Mueller, L. J.; Albrecht, A. C.; Farid,S. *J. Am. Chem. Soc.* **1994**, *116*, 8188.

[121] Paa, W.; Yang, J. P.; Rentsch, S. *Appl. Phys. B: Lasers Opt.* **2000**, *71*, 443.

[122] Reyftmann, J. P.; Kagan, J.; Santus, R.; Morliere, *P. Photochem. Photobiol.* **1985**, *41*, 1.

[123] Beljonne, D.; Cornil, J.; Friend, R. H.; Janssen, R. A. J.; Brédas, J. L. *J. Am. Chem. Soc.* **1996**, *118*, 6453.

[124] Martin, R. L. *J. Chem. Phys.* **2003**, *118*, 4775.

[125] Piet, J. J.; Schuddeboom, W.; Wegewijs, B. R.; Grozema, F. C.; Warman, J. M. *J. Am. Chem. Soc.* **2001**, *123*, 5337.

[126] Giaimo, J. M.; Gusev, A. V.; Wasielewski, M. R. *J. Am. Chem. Soc.* **2002**, *124*, 8530.

[127] Rentsch, S.; Yang, J. P.; Paa, W.; Birckner, E.; Schiedt, J.; Weinkauf, R. *Phys. Chem. Chem. Phys.* **1999**, *1*, 1707.

[128] Fabiano, E.; Della Sala, F.; Cingolani, R.; Weimer, M.; Goerling, A. *J. Phys. Chem. A* **2005**, *109*, 3078.

[129] Weinhold, F. L., C.R *Valency and Bonding: A Natural Bond Orbital Donor-Acceptor Perspective*; Cambridge University Press: Cambridge, UK, **2005**.

[130] Chesnut, D. B.; Quin, L. D. *J. Comput. Chem.* **2004**, *25*, 734.

[131] Zhang, Q.; Silbey, R. *J. Chem. Phys.* **1990**, *92*, 4899.

[132] Terenziani, F.; Painelli, A.; Katan, C.; Charlot, M.; Blanchard-Desce, M. *J. Am. Chem. Soc.* **2006**, *128*, 15742.

[133] Lewis, F. D.; Daublain, P.; Zhang, L.; Cohen, B.; Vura-Weis, J.; Wasielewski, M. R.; Shafirovich, V.; Wang, Q.; Raytchev, M.; Fiebig, T. *J. Phys. Chem. B* **2008**, *112*, 3838.

[134] Schutz, M.; Schmidt, R. *J. Phys. Chem.* **1996**, *100*, 2012.

[135] Grabner, G.; Rechthaler, K.; Kohler, G. *J. Phys. Chem. A* **1998**, 102, 689.

[136] Aldern, R. G.; Parson, W. W.; Chu, Z. T.; Warshel, A. *J. Am. Chem. Soc.* **1995**, *117*, 12284.

[137] Lunkenheimer, B.; Kohn, A. *J. Chem. Theory Comput.* **2013**, *9*, 977.

[138] Lu, R.; Lin, *J. Comput. Theor. Chem.* **2014**, *1037*, 10.

[139] Wei, S.; Xia, J.; Dell, E. J.; Jiang, Y.; Song, R.; Lee, H.; Rodenbough, P.; Briseno, A. L.; Campos, L. M. *Angew. Chem. Int. Ed.* **2014**, *53*, 1832.

[140] Spano, F. C.; Mukamel, S. *J. Chem. Phys.* **1989**, *91*, 683.

[141] Greyson, E. C.; Vura-Weis, J.; Michl, J.; Ratner, M. A. *J. Phys. Chem. B* **2010**, *114*, 14168.

[142] Smith, M. B.; Michl, J. *Annu. Rev. Phys. Chem.* **2013**, *64*, 361.

[143] Berkelbach, T. C.; Hybertsen, M. S.; Reichman, D. R. *J. Chem. Phys.* **2013**, *138*, 114102.

[144] Vallett, P. J.; Snyder, J. L.; Damrauer, N. H. *J. Phys. Chem. A* **2013**, *117*, 10824.

[145] Surface Xplorer; Ultrafast Systems LLC: Sarasota, FL, 2010.

[146] Parr, R. G.; Yang, W. *Density Functional Theory of Atoms and Molecules*; Oxford University Press, New York, **1994**.

[147] Ziegler, T. *Chem. Rev.* **1991**, *91*, 651.

[148] Yanai, T.; Tew, D. P.; Handy, N. C. *Chem. Phys. Lett.* **2004**, *393*, 51.

[149] Mark, E. C. *In Recent Advances in Density Functional Methods*; World Scientific: Singapore, **1995**; Vol. 1, p 155.

[150] Runge, E.; Gross, E. K. U. *Phys. Rev. Lett.* **1984**, *52*, 997.

[151] Fetter, A. L.; Walecka, J. D. *Quantum Theory of Many Particle Systems; Dover Publications*: Mineola, NY, 2003.

[152] Hirata, S.; Head-Gordon, M. *Chem. Phys. Lett.* **1999**, *314*, 291.

[153] Fabian, *J. Theor. Chem. Acc.* **2001**, *106*, 199.

[154] Preat, J. *J. Phys. Chem. C* **2010**, *114*, 16716.

[155] Camino, B.; De La Pierre, M.; Ferrari, A. M. *J. Mol. Struct.* **2013**, *1046*, 116.

[156] Jungsuttiwong, S.; Tarsang, R.; Sudyoadsuk, T.; Promarak, V.; Khongpracha, P.; Namuangruk, S. *Org. Electron.* **2013**, *14*, 711.

[157] Truong, T. N.; Stefanovich, E. V. *Chem. Phys. Lett.* **1995**, *240*, 253.

[158] Subotnik, J. E.; Cave, R. J.; Steele, R. P.; Shenvi, N. *J. Chem. Phys.* **2009**, *130*, 234102.

[159] Shao, Y. et. al. *Mol. Phys*. **2015**, *113*, 184.

[160] Glendening, E. D. B, J. K.; Reed, A. E.; Carpenter, J. E.;Bohmann, J. A.;Morales, C. M.;Weinhold, F. NBO 5.0 package; Theoretical Chemistry Institute, University of Wisconsin: Madison, WI, 2001.

[161] Boens, N.; Qin, W.; Basarić, N.; Hofkens, J.; Ameloot, M.; Pouget, J.; Lefvre, J.-P.; Valeur, B.; Gratton, E.; vande Ven, M; Silva, N.D., Jr.; Engelborghs, Y.; Willaert, K.; Sillen, A.; Rumbles, G.; Phillips, D.; Visser, A.J.W.G.; Malak, H.; Gryczynski, I.; Szabo, A.G.; Krajcarski, D.T.; Tamai, N.; Miura, A. *Anal. Chem.* **2007**, *79*, 2137.

[162] Van Bolhuis, F.; Wynberg, H.; Havinga, E. E.; Meijer, E. W.; Staring, E. G. *J. Synth. Met.***1989**, *30*, 381.

[163] Park, N.; Park, K.; Jang, M.; Lee, S. *J. Org. Chem.* **2011**, *76*, 4371.

[164] Chen, C.; Weng, Z.; Hartwig, J. F. *Organometallics* **2012**, *31*, 8031.

[165] Uyeda, C.; Tan, Y.; Fu, G. C.; Peters, J. C. *J. Am. Chem. Soc.* **2013**, *135*, 9548.

[166] Hartwig, J. F. *Acc. Chem. Res.* **2008**, *41*, 1534.

[167] CCDC reference numbers 950417, 950418, 950419, 950420 contain the supplementary crystallographic data for this chapter. These data can be obtained free of charge from The Cambridge Crystallographic Data Centre via www.ccdc.cam.ac.uk/data_request/cif.

[168] Kyzioł, J. B.; Zaleski, J.; *Acta. Cryst.* **2007**, *63*, 1235.

[169] Deng, W.-Q.; Goddard, W. A. *J. Phys. Chem. B* **2004**, *108*, 8614.

[170] Tannaci, J. F.; Noji, M.; McBee, J. L.; Tilley, T. D. *J. Org. Chem.* **2008**, *73*, 7895.

[171] Fritzsche, J. *Pract. Chem.* **1867**, *101*, 7363.

[172] Bouas-Laurent, H.; Castellan, A.; Desvergne, J.-P.; Lapouyade, R. *Chem. Soc. Rev.* **2001**, *30*, 248.

[173] Bouas- Laurent, H.; Castellan, A.; Desvergne, J. P.; Lapouyade, R. *Chem. Soc. Rev.* **2000**, *29*, 43.

[174] Becker, H. D. *Chem. Rev.* **1993**, *93*, 145.

[175] Mock, W. L. *J. Am. Chem. Soc.* **1975**, *97*, 3673.

[176] Surez, D.; Sordo, J. A.; Sordo, T. L.; *J. Phys. Chem.* **1996**, *100*, 13462.

[177] Harel, T.; Amir, E.; Rozen, S. *Org. Lett.* **2006**, *8*, 1213.

[178] Mataga, N.; Yao, H.; Okada, T.; Rettig, W. *J. Phys. Chem.* **1989**, *93*, 3383.

[179] Simon, J. D.; Su, S. *J. Chem. Phys.* **1987**, *87*, 7016.

[180] Rettig, W.; Paeplow, B.; Herbst, H.; Müllen, K.; Desvergne, J. P.; Bouas-Laurent, H. New *J. Chem.* **1999**, *23*, 453.

[181] Dramrauer, N. H.; Cerullo, G.; Yeh, A.; Boussie, T. R.; Shank, C. V.; McCusker, J. K. *Science* **1997**, *275*, 54.

[182] Islangulov, R. R.; Castellano, F. N. *Angew. Chem.* **2006**, *118*, 6103.

[183] Grainger, R. S.; Patel, B.; Kariuki, B. M.; Male, L.; Spencer, N. *J. Am. Chem. Soc.* **2011**, *133*, 5843.

[184] Wang, Z. "Norrish Type II Reaction", Wiley, **2010**

[185] Lee, W.; Jenks, W. *J. Org. Chem.* **2001**, *66*, 474.

[186] SAINT. Version 8.27B. Bruker AXS Inc., Madison, Wisconsin, USA, **1997-2013**.

[187] TWINABS.V.2012/1 Bruker AXS Inc., Madison, Wisconsin, **2012**.

[188] SIR97 - Altomare A.; Burla M.C.; Camalli M.; Cascarano G.L.; Giacovazzo C.; Guagliardi A.; Moliterni A.G.G.,;Polidori G.; Spagna R. *J. Appl. Cryst.* **1999**, *32*, 115.

[189] Least squares function minimized: $S_w(F_o^2-F_c^2)^2$.

[190] Standard deviation of an observation of unit weight: $[S_w(F_o^2-F_c^2)^2/(N_o-N_v)]^{1/2}$, where N_o = number of observations, N_v = number of variables.

[191] Cromer, D. T.; Waber, J. T. "International Tables for X-ray Crystallography", Vol. IV, The Kynoch Press, Birmingham, England, Table 2.2 A, **1974**.

[192] Ibers, J. A.; Hamilton, W. C. *Acta Crystallogr.* **1964**, *17*, 781.

[193] Creagh, D. C.; McAuley, W.J. "International Tables for Crystallography", Vol C, (A.J.C. Wilson, ed.), Kluwer Academic Publishers, Boston, Table 4.2.6.8, pages 219-222, **1992**.

[194] Creagh, D. C.; Hubbell, J.H. "International Tables for Crystallography", Vol C, (A.J.C. Wilson, ed.), Kluwer Academic Publishers, Boston, Table 4.2.4.3, pages 200-206, **1992**.

[195] Sheldrick, G. M. *Acta Cryst.* **2008**, *A64*, 112.

[196] OLEX2 – A complete structure solution, refinement and analysis program *J. Appl. Cryst.* **2009***, 42*, 339.

[197] World Health Organization (WHO), Anti-Counterfeit Technologies for the International Medical Products Anti-Counterfeiting Taskforce. http://www.fip.org/impactglobalforum/pdf/backgroundinfo/IMPACT%20-%20AC%20Technologies%20v2.pdf (Accessed January, 2016)

[198] Mackey, T, K.; Liang, B. A.; York, P.; Kubic. T. *Am. J. Trop. Med. Hyg.* **2015**, *92*, 59.

[199] Bansal, D.; Malla, S.; Gudala, K.; Tiwari, P. *Sci. Pharm.* **2013**, *81*, 1.

[200] ITU mobile subscription data 2015 https://www.itu.int/en/ITU-D/Statistics/Pages/stat/default.aspx (Accessed January 2016)

[201] Martinez, A. W.; Phillips, S. T.; Carrilho, E.; Thomas III, S. W.; Sindi, H.; Whitesides, G. M. *Anal. Chem.* **2008**, *80*, 3699.

[202] Martinez, A. W.; Phillips, S. T.; Whitesides, G. M.; Carrilho, E. *Anal. Chem.* **2010**, *82*, 3.

[203] Hou, X.; Ke, C.; Burns, C. J.; McGonigal, P. R.; Pettman, R. B.; Stoddart, J. F. *Nature Comm.* **2015**, 6:6884.

[204] De Cremer, G.; Self, B. F.; Hotta, J.; Roeffaera, M. B. J.; Bartholomeeusen, E.; Coutiño-Gonzalez, E.; Valtchev, V.; De Vos, D. E.; Vosch, T.; Hofkens, J. *Adv. Mater.* **2010**, 22, 957.

[205] Han, S.; Bae, H. J.; Kim, J.; Shin, S.; Choi, S. -E.; Lee, S. H.; Kwon, S.; Park, W. *Adv. Mater.* **2012**, *24*, 5924.

[206] Yoon, B.; Lee, J.; Park, I.; Jeon, S.; Lee, J.; Kim, J. -M.; *J. Mat. Chem C* **2013**, *1*, 2388.

[207] Shah, R. Y.; Prajapati, P. N.; Agrawal, Y. K. *J. Adv. Pharm. Technol. Res.* **2010**, *1*, 368.

[208] Rogojevic, S.; Parthasarathy, G. U.S. Patent 8,022,623, **2011**.

[209] Hayashi, K.; Nakanotani, H.; Inoue, M.; Yoshida, K.; Mikhnenko, O.; Nguyen, T. -Q.; Adachi. C. *Appl. Phys. Lett.* **2015**, *106*, 093301.

[210] McDowell, J. J.; Maier-Flaig, F.; Wolf, T. J. A.; Unterreiner, A. -N.; Lemmer, U.; Ozin, G. A. *ACS Appl. Mater. Interfaces.* **2014**, *6*, 83.

[211] Nie, Z.; Kumacheva, E. *Nature Mater.* **2008**, *7*, 277.

[212] DeForest, C. A.; Tirrell, D. A. *Nature Mater.* **2015**, *14*, 523.

[213] Grenier, V.; Walker, A. S.; Miller, E. W. *J. Am. Chem. Soc.* **2015**, *137*, 10894.

[214] Strale, P. -O.; Azioune, A.; Bugnicourt, G.; Lecomte, Y.; Chahid, M.; Studer, V. *Adv. Mater.* **2015**, DOI: 10.1002/adma.201504154

[215] Chan, V.; Zorlutuna, P.; Jeong, J. H.; Kong, H.; Bashir, R. *Lab Chip.* **2010**, *10*, 2062.

[216] Hess, S. T.; Girirajan, T. P. K.; Mason, M. D. *Biophys. J.* **2006**, *91*, 4258.

[217] Peyser, L. A.; Vinson, A. E.; Bartko, A. P.; Dickson, R. M. *Science* **2001**, *291*, 103.

[218] Crumpston, B. H.; Anathavel, S. P.; Barlow, S.; Dyer, D. L.; Ehrlich, J. E.; Erskine, L. L.; Heikal, A. A.; Kuebler, S. M.; Lee, I.-Y. S.; McCord-Maughton, D.; Qin, J.; Röckel, H.; Rumi, M.; Wu, X.-L.; Mader, S. R.; Perry, J. W. *Nature* **1999**, *398*, 51.

[219] Corredor, C. C.; Huang, Z.-L.; Belfield, K. D. *Adv. Mater.* **2006**, *18*, 2910.

[220] Belfield, K. D.; Schafer, K. J *Chem. Mater.* **2002**, *14*, 3656.

[221] Belfield, K. D. U.S. Patent 7,598,018, **2009**.

[222] Kim, J. -M. *Macromol. Rapid Commun.* **2007**, *28*, 1191.

[223] Yoon, B.; Oh, E. H.; Lee, C. W.; Kim, J. -M. *Bull. Korean Chem. Soc.* **2013**, *34*, 1282.

[224] McDowell, J. J.; Maier-Flaig, F.; Wolf, T. J. A.; Unterreiner, A. -N.; Lemmer, U.; Ozin, G. A. *ACS Appl. Mater. Interfaces.* **2014**, *6*, 83.

[225] Kim, J. -M.; Lee, Y. B.; Yang, D. H.; Lee, J. -S.; Lee, G. S.; Ahn, D. J. *J. Am. Chem. Soc.* **2005**, *127*, 17580.

[226] Shi, W.; Lin, Y.; He, S.; Zhao, Y.; Li, C.; Wei, M.; Evans, D. G.; Duan, X. *J. Mat. Chem.* **2011**, *21*, 11116.

[227] Christensen, P. R.; Patrick, B. O.; Caron, É.; Wolf, M. O. *Angew. Chem.* **2013**, *125*, 13184.

[228] Schmaltz, M.; Schmidt, R. *J. Phys. Chem.* **1996**, *100*, 2012.

[229] Grabner, G.; Rechthaler, K.; Köhler, G. *J. Phys. Chem. C.* **1998**, *102*, 689.

[230] Yu, Y.; Wu, Z. ; Li, Z.; Jiao, B.; Li, L.; Ma, L.; Wang, D.; Zhou, G.; Hou, X. *J. Mat. Chem. C,* **2013**, *1*, 8117.

[231] 3GVision i-nigma barcode reader for Apple iPhone, www.i-nigma.com (Accessed January, 2016)

[232] NumPy Package for Python http://www.numpy.org/ (Accessed January, 2016)

[233] MatplotLib 2.0 Plotting Package for Python http://matplotlib.org/ (Accessed January, 2016)

[234] Python Imaging Library (PIL) https://pypi.python.org/pypi/PIL (Accessed January, 2016)

[235] Open Source Computer Vision (OpenCV) Image Processing Package for Python http://opencv.org/ (Accessed January, 2016)

APPENDIX

A.1 Python Source Code

Listing A1.1 Python script used to extract the red (R) green (G) and blue (B) pixel information from JPG images.

```
import PIL
from PIL import Image

import numpy as np
from mpl_toolkits.mplot3d import Axes3D
from matplotlib import pylab as pl


# Load Full Color (R,G,B) JPG

red = Image.open('JPG File Directory')
green = Image.open('JPG File Directory')
blue = Image.open('JPG File Directory')


# Creates New Image Containing Only Red Pixel Data (R,0,0)

for i in range(red.size[0]):
    for j in range(red.size[1]):
        r = red.getpixel((i,j))
        red.putpixel((i,j),(r[0],0,0))


# Creates New Image Containing Only Green Pixel Data (0,G,0)

for h in range(green.size[0]):
    for k in range(green.size[1]):
        g = green.getpixel((h,k))
        green.putpixel((h,k),(r[0],g[1],0))



# Creates New Image Containing Only Blue Pixel Data (0,0,B)

for l in range(blue.size[0]):
    for m in range(blue.size[1]):
        b = blue.getpixel((l,m))
        blue.putpixel((l,m),(0,0,b[2]))


# Show Red Image

red.show()


# Show Green Image

green.show()


# Show Blue Image

blue.show()
```

Listing A1.2 Python script used to plot the color intensity of the fluorescent images (Chapter 4) in 2D and 3D.

```
from mpl_toolkits.mplot3d import Axes3D
from matplotlib import pylab as pl
import matplotlib.image as mpimg

from PIL import Image
import numpy as np
import pylab
import cv2



#Open Image
img = Image.open('File Directory.jpg')


# Resize
small = img.resize((500,500), Image.ANTIALIAS)
ext = ".jpg" # new file type
small.save("ANTIALIAS" + ext)


# Blue PIX Function
def rgb2gray(rgb):
    return np.dot(rgb[...,:3], [0, 0, 1])



#Convert Resized JPG, saves as an array
gray = rgb2gray(np.asarray(small))


#Plot Color Mapped Intensity in 2D and 3D

data = gray[::1,::1]
fig = pl.figure(facecolor='w')
ax1 = fig.add_subplot(1,2,1)
ax2 = fig.add_subplot(1,2,2,projection='3d')
im = ax1.imshow(data,interpolation='nearest',cmap=pl.cm.jet)


ax1.set_axis_off()
ax2.set_autoscale_on(False)


x,y = np.mgrid[:data.shape[0],:data.shape[1]]
ax2.plot_surface(x,y,data,cmap=pl.cm.jet,rstride=1,cstride=1,linewidth=0.,antialiased=False)

ax2.set_zlim3d(0,100)
ax2.set_axis_off()
pl.show()
```

Listing A1.3 Python script used to measure the average value of the blue color intensity of an image.

```
import PIL
from PIL import Image

# Load Image Files, Manually Cropped "Quadrants"

A = Image.open('/Users/pchristensen/Desktop/cropped Mosaic/Blue0.jpg')
B = Image.open('/Users/pchristensen/Desktop/cropped Mosaic/Blue50.jpg')
C = Image.open('/Users/pchristensen/Desktop/cropped Mosaic/Blue75.jpg')
D = Image.open('/Users/pchristensen/Desktop/cropped Mosaic/Blue100.jpg')

# Create 4 New Lists, One for Each Image

alpha = []
beta = []
gamma = []
delta = []

# Populate Lists with RGB data from Images A, B, C and D.

for i in range(A.size[0]):
    for j in range(A.size[1]):
        alpha.append(A.getpixel((i,j)))

for i in range(B.size[0]):
    for j in range(B.size[1]):
        beta.append(B.getpixel((i,j)))

for i in range(C.size[0]):
    for j in range(C.size[1]):
        gamma.append(C.getpixel((i,j)))

for i in range(D.size[0]):
    for j in range(D.size[1]):
        delta.append(D.getpixel((i,j)))

# Averaging Function

def tuple_avg(tuples, index):
    items = [t[index] for t in tuples]
    return float(sum(items))/len(items)

# Create New Lists that only contain the Blue data (0,0,B)
# Each Pixel (data ranging from 0 - 255) is Converted into a Value Ranging from 0 - 1

Anewpix  = [((0,0,round(n[2]/255.0,2))) for n in alpha]
Bnewpix  = [((0,0,round(n[2]/255.0,2))) for n in beta]
Cnewpix  = [((0,0,round(n[2]/255.0,2))) for n in gamma]
Dnewpix  = [((0,0,round(n[2]/255.0,2))) for n in delta]


# Averages the data (0 - 1) from each of the new lists and prints a value.

tuple_avg(Anewpix, 2)
tuple_avg(Bnewpix, 2)
tuple_avg(Cnewpix, 2)
tuple_avg(Dnewpix, 2)
```